Wetting, evaporation and deposition processes in interaction of complex liquid formulations with porous substrates

Abhijeet Kumar

11.11.2019



TECHNISCHE UNIVERSITÄT DARMSTADT

TTD
Technische Thermodynamik

Wetting, evaporation and deposition processes in interaction of complex liquid formulations with porous substrates

Vom Fachbereich Maschinenbau

an der Technischen Universitat Darmstadt

zur Erlangung des akademischen Grades eines

Doktor-Ingenieurs (Dr.-Ing.)

genehmigte

Dissertation

vorgelegt von

M.Sc. Abhijeet Kumar

aus Dumka, Indien

Berichterstatter (1. Gutachten): Apl. Prof. Dr. Tatiana Gambaryan-Roisman
Mitberichterstatter (2. Gutachten): Prof. Dr. -Ing. Peter Stephan
Mitberichterstatter (2. Gutachten): Prof. Dr. Regina von Klitzing

Technische Thermodynamik
Tag der Einreichung: 11.11.2019
Tag der mündlichen Prüfung: 21.01.2020

Darmstadt, 2020

Abhijeet Kumar : Wetting, evaporation and deposition processes in interaction of complex liquid formulations with porous substrates
Dissertationsort : Darmstadt, Technische Universität Darmstadt
Veröffentlichungsjahr der Dissertation auf TUprints : 2020
URN der Dissertation : urn:nbn:de:tuda-tuprints-142114
Tag der mündlichen Prüfung : 21.01.2020

Veröffentlicht unter CC BY-SA 4.0 International
https://creativecommons.org/licenses/

Erklärung

Hiermit erkläre ich, dass ich die vorliegende Arbeit, abgesehen von den in ihr ausdrücklich genannten Hilfen, selbständig verfasst habe.

_____

Darmstadt, 11.11.2019

Abstract

Complex liquids form an important class of liquid formulations used in several homecare, personal care and industrial applications. They are mixtures containing a bulk liquid phase (water or other solvents) and a dispersed phase, which is usually the phase which typically carries the active ingredient. Common examples are particle suspensions, emulsions, and dispersions of surfactants & lipid assemblies such as micelles, vesicles etc. In everyday applications such as fabric and hair conditioning, and in industrial applications such as surface modification of paper and textile, the end goal is to deposit active ingredients onto substrate surfaces. The deposition of active ingredients produces the desired surface modification effect i.e. softening, conditioning, hydrophobicity etc. Therefore, a good understanding of the liquid formulation-substrate interaction which leads to actives deposition is needed to design more efficient and cost-effective formulations.

Although the interaction of complex liquid formulations with well-defined flat solid surfaces has been investigated in earlier works, very few works have considered substrates which are closer to real-life substrates such as textiles, paper and hair. A common feature of these real-life substrates is that they are porous in nature, and the porous structure of these substrates significantly influences their interaction with the complex liquid formulation. This PhD thesis aims to investigate the processes involved in the interaction of complex liquids with porous substrates, namely, wetting, deposition and evaporation, in more detail, and elucidate the mechanisms leading to final deposition of actives.

We consider the treatment of substrates with the complex liquid formulations via two different approaches, namely, (i) via direct contact upon immersion of the substrate into the complex liquid formulation, and (ii) via spraying and subsequent wetting and evaporation of liquid formulation droplets on dry porous substrates. For the experimental study, dispersions of cationic lipid vesicles, which are commonly used in fabric softeners, have been used as model complex liquids. Vesicles of different sizes and exhibiting contrasting lipid bilayer phase behavior are used. Anionic cellulose-based substrates, namely, single cellulose fibers, porous cotton yarns, and porous cellulose fiber filter papers are used as substrates.

In the first part of the thesis, we consider the formulation-substrate interaction under fully immersed conditions wherein attractive electrostatic forces drive the deposition of cationic actives on anionic substrate surfaces. Single cellulose fibers and porous cotton yarns are used as deposition substrates. We investigate the vesicle deposition process via a combination of two techniques, namely, spectrophotometric measurement of adsorption density of vesicles on the substrate and streaming potential measurement of substrate zeta potentials. The theory of streaming potential measurements is revisited to ascertain it's applicability to our substrates. Experiments with single cellulose fibers are aimed at understanding the fundamental mechanism of vesicle deposition on cellulose surfaces. In the case of porous cotton yarns, the investigation focuses on the distribution of deposited vesicles across the porous substrate.

The investigations reveal that the cationic vesicles deposit on cellulose fiber surfaces as intact entities in contrast to the more usual case in which the deposited vesicles disintegrate forming supported lipid bilayers. The surface roughness of cellulose fibers and the lipid bilayer phase behavior was found to significantly affect the deposition process. In the case of porous cotton yarns, the lipid bilayer phase behavior was found to significantly influence the location of vesicle deposition. Additionally, the bulk electrical conductivity also influences the distribution of deposited vesicles. A new theory is proposed to explain the observed results which relates location of deposition on the porous substrates to the rates of permeation and deposition of vesicles.

The later part of the thesis focuses on the spray-application of complex liquid formulations which is of great significance to industrial applications. Cellulose fiber filter papers are used as substrates for the experiments. We investigate the interaction of vesicle dispersion droplets with these porous substrates which involves, (i) wetting of the porous substrate by the droplets, and (ii) evaporation of the bulk liquid from the wetted area and subsequent stain formation.

The wetting of porous substrates by vesicle dispersion droplets involves simultaneous spreading of the droplet over the porous substrate and imbibition of the liquid into substrate pores. The wetting process is investigated using high-speed cameras to capture both the side and top views. After the fast wetting process is over, evaporation takes effect. This process is investigated by observing the evaporating area continuously from the top using a camera. The liquid mass reduction due to evaporation is simultaneously characterized using a highly precise analytical balance. In the final stains left on the porous substrate, deposition is observed to be localized close to the periphery of the wetted spot. It is similar to the typical “coffee ring effect” obtained when colloidal droplets evaporate on flat solid surfaces. Using the experimental results, the mechanism of formation of the coffee ring effect on porous substrates is explained. Furthermore, the factors which influence the droplet evaporation process and the resultant coffee ring stain are identified.

The results of this PhD thesis are expected to be helpful in devising approaches for achieving improved performance in several applications involving complex liquid-porous substrate interactions such as fabric softening, hair conditioning, and industrial surface treatment of paper, textiles etc. The results are also significant for other applications such as transdermal drug delivery, dried spot sampling of blood and other biological samples.

Kurzfassung

Komplexe flüssige Formulierungen finden in vielen Bereichen Anwendung, zum Beispiel in Haushalts- und Körperpflegeprodukten, sowie in industriellen Prozessen. Komplexe Flüssigkeiten bestehen aus einer Bulkflüssigkeit und einer dispergierten Phase, die üblicherweise den Wirkstoff trägt. Beispiele von komplexen Flüssigkeiten sind Partikelsuspensionen, Emulsionen, Dispersionen von Tensid- und Lipidanordnungen wie Vesikeln, Mizellen etc. Das Ziel dieser Formulierungen in Anwendungen wie Gewebe-, Haarkonditionierung und in industriellen Anwendungen wie Oberflächenmodifizierung von Papier und Textilien, ist die Ablagerung von Wirkstoffen auf Substratoberflächen. Die Ablagerung von Wirkstoffen führt zu der gewünschten Oberflächenmodifizierung bzw. Erweichung, Konditionierung oder Hydrophobierung. Daher ist ein gutes Verständnis der Formulierung-Substrat-Wechselwirkung von groβer Bedeutung.

In vorherigen Arbeiten ist die Wechselwirkung von komplexen flüssigen Formulierungen vorwiegend mit glatten festen Substraten untersucht worden. Nur manche Arbeiten haben solche Substrate betrachtet, deren Eigenschaften realen Substraten wie Textilien, Papier und Haare entsprechen. Eine gemeinsame Eigenschaft von diesen realen Substraten ist die poröse Struktur, welche die Wechselwirkung mit der komplexen Flüssigkeit stark beeinflussen kann. Das Ziel dieser Dissertation, ist die komplexe Wechselwirkung von komplexen Formulierungen mit porösen Substraten zu untersuchen.

Diese Wechselwirkung wird unter zwei Umständen untersucht, nämlich (i) unter direkten Kontakt beim Eintauchen des Substrats in der komplexen flüssigen Formulierung und, (ii) Aufsprühen und anschlieβende Benetzung und Verdunstung der komplexen flüssigen Formulierung auf dem porösen Substrat. Für die experimentelle Untersuchungen werden Dispersionen aus kationischen Lipidvesikeln als Modellflüssigkeit verwendet. Dabei werden anionische Substrate, nämlich einzelne Cellulosefasern, poröse Baumwollgarne und poröse Cellulosefaser-filterpapiere werden verwendet.

In dem ersten Teil der Dissertation wird die Wechselwirkung unter direkten Kontakt beim Eintauchen des Substrats in der komplexen flüssigen Formulierung untersucht, wobei die attraktiven elektrostatischen Kräfte die Ablagerung von kationischen Wirkstoffe auf anionischen Substratoberflächen antreiben. Einzelne Cellulosefasern und porösen Baumwollgarne werden als Substrat verwendet. Der Vesikelablagerungsprozess wird durch eine Kombination von zwei Methoden, nämlich spektrophotometrische Messung der Adsorption und Strömungspotentialmessung von Substrat-Zeta-Potential untersucht. Die Theorie von Streaming-Potentialmessungen wird überprüft, um die Anwendbarkeit für unsere Substrate festzustellen. Die Versuche mit einzelnen Cellulosefasern zielen darauf ab, den grundlegenden Mechanismus des Vesikelablagerungprozesses auf Celluloseoberflächen zu verstehen. Bei porösen Baumwollgarnen liegt der Schwerpunkt bei der Verteilung von abgelagerten Vesikeln in dem porösen Substrat.

Diese Untersuchungen ergeben, dass die kationischen Vesikeln sich intakt auf Cellulosefaser-Oberflächen adsorbieren. Das steht im Gegensatz zu dem üblichen Fall, bei dem die abgelagerten

Vesikeln sich zersetzen. Es wird festgestellt, dass die Oberflächenrauheit von Cellulosefasern und die Vesikel-Lipiddoppelschichtphase einen signifikanten Einfluss auf den Ablagerungsprozess haben. Bei porösen Baumwollgarnen wird festgestellt, dass die Vesikel-Lipiddoppelschichtphase und die elektrische Leitfähigkeit der Bulkflüssigkeit die Verteilung von abgelagerten Vesikeln signifikant beeinflussen. Eine neue Theorie wird vorgeschlagen, um die beobachteten Ergebnisse zu erklären.

Der zweite Teil der Arbeit konzentriert sich auf die Wechselwirkung zwischen Tropfen aus komplexen flüssigen Formulierungen und porösen Substraten. Dieser Art von Wechselwirkung ist für industrielle Anwendungen von groβer Bedeutung. Für die Experimente werden Cellulosefaser-Filterpapiere als Substrat eingesetzt. Wir untersuchen die Wechselwirkung von Vesikel-Dispersionstropfen mit porösen Substraten, wobei (i) das poröse Substrat benetzt wird, und (ii) die Verdunstung der Bulkflüssigkeit aus dem benetzten Bereich zu einer Fleckenbildung führt.

Der Benetzungsprozess beinhaltet die parallel ablaufende Tropfenausbreitung auf dem porösen Substrat und die Imbibition der Flüssigkeit in die Substratporen. Der schnelle Benetzungsprozess wird mithilfe von Hochgeschwindigkeitskameras von der Seite und von Oben erfasst. Nach Beendigung des schnellen Benetzungsprozesses, tritt der Verdunstungsprozess in Kraft. Die Verdunstungsrate wird durch eine Bestimmung der Reduzierung der Flüssigkeitsmasse mithilfe einer hochpräzisen Analysenwaage charakterisiert. Gleichzeitig wird der Prozess kontinuierlich mit einer Kamera von oben beobachtet. Bei den Flecken, die auf dem porösen Substrat zurückbleiben, ist zu beobachten, dass die Ablagerung am Rand des benetzten Bereiches konzentriert ist. Das ist vergleichbar zu dem typischen "Kaffeering-Effekt" von kolloidalen Tropfen auf ebenen festen Oberflächen. Anhand der experimentellen Daten wird der Mechanismus der Bildung des Kaffeeringeffekts auf porösen Substraten erläutert. Darüber hinaus werden die Faktoren, die den Verdunstungsprozess und die resultierenden Kaffeeringflecken beeinflussen, identifiziert.

Die Ergebnisse dieser Dissertation sollen bei der Erzielung einer verbesserten Leistung in mehreren Anwendungen, die komplexe Wechselwirkungen zwischen Flüssigkeit und poröse Substrat beinhalten, hilfreich sein. Die Erkenntnisse der Arbeit sind auch für andere Anwendungen wie transdermale Arzneimittelabgabe und Trockenpunktentnahme von Blut von groβer Bedeutung.

Acknowledgments

When I set forth the journey to obtain my PhD, I had little knowledge that I would be mentored by such inspiring, motivating and helpful people. I am extremely grateful to **Apl. Prof. Dr. Sc. Tatiana Gambaryan-Roisman** (Institute of Technical Thermodynamics, TU Darmstadt) and **Dr. Joachim Venzmer** (Evonik Nutrition & Care GmbH) for having given me the opportunity to work on this wonderful research project. Their supervision played the biggest role in shaping me as a researcher. I am thankful to **Prof. Peter Stephan**, the director of our Institute, for fostering a great working environment in the institute. I cannot thank enough **Dr. Jochen Kleinen** who guided me closely through the difficult times early on in my PhD. I thank **Dr. Verena Dahl** for her valuable suggestions and feedback. They were always there when I needed help and at the same time provided me with the highest quality of technical supervision.

I thankful to the Marie Curie Initial Training Network **"Complex Wetting (CoWet)"** for the financial support and the several training activities which helped me to grow. I am thankful to all the supervisors at CoWet whom I got to learn a lot from. I am specially grateful to **Dr. Günter Auernhammer** & **Prof. Hans Jürgen Butt** (Max Plank Institute of Polymer Research, Mainz), and **Prof. Victor Starov** (Loughborough University) for giving me the opportunity to carry out secondments at their research groups.

I am thankful to all the wonderful colleagues whom I got the opportunity to work with. This includes all of my co-fellows at CoWet and my colleagues at Evonik & TU Darmstadt. **Ehsan**, **Vignesh** and **Alireza**, I really enjoyed our cooperations and discussions covering a broad range of topics. It was an enjoyable experience sharing my office with **Jella Winterling** and **Josephine Meidinger**.

I am grateful that I had the support of capable technical staff all throughout my PhD research both at Evonik Nutrition & Care GmbH as well as TU Darmstadt. I would like to specially thank **Iwona Winter**, **Karin Fuerch**, **Robert Schrod** and **Roland Berntheisel**.

This thesis would not exist in it's present form if it wasn't for the sincere efforts of my students, **Janita Braun**, **Nasar Patel** and **Rakshitaa Geetha Mohan**. Their contributions specially in the area of investigations on coffee ring stain formation on porous substrates is commendable.

I am grateful to all of my German language instructors, specially **Christina Braun**, under whose guidance I undertook my journey from almost non-existent German skills to the C1-level.

In between stress at work, failed experiments and rejected papers, it is with family and friends that I found my inner peace. My parents, my brother and my sister-in-law always believed in me and motivated me to give my best. My friends **Anitha**, **Vikram**, **Pratik**, **Vidya**, **Kshitij**, **Hari Om** and **Aishwarya** were always there as a strong pillar of support.

Darmstadt, 11.11.2019 Abhijeet Kumar

Contents

1. Introduction **1**
- 1.1. Motivation of the thesis . . . 1
- 1.2. Complex liquids . . . 3
  - 1.2.1. Types of complex liquid formulations . . . 3
  - 1.2.2. Application methods of complex liquid formulations on substrates . . . 3
  - 1.2.3. Other applications involving complex liquid-porous substrate interaction . 5
- 1.3. Open questions and challenges . . . 6
- 1.4. Complex liquids, substrates and experimental methods used in this thesis . . . 7
- 1.5. Outline and scope of the thesis . . . 7

2. Complex liquids and solid substrates used in this thesis **9**
- 2.1. Cationic vesicle dispersions . . . 9
  - 2.1.1. What are vesicles ? . . . 9
  - 2.1.2. Esterquats . . . 10
  - 2.1.3. Preparation of esterquat vesicle dispersions . . . 10
  - 2.1.4. Properties of the prepared vesicle dispersions . . . 11
- 2.2. Porous and non-porous solid substrates . . . 14
  - 2.2.1. Single cellulose fibers . . . 14
  - 2.2.2. Porous cotton yarns . . . 14
  - 2.2.3. Porous cellulose fiber filter papers . . . 15

3. Zeta potential characterization of fiber plugs and porous substrates **19**
- 3.1. Background of streaming potentials and streaming current measurements . . . 19
- 3.2. Streaming potential and streaming current measurements on porous substrates . . 20
- 3.3. Fundamental theory of geometry effects on generation of I_{str} and U_{str} . . . 22
  - 3.3.1. Fundamental microscale relationship for I_{str} generation . . . 23
  - 3.3.2. General expressions for an arbitrary porous sample . . . 25
- 3.4. Application to model sample geometries . . . 28
  - 3.4.1. Capillaries with non-uniform cross-section . . . 28
  - 3.4.2. Square fiber array (model porous media) . . . 32
  - 3.4.3. Implications of obtained results in practical use . . . 37
- 3.5. Summary . . . 40

4. Deposition of cationic vesicles on single anionic cellulose fibers **41**
- 4.1. State-of-the-art . . . 41
- 4.2. Materials and Methods . . . 42
  - 4.2.1. Materials . . . 42
  - 4.2.2. Spectrophotometric determination of esterquat concentrations . . . 43
  - 4.2.3. Streaming potential measurements . . . 43
  - 4.2.4. Deposition experiments . . . 44
  - 4.2.5. Fluorescence microscopy visualization of deposited vesicles . . . 44
- 4.3. Investigations on colloidal deposition via streaming potential measurements . . . 45

4.4. Results and Discussion . . . 46
4.4.1. Applicability of Helmholtz-Smoluchowski equation to fiber plugs . . . 46
4.4.2. Establishing intact deposition of vesicles . . . 47
4.4.3. Vesicle deposition on single viscose fibers (smooth and uniformly shaped) 49
4.4.4. Vesicle deposition on rough cotton fibers . . . 52
4.5. Summary . . . 55

5. Deposition of cationic vesicles on porous cotton yarns 57
5.1. Background of vesicle deposition on porous substrates . . . 57
5.2. Materials and Methods . . . 59
5.2.1. Materials . . . 59
5.2.2. Determination of bulk lipid concentrations . . . 60
5.2.3. Streaming potential measurements . . . 60
5.2.4. Deposition experiments . . . 60
5.3. Theory . . . 62
5.3.1. Qualitative model of permeation and deposition of colloids on porous substrates . . . 62
5.3.2. Theory of streaming potential measurements on porous yarns . . . 64
5.4. Results and Discussion . . . 66
5.4.1. Deposition kinetics of vesicles on single cotton fibers . . . 66
5.4.2. Equilibrium deposition of vesicles on cotton yarns . . . 68
5.5. Summary . . . 72

6. Spreading and imbibition of vesicle dispersion droplets on porous substrates 75
6.1. Background of liquid droplet spreading on porous substrates . . . 75
6.2. Partial vs. Complete wetting case . . . 77
6.3. Materials and Methods . . . 77
6.3.1. Materials . . . 77
6.3.2. Spreading experiments . . . 78
6.4. Results and Discussion . . . 79
6.4.1. Droplet spreading kinetics . . . 79
6.4.2. Non-dimensionalized droplet spreading kinetics . . . 80
6.4.3. Secondary radial liquid penetration . . . 82
6.5. Summary . . . 82

7. Evaporation of imbibed complex liquids droplets on porous substrates 85
7.1. Introduction to liquid droplet evaporation on porous substrates . . . 85
7.2. Materials and Methods . . . 85
7.2.1. Materials . . . 85
7.2.2. Evaporation experiments . . . 86
7.2.3. Elimination of the zero drift . . . 86
7.3. Data processing and analysis . . . 88
7.3.1. Analysis of images of the evaporating area . . . 88
7.3.2. Analysis of the final stains . . . 91
7.3.3. Analysis of the mass variation data . . . 92
7.4. Model for liquid evaporation from wetted areas on porous substrates . . . 93
7.5. Results and Discussions . . . 94
7.5.1. Initial evaporation rates from wetted areas . . . 94
7.5.2. Simultaneous plateau diameter and liquid mass variation during evaporation 97

7.5.3. Characteristics of coffee ring stains formed on porous substrates 98
7.5.4. Schematic model for evaporation and coffee ring formation from wetted areas 100
7.5.5. Influence factors in the final stain formation 102
7.6. Summary 104

8. Conclusions and Outlook **107**
8.1. Outlook 108

Bibliography **111**

A. Appendix **127**

List of Symbols and Abbreviations **129**

List of Figures **131**

List of Tables **133**

Resume **135**

Publications **137**

1 Introduction

1.1 Motivation of the thesis

Complex liquid formulations form the primary constituent of several homecare and personal care products such as fabric softeners, hair conditioners and skin lotions etc. Some of these everyday use products and their applications are shown in Fig.1.1. In the industry, complex liquid formulations are often used for the surface modification of textile, paper and other substrates. These formulations contain a bulk liquid phase (water or any other solvent) and a dispersed phase in which the active ingredients are encapsulated. When substrates are treated with these formulations, the active ingredients are deposited on substrate surfaces imparting them the desired surface properties such as softness or hydrophobicity.

An important question concerning such treatments is : what are the factors that determine their effectiveness ? Certainly, the molecular properties of the active ingredients would play an important role. However, from a formulation perspective, the properties such as size, shape and surface charge of dispersed ingredients, viscosity and electrical conductivity of the liquid formulation are important to consider. Depending upon the mode of application, the formulation-substrate interaction could involve processes such as deposition on solid surfaces, colloidal transport through pores, droplet spreading and imbibition as well as liquid evaporation. In order to explain the effect of formulation properties on the final performance, it is important to clearly understand the fundamental aspects of liquid formulation-substrate interactions in various treatment methods.

The interaction of complex liquid formulations with flat and non-porous solid substrates has been investigated in several earlier works. However, very few works have used substrates whose properties are comparable to that of real-life substrates such as textiles, paper, human hair and outer skin tissue. An important common morphological feature of these real-life substrates is that they have a porous structure. The porous structures of these substrates is easily identifiable from their magnified images shown in Fig. 1.2. The porous structure of substrates significantly influences their interactions with complex liquid formulations. For instance, when the mode of action involves deposition, deposition could occur both on external as well as internal substrate surfaces when the substrate is porous. The distribution of actives deposition between internal and external surfaces could significantly influence the final performance. Similarly, in applications where the mode of application involves spraying, the porous substrate structure leads to additional phenomena such as capillary flows and imbibition which do not exist on simple flat surfaces.

The main motivation of the PhD thesis is to investigate the complex liquid-substrate interaction with a focus on the role played by the formulation properties and porous substrate morphologies. The different processes constituting this interaction are investigated with the goal of elucidating the phenomena leading to final performance. An understanding of the interaction is thereafter



Source of images (A) , (B) and (C) : Vernel, Unilever and LÓreal
Source of Image (D) : https://downy.com/en-us/fabric-conditioner-tips/how-to-use-downy/how-to-use-liquid-fabric-softener/
Source of Image (F) : https://www.eucerin.co.uk/about-skin/basic-skin-knowledge/skins-ph/

Figure 1.1.: (A),(B) and (C) : Common fabric softener, hair conditioner and skin care products, (D) Dosing of a fabric softener formulation into a washing machine, (E) and (F) Representation of the everyday use of hair conditioner and skin care lotions

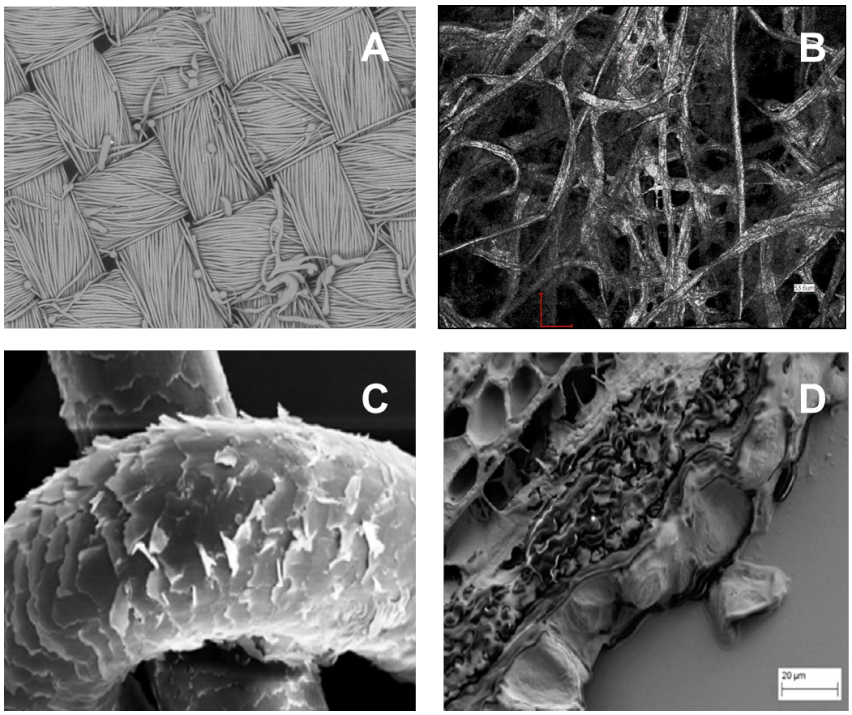

Figure 1.2.: Porous structures of textile (A), paper (B), hair (C) and the human skin epidermis (D) as observed via different microscopy techniques. Fig. 1(C) has been reprinted with permission from Gerace et. al. [1] Copyright © 2017, Elsevier. Figure 1(D) has been reprinted with permission from Sjövall et. al. [2] Copyright © 2014, American Chemical Society.

used to explain the how different formulation and substrate properties influence the effectiveness of the formulations.

1.2 Complex liquids

In this work, the term “complex liquids” applies to mixtures of two phases, namely, a bulk liquid phase and a dispersed phase. Particle dispersions, polymer solutions, emulsions and dispersions of surfactant or lipid assemblies such as vesicles, micelles, and several other liquids come under this category.

1.2.1 Types of complex liquid formulations

The type of complex liquid that a given active ingredient is formulated as depends upon both, the intended goals of the formulation as well as the physico-chemical properties of the active ingredient such as its melting point, solubility in water or oil phases and its hydrophobic or hydrophilic nature. Active ingredients such as metals, inorganic/, organic compounds, polymers etc. that exist in the solid state at room conditions and are insoluble in water could be typically formulated as aqueous particle dispersions. A liquid active ingredient which is insoluble in water could be formulated as an aqueous emulsion. In the case of fabric and hair conditioners, where the aim of the formulation is to deposit active ingredients on anionic textiles and hair, the active ingredients are encapsulated inside a dispersed phase with cationic surface charge such as cationic vesicles or droplets. The basic composition of complex liquids and some of their important classes are shown in Fig.1.3.

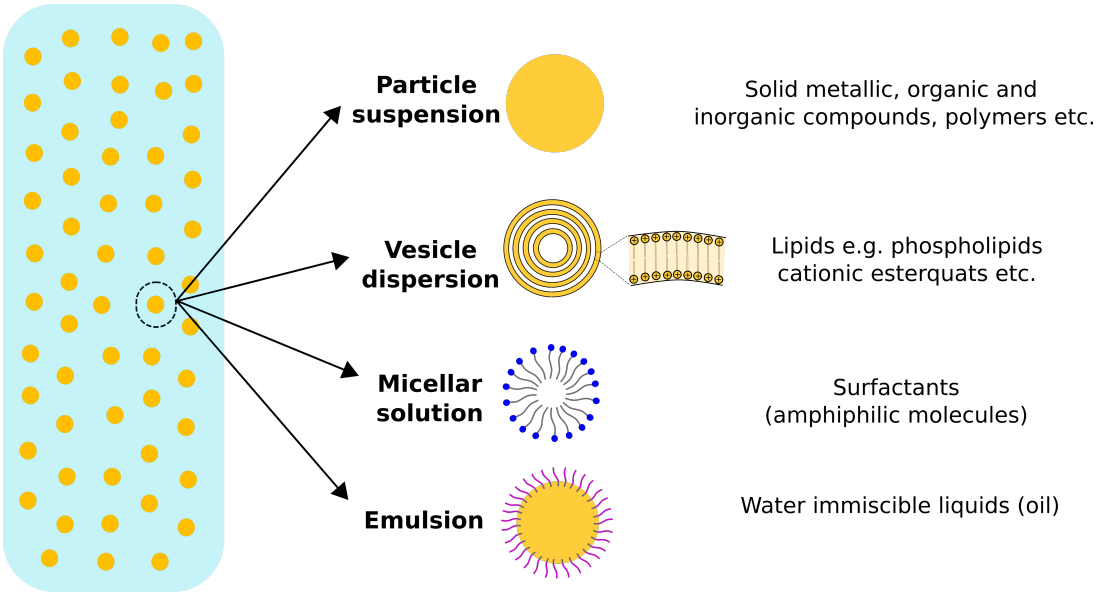

Figure 1.3.: Schematic representation of the composition of complex liquids and some of the important classes of dispersed ingredients

1.2.2 Application methods of complex liquid formulations on substrates

The chosen method for application of a complex liquid formulation depends on the intended purpose of the formulation as well as the properties of the formulation and the substrate. One approach, typically employed in the application of creams and lotions on skin, is the forced deposition of actives via direct application. This forced application method is not viable for large-scale industrial processes. In the case of fabric and hair conditioners, the actives are

deposited from dilute formulations, and the hence, the method of application needs to be decided accordingly. The application methods that have been considered in this thesis are shown schematically in Fig. 1.4(A) and (B). We consider the treatment of substrates with the complex liquid formulations via two different approaches, namely, (i) via batch deposition upon immersion of the substrate into a dilution of the complex liquid formulation, and (ii) via spraying and subsequent wetting and evaporation of the liquid formulation on dry substrates.

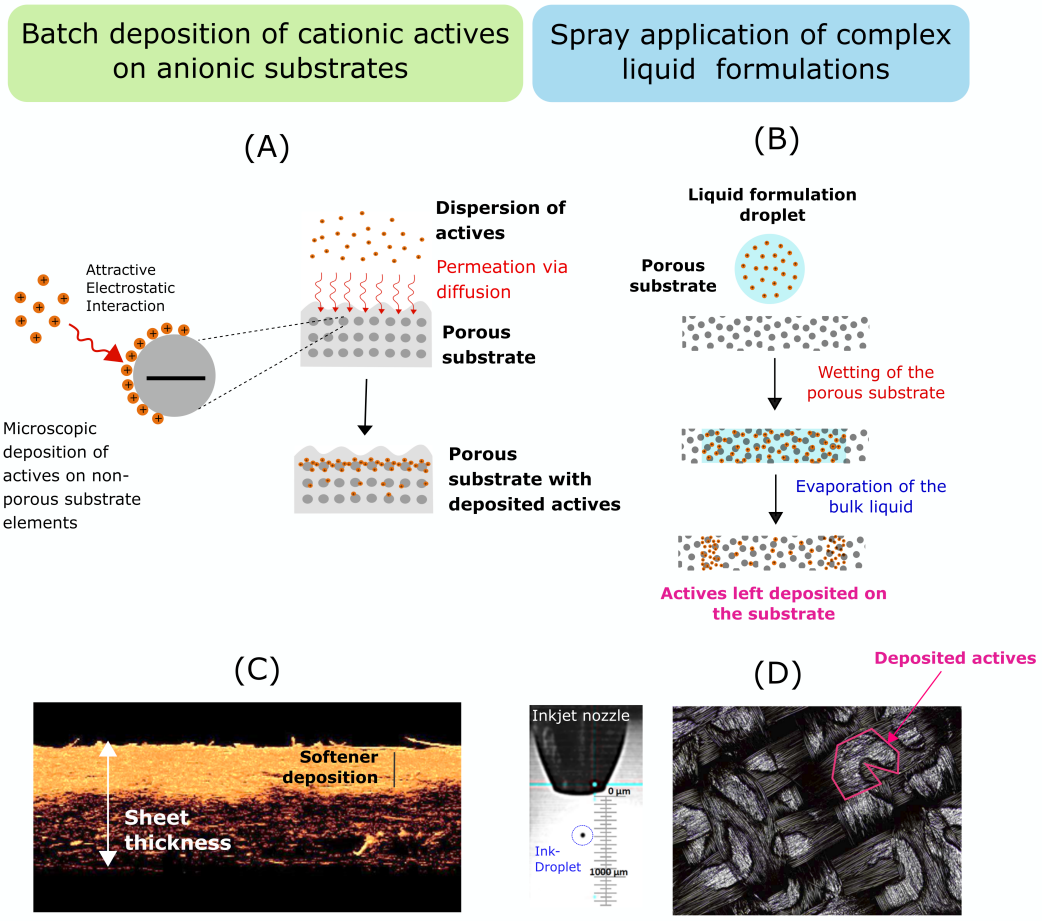

Figure 1.4.: (A) and (B) : Schematic representation of methods for treatment of substrates with complex liquid formulations, (C) Cross-section of a textile sheet treated with fluorescent labelled cationic softener actives (Image copyright © Evonik Nutrition & Care GmbH), (D) Deposition of metallic nanoparticles on textile via treatment with metallic nanoparticle dispersion droplets (Image copyright © Marco Cirelli, University of Twente & Verosol)

The batch deposition method is well suited for applications such as fabric softening involving the deposition of cationic actives on anionic substrate surfaces, wherein attractive electrostatic interactions can significantly influence the deposition process. An example is shown in Fig. 1.4(C) where fluorescent labelled cationic actives deposited on a textile sheet are visualized. On the other hand, the spray application method is suitable for industrial applications where the substrates need to be processed at a very fast rate and hence a continuous process such as spray

application is more suited. An example is shown in Fig. 1.4(D) where a textile sheet has been "metallized" via treatment with droplets of metallic nanoparticle dispersions.

1.2.3 Other applications involving complex liquid-porous substrate interaction

The interaction of complex liquids with porous substrates is important in several biomedical applications such as the dried spot sampling of blood and other biological liquids. The dried spot sampling technique involves dripping a small volume of the liquid into a filter paper creating a small wetted spot as shown in Fig.1.5(A). The spot is thereafter dried and subsequently analyzed in the laboratory. For the analysis, a small area on the spot is punched out and the dried blood is eluted out from the punched spot into a buffer [3]. Although it is a relatively new technique, it is already used for the analysis of a number of different species [4].

The main problem associated with this technique is the inhomogeneous distribution of ingredients in the dried spots after evaporation, wherein a higher concentration is found near the edge of the spot as compared to its center [3]. Therefore, the accuracy of this method depends upon where the final spot for analysis is punched out from. A typical dried blood spot is shown in Fig. 1.5(B), where the inhomogeneity in the spot is identifiable. The inhomogeneous distribution leads to inaccuracies in the measured concentrations.

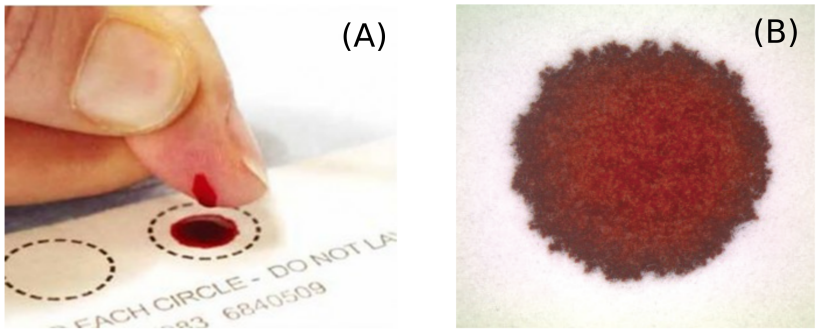

Image source (A) : https://vitas.no/dried-blood-spot-testing

Figure 1.5.: (A) Sampling of patient's blood on a filter paper and (B) A typical dried blood spot with inhomogeneous deposition (Image reproduced from Lenk et. al. Bioanalysis (2015) 7(16), 1977-1985) with permission

The physical phenomena underlying this technique area fundamentally similar to the spray application of complex liquids on porous substrates as described in Section 1.2.2. In earlier works, it has been established that the formation of these peripheral rings is linked to the evaporation process. The mechanism of formation of these rings, and how their formation is influenced by various substrate and liquid properties is still not well understood [5]. Therefore, a profound understanding of the formation of the dried spot is necessary for devising approaches for obtaining more accurate measurements using this technique.

1.3 Open questions and challenges

When it comes to understanding and controlling actives deposition on substrates, several open questions and associated challenges still exist. The important aspects of theses treatments which are of significant research interest are laid out in Fig. 1.6.

In order to understand the deposition of cationic actives on porous substrates such as porous textile and hair, it is firstly important to understand how the cationic actives interact with anionic non-porous substrate elements. Typically, when the substrate and the dispersed elements are oppositely charged, attractive electrostatic interaction is responsible for actives deposition. The mechanism of such deposition processes on simple flat solid surfaces has been investigated in earlier works and has been postulated to follow the "Random Sequential Adsorption model". However, much less is known when it comes to the deposition of complex dispersed phases such as cationic vesicles or oil droplets on morphologically complex substrates such as textile fibers. One of the main goals of this work is to further the general understanding of such deposition processes.

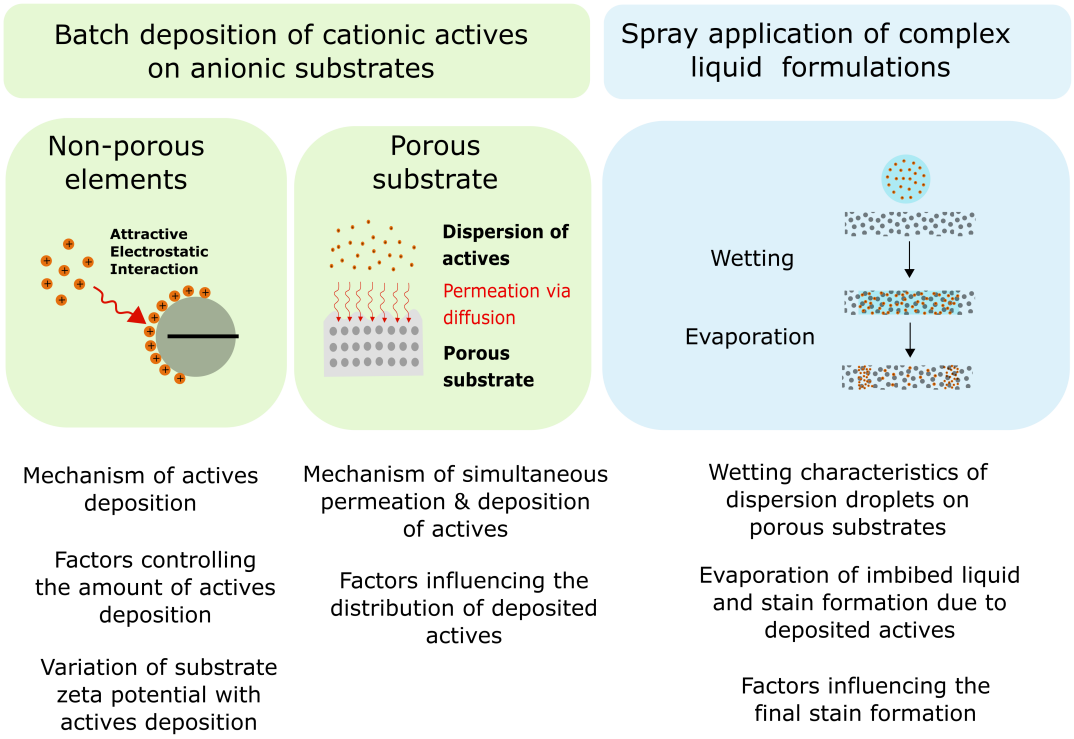

Figure 1.6.: Layout of the common areas of investigation in the application of complex liquid formulations on porous substrates

The next level of complexity is when the deposition substrate in the batch deposition process has a porous structure, where the actives could deposit on both external as well as internal substrate surfaces. Therein the mechanism involves simultaneous permeation of actives into the substrate through pores as well as the deposition of actives on substrate surfaces. The mechanism of such deposition processes is still not well elucidated and even less is known about how the formulation properties affect the final actives distribution. This can be attributed to the difficulty in experimentally characterizing deposition on the internal surfaces of a porous substrate using

conventional methods [6–8]. However, in this work, this challenge is overcome using a novel streaming potential measurements-based approach which enables us to distinguish between deposition on external and internal substrate surfaces. This experimental approach is used to obtain new insights into the factors which influence the final distribution of deposited actives.

In spray application of formulations on porous substrates, several open questions still exist related to both the wetting and evaporation stages of the process. For example, it is not very well established if droplet wetting on the porous substrate produces a uniformly or a non-uniformly filled wetted area. Furthermore, the kinetics of complex liquid droplet spreading on porous substrates has been examined only in a few earlier works and only for a few complex liquid types [9, 10]. The evaporation stage which finally leads to deposit formation has also received very little attention in scientific literature. The mechanism governing the evaporation of such wetted spots has not been comprehensively investigated yet.

1.4 Complex liquids, substrates and experimental methods used in this thesis

In this thesis, a special class of complex liquids, namely esterquat vesicle dispersions, have been used for the experimental investigations. Esterquat vesicles are commonly used in fabric softener formulations and have positive surface charges due to the presence of cationic quaternary ammonium head groups in esterquat molecules. Vesicles of different sizes and different lipid bilayer phase behavior are used. Single cellulose fibers and porous cotton yarns are used as substrates for the batch deposition experiments. Cellulose fiber filter papers are used as substrate for experiments aimed at investigating complex liquid droplet wetting and evaporation.

The experimental methods used in this thesis to study the batch deposition processes includes, streaming potential measurements to characterize the zeta potential of deposition substrates and UV-Vis spectrophotometry to quantify the mass deposition. The spreading and evaporation processes are investigated via direct imaging using high speed cameras wherever necessary. Furthermore, the loss of mass during evaporation is measured using a precise analytical balance to obtain the mass evaporation kinetics.

1.5 Outline and scope of the thesis

The thesis is divided into several self-contained chapters which covers different important focus areas. The structure is so chosen so as to be able to focus individually on the different areas of investigation covered in this thesis. A summary of the existing literature related to specific scientific questions are also included in each of the chapters separately.

In Chapter 2, detailed information about the preparation and characterization of the complex liquids is provided. Along with it, the substrates used in the different experimental studies are outlined.

In Chapter 3, the theory underlying the streaming potential measurement technique which has been used in the thesis to characterize deposition on single cotton fibers and porous cotton yarns is desribed. A new theory is proposed which is used to evaluate the applicability of this approach

to our system for which the commonly used Helmholtz-Smoluchowski equation is not directly applicable.

In Chapter 4, the deposition of cationic vesicle deposition on anionic single cellulose fibers is described. The mechanism of vesicle deposition on anionic cellulose surfaces is elucidated. The roles played by vesicle size, polydispersity and substrate surface roughness are described.

In Chapter 5, our investigations on the simultaneous permeation and deposition of vesicles on porous substrates are described. A new qualitative model is proposed to describe the process mechanism. The role played by vesicle lipid bilayer phase behavior and interparticle electrostatic interactions is described.

In Chapter 6, the results of wetting of porous substrates by vesicle dispersion droplets are presented. The kinetics of simultaneous spreading and imbibition of vesicle dispersion droplets on porous substrates is described. Two characteristically different types of droplet spreading behavior, namely, complete and partial wetting cases, are reported.

In Chapter 7, the fundamental investigations on the evaporation of wetted spots on the porous substrates are described. The variations observed in the evaporating spot together with the liquid mass variation helps reveal the mechanism of liquid evaporation and stain formation. The investigations on the influence of factors such as vesicle concentration, pore size, substrate geometry and temperature on the stain formation are described. The strategies that could be employed the control the intensity of the coffee rings on porous substrates are discussed.

In Chapter 8, the experimental results and conclusions are summarized. The significance of the present results in practical applications are described. The themes of possible future works are laid out.

2 Complex liquids and solid substrates used in this thesis

This chapter describes the complex liquid formulations and the solid substrates used in different experimental investigations in this thesis. This chapter is divided into two parts. Firstly, the preparation and properties of the esterquat vesicle dispersions used for the experiments in this thesis as model complex liquids is described. It is followed by a description of the used substrates, namely, single cellulose fibers, porous cotton yarns and porous cellulose fiber filter papers.

2.1 Cationic vesicle dispersions

2.1.1 What are vesicles ?

Lipids are surfactant-like amphiphilic molecules comprised of twin hydrophobic tails and one hydrophilic head group, and have the tendency to form bilayer assemblies when dispersed in water. Closed lipid bilayers which enclose a certain volume of water are called vesicles or liposomes. A vesicle could either be composed of a single lipid bilayer (unilamellar) or multiple lipid bilayers (multilamellar) as shown in Fig. 2.1 [11]. The lipid molecules constituting the vesicles could vary in terms of the properties of the hydrophobic tails and the hydrophilic head groups imparting different properties to the vesicles. Furthermore, the size of vesicles depends on both, the properties of lipid molecules as well as the preparation method.

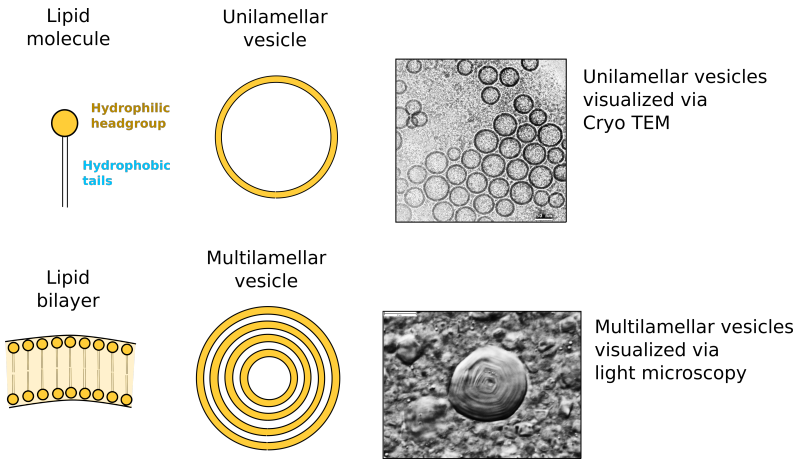

Figure 2.1.: Schematic representation of the structures of lipid molecules, lipid bilayers, unilamellar and multilamellar vesicles. Typical structures of unilamellar and multilamellar vesicles as observed via cryo-TEM and light microscopy, respectively, are also shown. The Cryo-TEM image of unilamellar vesicles has been reprinted with permission from Battersby et. al. [11] Copyright © 2017, Elsevier.

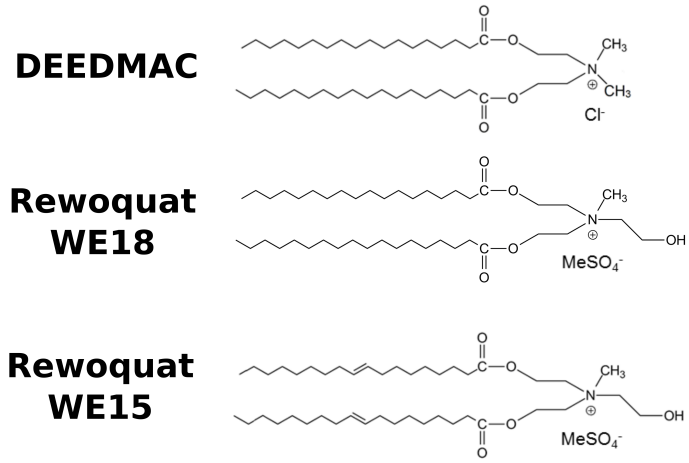

Figure 2.2.: Molecular structures of the esterquats used for preparing the vesicles used in the thesis [12, 13]

2.1.2 Esterquats

Esterquats are a special class of lipids which have an ester group present in their hydrophobic chains. The hydrophilic headgroup of esterquats is a cationic quaternary ammonium group. In this work, three different esterquats, namely, DEEDMAC, Rewoquat WE18 and Rewoquat WE15 are used for preparing the vesicles. The molecular structures of these esterquats are shown in Fig. 2.2. The esterquats were synthesized at Evonik Nutrition & Care GmbH. While the esterquats, DEEDMAC and Rewoquat WE18 are almost identical and they both exist in the solid state at room temperature, the esterquat Rewoquat WE15 exists in the liquid state.

2.1.3 Preparation of esterquat vesicle dispersions

Vesicles of two different size ranges, large ($d_{avg} \sim 10\ \mu m$) and small ($d_{avg} < 1\ \mu m$), were prepared using each of the three esterquats. Additionally, vesicles doped with a fluorescent dye were also prepared so that they could also be visualized via fluorescence microscopy.

2.1.3.1 Preparation of large vesicles

The standard large vesicles, as used in commercial fabric softener formulations, were prepared using the melt-dispersion method.

DEEDMAC and WE18 vesicles

A certain mass of esterquat (80 g) was melted by heating above its melting point (75 °C for DEEDMAC and 60°C for WE18). The liquid esterquat was then added steadily to a batch of pre-heated water (720 g) with an agitator being used to continuously mix the ingredients. The temperature was kept fixed at 60 °C for the first 20 minutes of mixing during which the molten molecules disperse in water, form bilayers and assemble into large multilamellar vesicles [14, 15]. Thereafter, the batch was placed in a cold water bath and mixed until it cooled down to room

temperature. The properties of DEEDMAC and WE18 vesicles are very similar to each other due to their very similar molecular properties.

WE15 vesicles
WE15 vesicles were prepared following a similar procedure as DEEDMAC and WE18 vesicles, with the difference being that WE15, being liquid at room temperature was heated only mildly to 40 °C before mixing with water (also preheated to 40 °C).

2.1.3.2 Preparation of small vesicles

The large vesicles prepared by the melt dispersion method were put through a size-reduction process to prepare vesicles smaller than 1 μm. Size-reduction was carried out via microfluidization using the M-110Y Microfluidizer from Microfluidics Corp. USA. DEEDMAC and WE18 vesicles were preheated to 75 °C and 60°C, respectively, before microfluidization, whereas WE15 vesicles were used at room temperature. The dispersions were fed in the device, operated at an applied pressure of 250 bar, and multiple passes (2-3 times) were carried out to attain the desired size-reduction.

2.1.3.3 Preparation of fluorescently doped vesicles

Fluorescently doped vesicles were prepared by dissolving an oil-soluble fluorescent dye in the esterquat melt to a concentration of 100 ppm prior to vesicle preparation. Lumogen F (BASF) was chosen as the suitable dye because it is extremely hydrophobic, and therefore gets localized inside lipid bilayers when vesicles are formed, resulting in vesicles with uniform bulk fluorescence. As the concentration of Lumogen F used is very low, it is expected to have negligible effect on vesicle properties.

2.1.4 Properties of the prepared vesicle dispersions

The prepared vesicles were analyzed using different techniques to characterize their properties such as size distribution, viscosity, zeta potential etc.

2.1.4.1 Vesicle sizes and shapes

The size distributions of vesicle dispersions characterized via laser diffraction using a Malvern Mastersizer 3000 are shown in Fig. 2.3. It could be remarked from the size distributions that all the vesicle dispersions are significantly polydisperse.

As the esterquats, DEEDMAC and WE18 naturally exist in the solid state at room temperature, the lipid bilayers formed by them in the vesicles exist in “solid-gel” phase. On the other hand, as the esterquat WE15 exists in the liquid phase at room temperature, it forms “liquid-crystalline” phase bilayers. This difference in phase behavior of lipid bilayers results in significant differences in the shapes of vesicles. The liquid-crystalline WE15 vesicles are smoothly shaped and round, whereas the solid-gel DEEDMAC and WE18 vesicles exist as angular, crumpled spheres with sharp edges as a result of the stresses generated when their bilayers undergo a transition from the liquid-crystalline to the solid-gel phase during the cooling stage of their preparation [16]. The

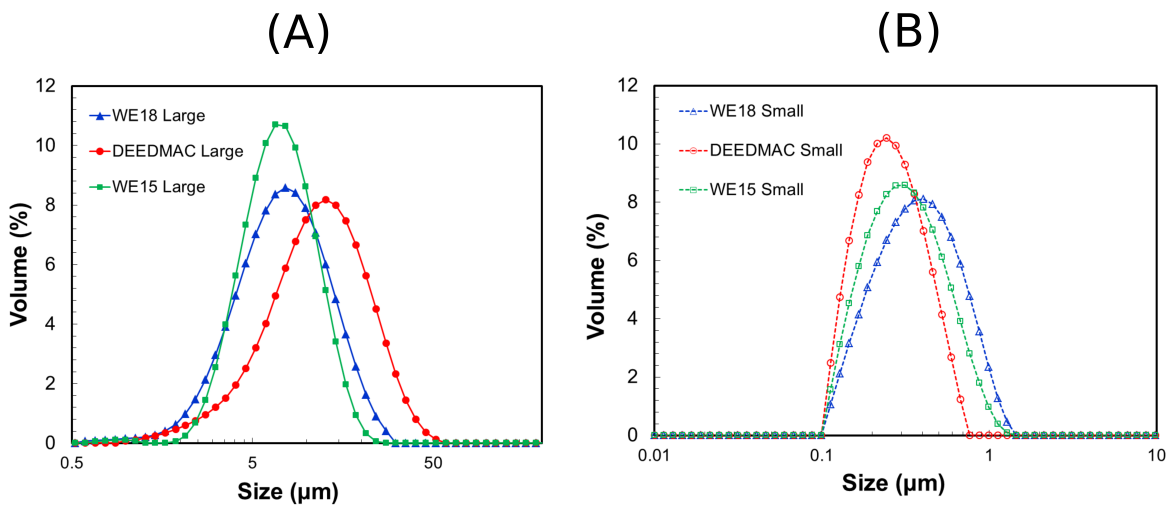

Figure 2.3.: Size distributions of large (A) and small (B) DEEDMAC, WE18 and WE15 vesicle dispersions

large vesicles as visualized using optical microscopy are shown in Fig. 2.4 where the contrasting shapes of large solid-gel and liquid-crystalline vesicles can be identified. The difference in shapes of the microfluidized vesicles were identified by imaging them via cryo-electron microscopy which is also shown in Fig. 2.4. The samples for cryo-electron microscopy were prepared using the freeze fracture technique.

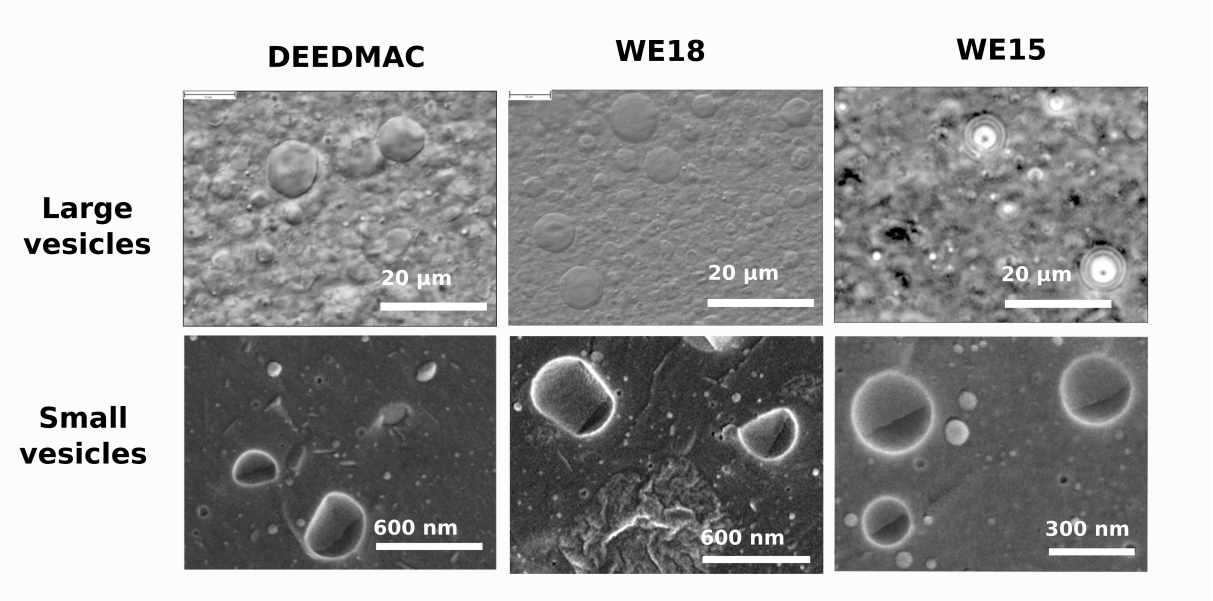

Figure 2.4.: Large and small DEEDMAC, WE18 and WE15 vesicles as observed via optical microscopy and cryo-electron microscopy, respectively.

2.1.4.2 Vesicle zeta potentials

The zeta potential of vesicles was measured via electrophoretic mobility characterization on a Malvern Zetasizer Nano ZS, and found to be + 60 mV (±10 mV) for all the vesicle dispersions. The measurements were carried out at a bulk electrical conductivity of 1 mS/cm with vesicle

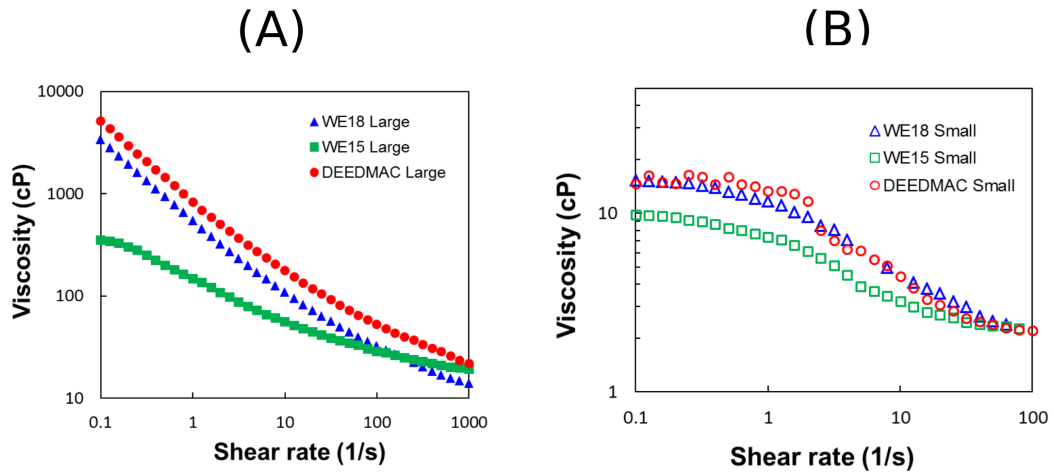

Figure 2.5.: Dynamic viscosity vs. shear rate profiles of the large (A) and small (B) vesicle dispersions at a lipid concentration of 8%.(Image reproduced with permission from Kumar et. al. [17])

dispersions diluted with Millipore water to concentration levels of 50 ppm. Comparable zeta potential values of different vesicle types indicate similar packing of cationic head groups in lipid bilayers in all the vesicles.

2.1.4.3 Dynamic viscosity of vesicle dispersions

The dynamic viscosity of the prepared vesicle dispersions was characterized via measurements at different shear rates (0.1 to 100 s^{-1}) using the AR-G2 rheometer from TA Instruments. The viscosity vs. shear rate profiles of all the vesicle dispersions are shown in Fig. 2.5.

It is to be noted that the viscosity of large vesicle dispersions is significantly higher than that of the small vesicle dispersions. All the vesicle dispersions behave as non-newtonian liquids and exhibit shear thinning behavior. Furthermore, the viscosity of the vesicle dispersions is measured at very low lipid concentratito estimate the lipid density of vesicles as shown in the following section.

2.1.4.4 Vesicle lipid density

Vesicle lipid density, defined as the lipid mass per unit vesicle volume, depends on vesicle properties such as inter-lamellar spacing and packing efficiency of lipids in bilayers, and can vary depending upon the preparation method. The lipid density in prepared vesicles is estimated using a method involving characterization of intrinsic viscosities [18]. The intrinsic viscosity, $[\eta]$, of the vesicles is defined as :

$$[\eta] = \left(\frac{\eta_r - 1}{C}\right)_{C \to 0} \tag{2.1}$$

where, η_r is the relative viscosity given by $\frac{\eta_s}{\eta_o}$, with η_s denoting the viscosity of vesicle dispersion at very low concentration, and η_o is the viscosity of water. C is the concentration of lipid in the vesicle dispersion.

Esterquat	**Intrinsic viscosity (m^3/kg)$\times 10^{-3}$**	
	Large vesicles	Small vesicles
DEEDMAC	68.9	19.4
WE18	61.2	17.3
WE15	53.2	14.1

Table 2.1.: Measured instrinsic viscosities of the vesicle dispersions

We assume the validity of the Einstein equation for hard spheres [19], and can thus only obtain rough comparative estimates of vesicle lipid density values. The Einstein equation gives a linear relationship between viscosities and vesicle volume fractions in dilute dispersions. As a result an inverse relationship between vesicle lipid densities and intrinsic viscosities is obtained. From the values listed on Table 2.1, it can be observed that the intrinsic viscosity of all large vesicles are higher than that of the corresponding small (microfluidized) vesicles. Using the inverse relationship given by Einstein equation, it is therefore estimated that the lipid density of the small (microfluidized) vesicles is significantly higher (3-4 times) than that of the corresponding large vesicles.

2.2 Porous and non-porous solid substrates

Cellulose fiber based substrates have been used as deposition substrates in this thesis. For the batch deposition experiments, single cellulose fibers and porous cotton yarns have been used. For the droplet wetting and evaporation experiments on porous substrates, different grades of cellulose fiber filter papers were used. The properties of all the used substrates are described below.

2.2.1 Single cellulose fibers

Natural and regenerated single cellulose fibers, namely cotton and viscose, were obtained from available commercial product called Ebelin, from drogerie markt (dm), Germany, and were pre-washed to remove any textile treatment. The fibers as observed by scanning electron microscopy on a TM 3000 (Olympus), and their surface topography as characterized by optical confocal microscopy on a Nanofocus are shown in Fig 2. It can be identified that cotton fibers are rough and have irregularly shaped cross-sections with several twists and turns along its length, whereas viscose fibers are smooth with consistent but non-circular cross-sections due to the presence of some depressions on their external surface.

2.2.2 Porous cotton yarns

The cotton yarns (standard cotton 10A) were procured from WFK Testmaterials GmbH, Germany. This particular type of cotton yarn have been chosen for our study as they are commonly used in textile manufacture, and they have also been characterized in previous studies [20].

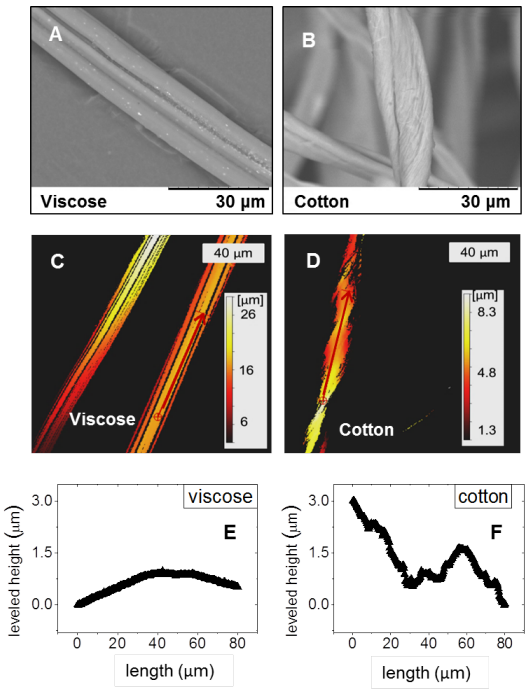

Figure 2.6.: SEM images of viscose (A) and cotton (B) fibers, surface topography of viscose (C) and cotton fibers (D), and surface roughness profiles along the lines marked with arrow in (C) and (D) (Image reproduced with permission from Kumar et. al. [13])

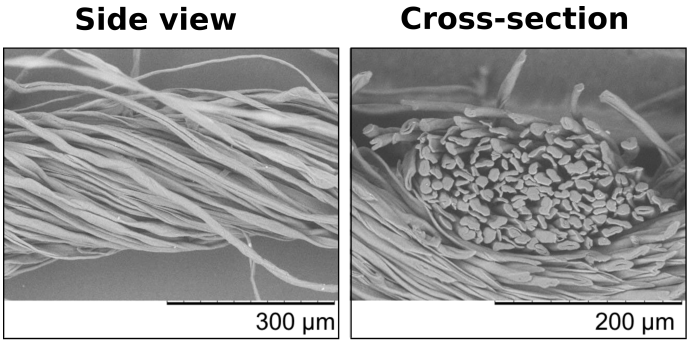

Figure 2.7.: SEM images of the cotton yarns used in this thesis (Image reproduced with permission from Kumar et. al. [22])

The distribution of pore sizes in cotton yarns is heterogeneous with the separation between neighboring fibers ranging from low (1-2 μm) to high (10-20 μm) as could be identified from Fig. 2.7. The distribution of pore sizes in these yarns has also been investigated in an earlier work [21]. The porosity of these yarns, as estimated via different techniques in an earlier work, is typically in the range 30-40% [20].

2.2.3 Porous cellulose fiber filter papers

Two different kinds of commercial cellulose fiber filter papers, namely, Whatman 903 and Sartorius 388, were used as porous substrate for the most of the droplet wetting and evaporation experiments. The filter papers were observed using a Keyence optical laser scanning microscope. The images are shown in Fig. 2.8. The thicknesses of these filter papers as specified by the

manufacturer are 500 μm and 210 μm, respectively. The cross-sectional images of these filter papers shown in Fig. 2.8 also reveal the same substrate thicknesses.

Apart from these two main filter papers, other grades of the Sartorius filter paper, namely 389, 390 and 392 were used as well. These filter papers differ in terms of their thickness and grammage (substrate mass per unit lateral area) which leads to differences in their porosities and pore sizes. The properties of the different grades of Sartorius filter papers as specified by the manufacturer are enlisted on Table 2.2. The "particle retention" value on Table 2.2 is the size of the smallest particle that cannot pass through the filter paper pores. The top views of these filter papers shown on Fig.2.9 clearly reveal their different pore sizes.

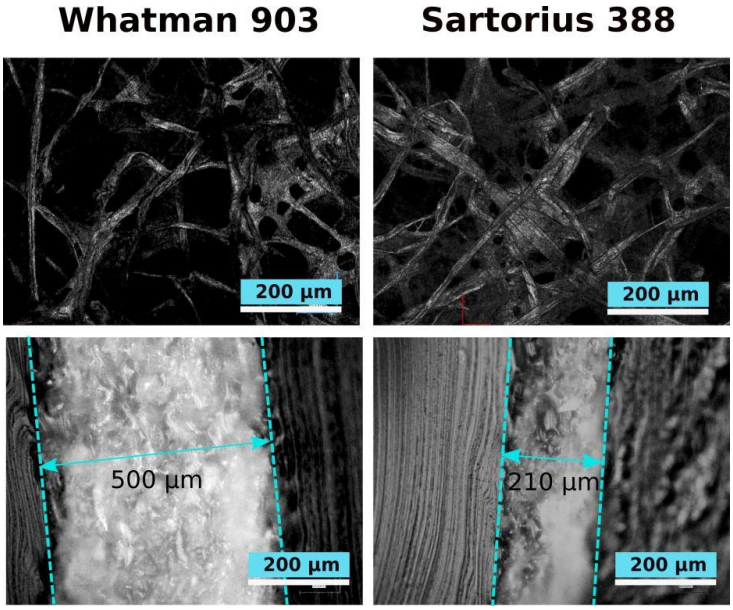

Figure 2.8.: Top and cross-sectional views of the cellulose fiber filter papers, Whatman 903 and Sartorius 388 (Image reproduced with permission from Kumar et. al. [17])

Paper Grade	Paper properties		
	Thickness (μm)	Grammage (g/m^2)	Particle retention (μm)
388	210	84	12-15
389	190	84	8-12
392	170	84	5-8
390	160	84	3-5

Table 2.2.: Properties of the different grades of Sartorius filter papers as specified by the manufacturer

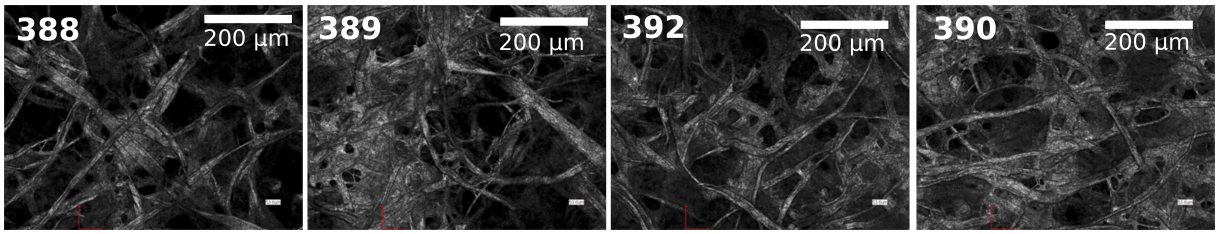

Figure 2.9.: Top views of the different grades of Sartorius filter papers. The substrates are arranged in the order of decreasing pore sizes from left to right.

3 Zeta potential characterization of fiber plugs and porous substrates

This chapter outlines the theory underlying the experimental technique used for characterizing the zeta potential of macroscopic solid surfaces, namely, the single cellulose fibers and porous cotton yarns, used as deposition substrates in this thesis. The limitations of the conventionally used theory are pointed out and a new theoretical approach is described.

This chapter is based on the article, *Effect of geometry on electrokinetic characterization of solid surfaces*, by Kumar et al. (2017) published in Langmuir.

3.1 Background of streaming potentials and streaming current measurements

Electrokinetic characterization via streaming current and streaming potential measurements is one of the most widely used techniques for determining the zeta potential of macroscopic solid surfaces. It is thus an indispensable research tool in several application domains such as paper [23–25], textiles [13, 26–29], membranes [30–32] and biomaterials [33–35].

The measurement technique involves flowing an electrolyte solution of known conductivity through capillaries, channels or porous structures formed out of the solid substrate [36] under an applied pressure difference (ΔP), as shown in Fig. 3.1(A). When electrolytes flow along charged solid surfaces, the flow inside electrical double layers (EDLs) results in convective transport of counter-ions in the flow direction, which constitutes the streaming current (I_{str}). The total I_{str} along the pressure gradient direction through a sample cross-section $\mathbf{A_c}$ is given by the basic electrokinetic equation [37], as given below :

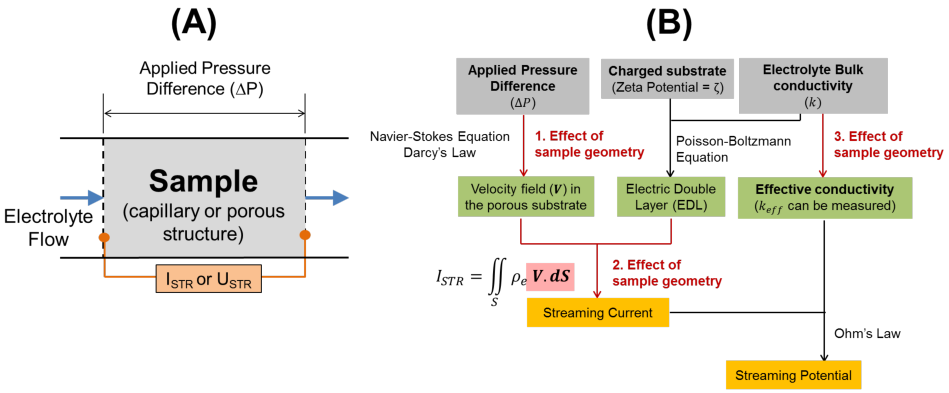

Figure 3.1.: (A) Experimental scheme used for streaming current/potential characterization of samples, and (B) Flow diagram of processes leading to streaming current/potential generation. The steps which could be affected by sample geometry are marked with red and labeled as 1-3. The existing theories/equations that can be used to describe these steps are also mentioned alongside.

$$I_{str} = \iint_{\mathbf{A_c}} \rho_e \mathbf{V} \cdot \mathbf{dA_c} \tag{3.1}$$

where, ρ_e is the electric charge density (non-zero only inside EDLs)[38], $\mathbf{V}$ is the macroscopic velocity field, and $\mathbf{dA_c}$ is a directed surface element of the cross-section $\mathbf{A_c}$ along the pressure gradient direction.

Due to the unidirectional transport of counter-ions with liquid flow, an electric potential difference, known as the streaming potential (U_{str}) develops across the sample. The developed U_{str} induces a conduction current flow through the electrolyte opposite to the direction of liquid flow. The streaming current (I_{str}) is balanced by the conduction current (I_c), and the value of the developed U_{str} is obtained by applying Ohm′s Law for conduction current flow.

The classical relationship which is commonly used to convert measured I_{str} and U_{str} values into substrate zeta potentials is known as the Helmholtz-Smoluchowski (H-S) equation. It has been derived analytically for uniform cross-sectional capillaries by applying Eq. 3.1 and Ohm's law [39]. The equation is, however, valid only under the conditions that : (i) the EDL thickness is sufficiently small compared with the capillary radius [39–41], (ii) the electric charge density inside EDLs is unperturbed by the liquid flow [42], (iii) the electroviscous effect, i.e. the effect of EDL on liquid viscosity, is negligible [43, 44], and (iv) surface conductivity effects are negligible . The same above conditions also need to be satisfied for the analytical approach presented in this work to be applicable.

Given that the above conditions are satisfied, the I_{str} and U_{str} generated in straight capillary geometries could be described by the H-S equation :

$$I_{str} = \frac{\epsilon_o \epsilon_{rs}}{\mu} \frac{A_c}{L} \Delta P \zeta \tag{3.2}$$

$$U_{str} = \frac{\epsilon_o \epsilon_{rs}}{\mu \kappa} \Delta P \zeta \tag{3.3}$$

where, ϵ_o and ϵ_{rs} are the vacuum permittivity and dielectric constant of the electrolyte, respectively. A_c and L are the capillary cross-sectional area and length, respectively. κ and μ are the bulk electrical conductivity and dynamic viscosity of the electrolyte solution, respectively. ΔP is the pressure difference applied across the capillary, and ζ is the solid surface zeta potential.

3.2 Streaming potential and streaming current measurements on porous substrates

Although the H-S equation has been obtained analytically only for uniform cross-sectional capillaries, the characterization of most real-life substrates involves geometrically complex samples such as membranes, textiles, and minerals, where electrolytes are flown through non-uniform and irregular channels. An important question therefore has been whether, in such

cases, the H-S equation is still applicable. Overbeek [45] suggested that if pressure-driven liquid flow inside porous samples is laminar, and if pore sizes remain larger than the EDL thickness, a simplistic extension of the H-S equation could still be used. In this approach, non-idealities induced by irregular sample geometries are ignored, and the porous sample is treated as a bundle of parallel straight capillaries. The equations which are hence obtained are given below :

$$I_{\text{str}} = \frac{\epsilon_{\text{o}}\epsilon_{\text{rs}}}{\mu}\frac{A_{\text{T}}\phi}{L}\Delta P\zeta, \tag{3.4}$$

$$U_{\text{str}} = \frac{\epsilon_{\text{o}}\epsilon_{\text{rs}}}{\mu\kappa}\Delta P\zeta, \tag{3.5}$$

where, ϕ is the sample porosity, and A_{T} is the total cross-sectional area of the sample.

In experimental works investigating the applicability of the parallel capillary model [36, 46–48], it was identified that although the linear variation of U_{str} and I_{str} with ΔP is observed with most samples, the experimentally measured U_{str} and I_{str} values could deviate significantly from the values given by Eq. 3.4 and 3.5. Furthermore, this approach fails to explain the capillary shape dependence of I_{str} and U_{str} generation in the case of non-uniform cross-sectional capillaries [36, 49]. In the general case of porous fiber plugs, it doesn't capture the variations of I_{str} and U_{str} with fiber orientation and packing density [50, 51].

A common approach used for incorporating sample geometry effects on I_{str} generation, referred to as the "Helmholtz-Smoluchowski approximation", involves experimentally estimating the so-called "cell constant" (the ratio L/A_{c} in Eq. 3.2) via sample electrical resistance measurements [36, 52]. Although, the parameters L and A_{c} are well defined for a uniform capillary, they are complex parameters for non-uniform geometries, and hence apparent values are used, which are evaluated indirectly from sample electrical resistance values, as given below:

$$R = \frac{1}{\kappa}\frac{L_{\text{app}}}{A_{\text{app}}}, \tag{3.6}$$

where, R is the experimentally measured sample electrical resistance, $L_{\text{app}}/A_{\text{app}}$ is the apparent value of the cell constant for the non-uniformly shaped sample which is subsequently substituted in Eq. 3.2 to obtain the generated I_{str}. Although widely used, the idea underlying the H-S approximation that the cell constant as determined via sample electrical resistance measurements could be used to obtain the generated I_{str} is inaccurate as it does not account for the sample geometry dependence of U_{str} generation. It is thus not an all-inclusive approach.

In earlier attempts to resolve the above discrepancy, the use of empirical functions of plug packing densities, referred to as shape correction factors has been proposed [53–55]. In other works, the so-called "formation factors" [56, 57] have been used to account for sample geometry effects. Another recent practice has been to lump the non-idealities arising from geometry effects into effective quantities such as effective porosity (ϕ_{eff}) and effective zeta potential (ζ_{eff}) [58].

In spite of a lack of clear insights into the factors on which such effective quantities depend, this approach has been widely used in characterization of membranes [59, 60].

An analytical scheme is therefore required that incorporates all the possible geometry effects on I_{str} and U_{str} generation, and developing the same forms the main objective of this chapter. In principle, once the velocity field has been obtained, it could be coupled with Eq. 3.1 to obtain the generated I_{str} followed by an application of Ohm′s law to obtain the generated U_{str}. However, to obtain usable relationships using these theories could be very challenging even for moderately non-ideal sample geometries.

This chapter is further organized into 4 sections. In the next section, a general theory is presented wherein a fundamental microscale relationship to describe I_{str} generation in different cross-sections of a sample is established. Thereafter, this fundamental relationship is applied to an arbitrarily shaped porous substrate, where, using a force balance on thin liquid layers in the direction of pressure difference, the generated I_{str} is related to the pressure gradient inside the sample. Furthermore, assuming that the generated U_{str} varies only along the macroscopic pressure gradient direction, a general expression is obtained to relate the generated U_{str} to the total pressure difference applied across the sample. This analytical approach provides a framework that accounts for the sample geometry dependence of I_{str} and U_{str} generation.

The general expressions for I_{str} and U_{str} generation are applied to obtain analytical solutions for a set of 3 non-uniform cross-sectional capillaries and for a square array of cylindrical fibers (model porous media). The pressure gradients inside sample geometries are obtained by using simplifying approximations to describe macroscopic liquid flow. Based on the results obtained for model porous media, some insights are obtained into the practically important case of zeta potential determination of porous fiber plugs. Strategies are devised for optimizing the measurement conditions for improving the accuracy of zeta potential measurements. Finally, the findings are summarized.

3.3 Fundamental theory of geometry effects on generation of I_{str} and U_{str}

In order to understand the reasons underlying the dependence of generated I_{str} and U_{str} on sample geometry, it is helpful to consider a flow diagram of all steps leading to I_{str} and U_{str} generation, as shown in Fig. 3.1(B). Those steps which might be affected by sample geometry are labelled as Steps 1-3 on the flowchart, and are discussed below.

Firstly, the geometry of porous samples has a direct influence on the characteristics of pressure-driven liquid flow (Step 1 on Fig. 3.1(B)). Although the velocity field ($\mathbf{V}$) could be in principle obtained by solving the Navier-Stokes equation using a no slip condition at solid-liquid interfaces, obtaining analytical solutions is very difficult for non-trivial geometries. Simplifications such as the creeping flow and lubrication approximations [61, 62] could be utilized under certain special conditions.

Apart from the direct effect of sample geometry on the velocity field, the orientation of solid surfaces with respect to the pressure gradient direction also influences I_{str} generation as determined by the dot product term $\mathbf{V} \cdot \mathbf{dA_c}$ in Eq. 3.1 (Step 2 on Fig. 3.1(B)).

The geometry of porous substrates affects bulk conduction current flow through confined liquids, and hence could influence U_{str} generation (Step 3 on Fig. 3.1(B)). We assume that surface conductivity effects are negligible. In such cases, the non-ideal porous substrate geometry effects only the macroscopic current flow characteristics, and an effective electrical conductivity term (κ_{eff}) is usually defined to account for it [63]. However, whether such an effective electrical conductivity (κ_{eff}) should be used while describing U_{str} generation is discussed in later in the chapter. We demonstrate that since our theory employs a pore-scale relationship to describe U_{str} generation, it is the bulk electrical conductivity which should be used.

3.3.1 Fundamental microscale relationship for I_{str} generation

Given that a pressure difference (ΔP) is applied across a porous sample in the z-direction, let $L_c(z)$ be the intersection line of the solid-liquid interface with a sample cross-section $\mathbf{A_c}$ located at a level of z along the pressure-gradient direction. A length element dL_c of the intersection line $L_c(z)$ where the local surface tangent along the local liquid flow direction ($\hat{\boldsymbol{\tau}}$) is inclined at an angle θ with respect to the z-direction, is shown in Fig. 3.2(A). The total streaming current ($I_{str}(z)$) through the cross-section $\mathbf{A_c}$ could be evaluated via a summation of infinitesimal streaming currents (dI_{str}) generated due to flow inside EDLs adjoining the length elements dL_c constituting $L_c(z)$. This approach is valid if EDL thickness is much smaller than the pore radius.

The streaming current $I_{str}(z)$ is obtained via a path integral of the expression for dI_{str} along the intersection line $L_c(z)$. dI_{str} can be expressed as a function of the solid surface zeta potential (ζ), local hydrodynamic wall shear stress ($\boldsymbol{\tau}_{wall}$), and local orientation of solid surface with respect to pressure-gradient direction (θ) following the procedure outlined below.

In the case of thin EDLs, liquid flow velocity inside the EDL adjoining dL_c can be expressed as a linear function of the local wall shear stress ($\boldsymbol{\tau}_{wall}$) :

$$V_\tau(y)\,\hat{\boldsymbol{\tau}} = \Big(\frac{\boldsymbol{\tau}_{wall}}{\mu}\Big)y \tag{3.7}$$

where, $\boldsymbol{\tau}_{wall}$ is the local wall shear stress vector. V_τ is the liquid flow velocity tangential to the solid surface. $\hat{\boldsymbol{\tau}}$ is the unit vector along local liquid flow direction. y is the distance from the solid surface along the local surface normal ($\hat{\boldsymbol{n}}$) as shown in Fig. 3.2(A).

Making use of Eq. 3.7 to describe liquid flow velocities inside EDLs, the streaming current dI_{str} resulting from convective transport of counter-ions in the EDL adjoining the solid-liquid interface length element dL_c is determined :

$$dI_{str} = \int_0^{\delta_{EDL}} \rho_e(y) V_\tau(y) \hat{\boldsymbol{\tau}} \cdot \hat{\boldsymbol{z}}\; dL_c dy = \frac{\boldsymbol{\tau}_{wall} \cdot \hat{\boldsymbol{z}}}{\mu} dL_c \int_0^{\delta_{EDL}} y \rho_e(y) dy \tag{3.8}$$

where, δ_{EDL} is the thickness of the EDL, and $\rho_e(y)$ is the electric charge density inside the EDL.

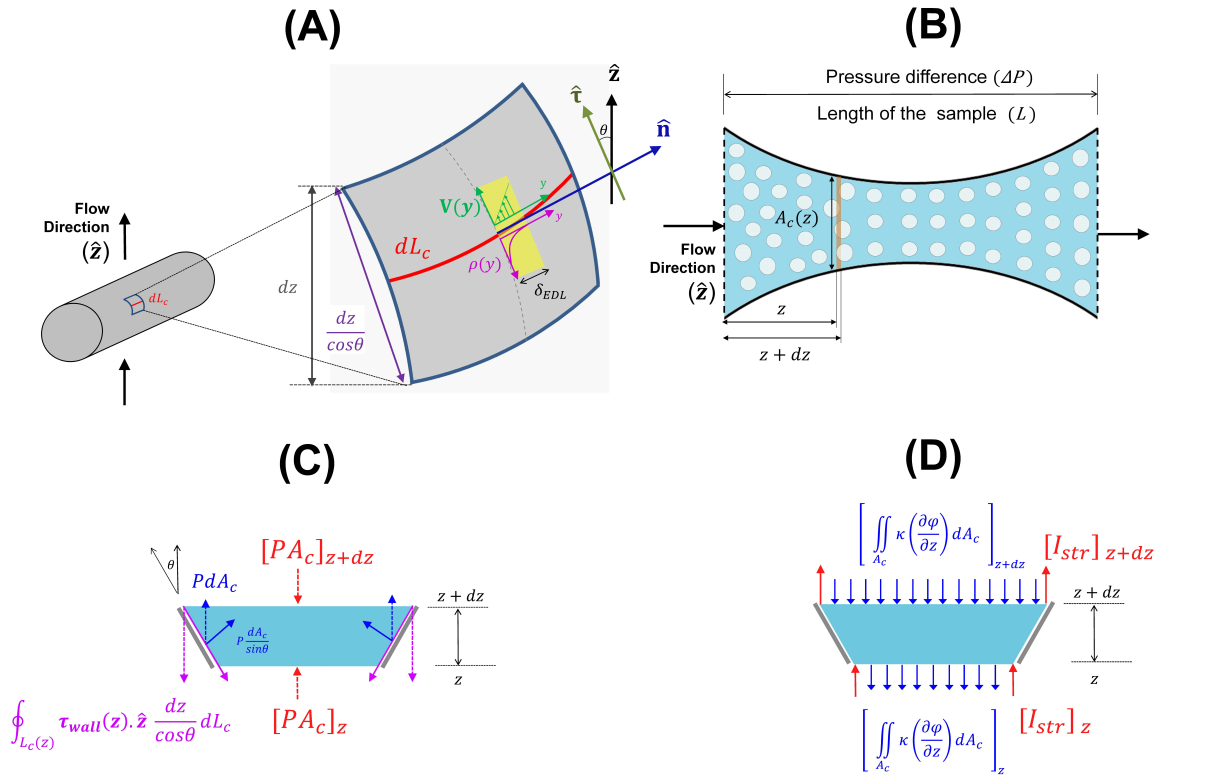

Figure 3.2.: (A) Velocity profile (shown in green) and electric charge density profile (shown in pink) inside EDLs near charged solid surfaces. (B) Schematic representation of an arbitrarily shaped porous sample. (C) Schematic representation of the force components acting on an infinitesimally thin liquid layer of thickness dz located at height z along the pressure gradient direction. (D) Schematic representation of the currents flowing in and out of the thin liquid layer due to streaming current and bulk conduction current flow.

The integral $\int_0^{\delta_{\mathrm{EDL}}} y\rho_{\mathrm{e}}(y)dy$ in Eq. 3.8 depends only on EDL properties, and could be determined independently using the Poisson-Boltzmann equation to describe $\rho_{\mathrm{e}}(y)$, as shown by Adamczyk et. al. [42] :

$$\int_0^{\delta_{\mathrm{EDL}}} y\rho_{\mathrm{e}}(y)dy = \epsilon_{\mathrm{o}}\epsilon_{\mathrm{rs}}\zeta \tag{3.9}$$

Upon substituting the value of the integral from Eq. 3.9 in Eq. 3.8, a simplified expression is obtained for dI_{str} :

$$dI_{\mathrm{str}} = \frac{\epsilon_{\mathrm{o}}\epsilon_{\mathrm{rs}}\zeta}{\mu}\,\boldsymbol{\tau}_{\mathrm{wall}}\cdot\hat{\boldsymbol{z}}\,dL_{\mathrm{c}} \tag{3.10}$$

The total streaming current $I_{\mathrm{str}}(z)$ through the cross-section located at the level of z could be obtained via an integral of Eq. 3.10 along the solid-liquid interface line $L_{\mathrm{c}}(z)$:

$$I_{str}(z) = \oint_{L_c(z)} dI_{str} = \frac{\epsilon_o \epsilon_{rs} \zeta}{\mu} \oint_{L_c(z)} \boldsymbol{\tau}_{wall} \cdot \hat{\mathbf{z}}\, dL_c \tag{3.11}$$

It should be kept in mind that the above relationship for I_{str} generation is valid under the same prerequisite conditions which are required for the H-S equation. Firstly, Eq. 3.7 is valid only if the EDLs are thin, i.e. δ_{EDL} is small in comparison to the pore radius. Secondly, it is assumed that the electric charge density inside EDLs should be unperturbed by the liquid flow which is reasonable under laminar flow conditions [42]. Furthermore, the electroviscous effect, i.e. the effect of EDLs on liquid viscosity, should be negligible. In an earlier work, it has been demonstrated that the electroviscous effect is insignificant when the factor a/δ_{EDL}, where a is the pore radius, does not lie between 0.3 and 30 [64, 65]. Therefore, if pore radius is much greater than δ_{EDL}, the electroviscous effect could be safely neglected. When using this theory in applications, it should be therefore ensured that this condition is met. This condition would be satisfied in measurements involving macroscopic substrates where the pore radius is typically of the order of micrometers, while the used electrolyte solution has an EDL thickness of the order of nanometers.

3.3.2 General expressions for an arbitrary porous sample

In this section, we consider a porous sample of length L with arbitrary internal geometry, and with the external form of an object with non-uniform cross-sectional area, as shown schematically in Fig. 3.2(B). Thereafter, general expressions to describe I_{str} and U_{str} generation in such geometries are obtained.

3.3.2.1 Streaming current

It is evident from Eq. 3.11 that the streaming current generated in a certain sample cross-section is dependent on the shear stresses and the surface orientations at the solid-liquid interface. Thus, for an irregularly shaped sample, I_{str} could vary along the sample length from one cross-section to another.

In order to relate the streaming current I_{str} given by Eq. 3.11 to the applied pressure difference ΔP, we consider a balance of forces along the pressure gradient direction on thin liquid layers of thickness dz located between two cross-sectional planes at the levels of z and $z+dz$, respectively (Fig. 3.2(B)). The shear and normal reaction forces exerted by the surrounding walls, and the pressure forces exerted by the liquid above and below the thin layer are accounted for. The total shear force exerted on the thin liquid layer opposite to the pressure-gradient direction is obtained via an integral of the z-component of shear forces acting on the solid-liquid interface.

For understanding the force balance, the thin liquid layer is visualized in Fig. 3.2(C). The balance of forces acting on the thin layer in the z-direction is given below :

$$\underbrace{\left[PA_c\right]_z - \left[PA_c\right]_{z+dz}}_{\text{Net upwards pressure force}} + \underbrace{PdA_c}_{\text{Upwards contact force}} = \underbrace{\oint_{L_c(z)} \boldsymbol{\tau}_{wall} \cdot \hat{\mathbf{z}} \frac{dz}{\cos\theta}\, dL_c}_{\text{Downwards shear force}} \tag{3.12}$$

where, P is the pressure, A_c is the area of the liquid in the cross-section, and dA_c is the differential change in area along the height dz. The line integral on the right gives the total shear force acting on the liquid layer opposite to the pressure gradient direction with $\frac{dz}{\cos\theta}\, dL_c$ being the area elemenent along which the viscous shear force is applied.

It is, however, to be noted such a force balance is valid only under such flow conditions wherein the creeping flow approximation is applicable. The above force balance could be consequently simplified to the following form :

$$A_c(z)\frac{-dP}{dz} = \oint_{L_c(z)} \frac{1}{\cos\theta}\, \boldsymbol{\tau}_{\text{wall}} \cdot \hat{\mathbf{z}}\, dL_c \tag{3.13}$$

Thereafter, Eq. 3.11 is divided by Eq. 3.13 :

$$I_{\text{str}}(z) = \frac{\epsilon_o \epsilon_{rs} \zeta}{\mu} A_c \frac{-dP}{dz} \frac{\oint_{L_c(z)} \boldsymbol{\tau}_{\text{wall}} \cdot \hat{\mathbf{z}}\, dL_c}{\oint_{L_c(z)} \frac{1}{\cos\theta}\, \boldsymbol{\tau}_{\text{wall}} \cdot \hat{\mathbf{z}}\, dL_c} \tag{3.14}$$

Eq. 3.14 is the general expression that can be used to describe I_{str} generation in different cross-sections of a sample. An important property of Eq. 3.14 is that if all solid surfaces in a particular sample cross-section are identically oriented and make the same angle with the pressure gradient direction, the $\frac{1}{\cos\theta}$ term could be taken outside the path integral in the denominator. Eq. 3.14 could then be further simplified :

$$I_{\text{str}}(z) = \frac{\epsilon_o \epsilon_{rs} \zeta}{\mu} A_c \frac{-dP}{dz} \cos\theta \tag{3.15}$$

3.3.2.2 Streaming potential

In order to estimate the streaming potential generated across the sample in the pressure gradient direction, we consider a balance of currents flowing into and out of a thin liquid layer between z and $z + dz$, as shown in Fig. 3.2(D). Both the streaming current, and the bulk conduction current described using Ohm's law are accounted for :

$$\underbrace{\Big[I_{str}\Big]_z + \Big[\iint_{A_c} \kappa\Big(\frac{\partial \psi}{\partial z}\Big) dA_c\Big]_{z+dz}}_{\text{Total inwards current flow}} = \underbrace{\Big[I_{str}\Big]_{z+dz} + \Big[\iint_{A_c} \kappa\Big(\frac{\partial \psi}{\partial z}\Big) dA_c\Big]_z}_{\text{Total outwards current flow}} \tag{3.16}$$

where, ψ is the bulk electric potential developed as a response to streaming current flow. It is important to note that the electric potential ψ is not necessarily uniform in a certain cross-section.

Therefore, the total bulk conduction current flowing through a certain cross-section is obtained via a surface integral.

Although the bulk electric potential ψ might also vary perpendicular to the z-direction inside the cross-sections, the main objective of our analysis is obtaining the measurable electric potential difference developed across the sample length along the pressure gradient (z) direction. For this purpose, we assume that the generated electric potential varies only along the pressure gradient direction, and that it is uniform in each cross-section, i.e. $\psi\big|_z = U_{str}(z)$.

Upon simplifying Eq. 3.16, assuming uniform electric potential in each cross-section, the following relationship is obtained :

$$\frac{dI_{\text{str}}(z)}{dz} = \kappa \frac{d}{dz}\left(A_c \frac{dU_{str}(z)}{dz}\right) \tag{3.17}$$

Upon integrating Eq. 3.17 with respect to z the following relation is obtained :

$$I_{\text{str}}(z) = \kappa A_c \frac{dU_{str}(z)}{dz} \tag{3.18}$$

The integration constant is equal to zero, because at the extreme ends of the sample ($z = 0$ & $z = L$) the values of the streaming current ($I_{\text{str}}(z)$), and the conduction current ($\kappa A_c(z)\frac{dU_{str}}{dz}$) are exactly equal since no net current enters or leaves the system.

The electrical conductivity term used in Eq. 3.18 is the bulk conductivity (κ) and not the effective electrical conductivity of the porous structure (κ_{eff}). Eq. 3.18 is a micro-scale relationship, whereas κ_{eff} is a macroscopically defined effective parameter, therefore κ_{eff} is not required in Eq. 3.18. This means that the Step 3 as depicted in Fig. 3.1(B) does not have an effect on U_{str} generation in our case.

The generated U_{str} can be obtained by integrating Eq. 3.18 along the sample length after substituting the value of $I_{str}(z)$ from Eq. 3.14 :

$$U_{\text{str}}(z) = \frac{\epsilon_{\text{o}}\epsilon_{\text{rs}}\zeta}{\mu\kappa}\int_0^z \frac{-dP}{dz}\frac{\oint_{L_{\text{c}}(z)} \boldsymbol{\tau}_{\text{wall}}\cdot\hat{\mathbf{z}}\, dL_{\text{c}}}{\oint_{L_{\text{c}}(z)} \frac{1}{\cos\theta}\, \boldsymbol{\tau}_{\text{wall}}\cdot\hat{\mathbf{z}}\, dL_{\text{c}}} dz \tag{3.19}$$

The above general expression could be further simplified in the case of porous samples in which all solid surfaces in a particular cross-section are oriented at the same angle (θ) with respect to the z-direction :

$$U_{\text{str}}(z) = \frac{\epsilon_{\text{o}}\epsilon_{\text{rs}}\zeta}{\mu\kappa}\int_0^z \frac{-dP}{dz}\cos\theta\; dz \tag{3.20}$$

It is important to note that in the development of the above theory, surface conductivity effects have been neglected, and it is assumed that the back current flow takes place entirely through the bulk electrolyte. The relative significance of surface conductivity effects is usually quantified in terms of the dimensionless Dukhin number (Du) which relates the surface and bulk conductivities [38, 39]. The contribution of surface conductivity to current flow is negligible when $Du \ll 1$ [66]. When surface conductivity effects are not negligible, their role in back current flow should be duly accounted for [67–69]. The surface conductivity includes contributions from both the diffuse double layer as well as the stagnant layer [38, 39]. The diffuse double layer's contribution to surface conductivity is negligible when the EDL thickness is sufficiently low, and the magnitude of ζ is low [38]. The contribution of the stagnant layer to surface conductivity could, however, not be correlated to other physical parameters in exisiting theories [39]. Therefore, when applying the proposed theory in practice, it should be determined beforehand if the surface conductivity effects are negligible at the conditions employed during the measurements.

3.4 Application to model sample geometries

3.4.1 Capillaries with non-uniform cross-section

In this section, the simplified general expressions for I_{str} and U_{str} generation in porous samples, as given by Eqs. 3.15 and 3.20, respectively, are applied to a set of 3 axi-symmetric capillaries with non-uniform cross-sectional area, as shown in Fig. 3.3(A)-(C). These capillary geometries are chosen as their sizes could be described using the same three physical dimensions, namely, R_o (diameter of the wider end), R_i (diameter of the narrower end), and L (length of the capillary). Additionally, the shapes of these capillaries could be defined in terms of only two non-dimensional size ratios, $\gamma_1 = R_i/R_o$ and $\gamma_2 = R_o/L$.

It is assumed that for the considered capillaries, the ratio $\frac{R_O - R_i}{L}$ is much less than 1, in which case the lubrication approximation can be used to describe pressure-driven macroscopic liquid flow inside the capillaries [70]. This condition is frequently fulfilled in substrates such as membranes and textiles [71]. The results obtained for the different capillary shapes are compared to each other to demonstrate the capillary shape dependence of I_{str} and U_{str} generation.

3.4.1.1 Capillary A

We consider the capillary having a conical shape as shown in Fig. 3.3(A) with a zeta potential ζ and a pressure difference ΔP applied across it. The Eqs. 3.15 and 3.20 are used to obtain expressions for the variation of streaming currents/potentials along the capillary length.

Under lubrication approximation, the velocity profile along the pressure-gradient direction in a capillary cross-section with radius R_z located at level of z along the capillary length is given by

$$\frac{1}{r}\frac{\partial}{\partial r}\left(r\frac{\partial V_z}{\partial r}\right) = \frac{1}{\mu}\frac{dP}{dz}, \quad V_z(r) = -\frac{1}{4\mu}\frac{dP}{dz}({R_z}^2 - r^2) \tag{3.21}$$

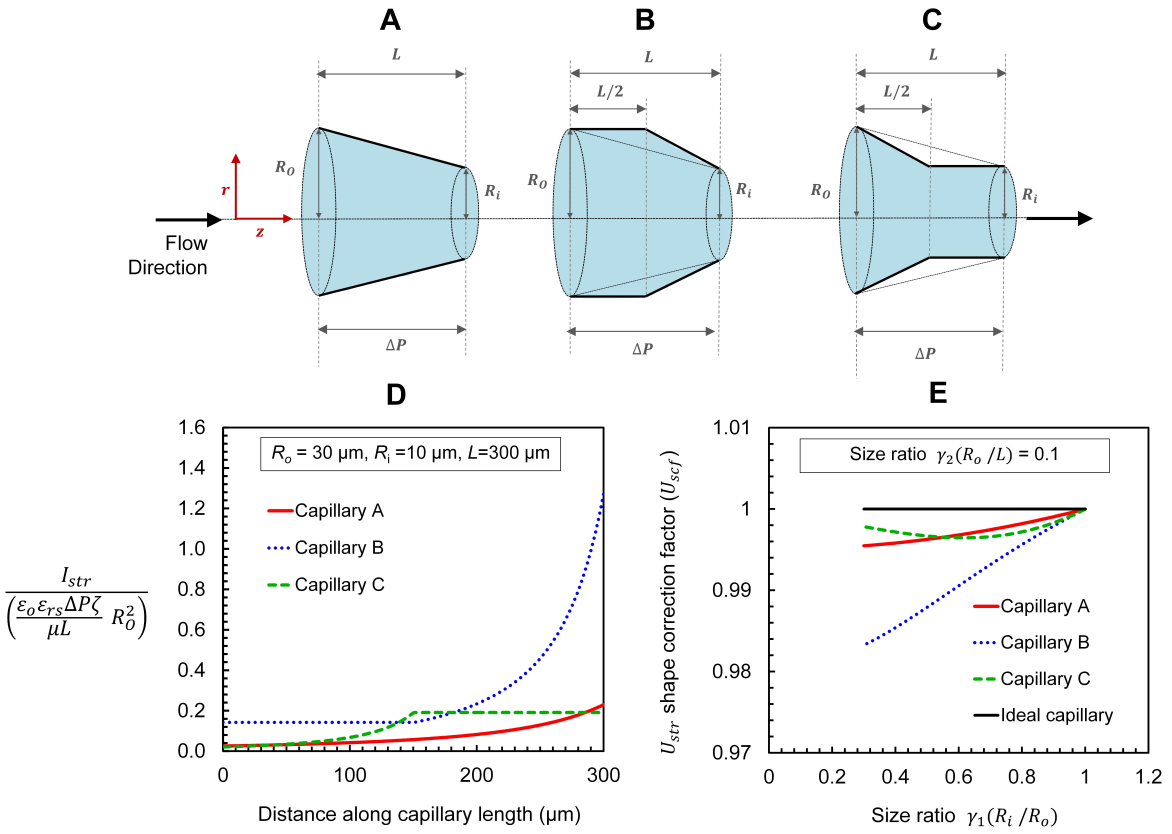

Figure 3.3.: (A)-(C) Geometry of non-uniform cross-sectional capillaries for which analytical solutions are obtained, (D) Variation of the generated streaming current along the length of the capillaries, and (E) Variation of U_{str} shape correction factor (U_{scf}) with the size ratio $\gamma_1 = R_i/R_o$ at a fixed size ratio $\gamma_2 = R_o/L = 0.1$ for the capillaries. For an ideal capillary with uniform cross-sectional area, U_{scf} is equal to 1.

The volumetric flow rate (Q) through a capillary cross-section could be determined as shown below :

$$Q = \int_0^{R_z} V_z(r)\, 2\pi r\, dr = -\frac{\pi {R_z}^4}{8\mu}\frac{dP}{dz} \tag{3.22}$$

Upon expressing the cross-sectional radius R_z as a function of the distance along the capillary length z as $R_o - (\frac{R_o - R_i}{L})z$, and integrating Eq. 3.22 along the capillary length ($0 \leq z \leq L$), the volumetric flow rate Q is obtained in terms of the applied pressure difference ΔP. The value of Q is thereafter substituted in Eq. 3.22 to obtain the pressure gradient as a function of z

$$-\frac{dP}{dz} = \frac{\Delta P}{L}\frac{1}{f_A(R_i/R_o)}\frac{{R_o}^4}{{R_z}^4}, \tag{3.23}$$

where, $f_A(R_i/R_o) = \frac{(1+\gamma_1+{\gamma_1}^2)}{3{\gamma_1}^4}$ with $\gamma_1 = \frac{R_i}{R_o}$.

Next, the pressure gradient from Eq. 3.23 is substituted in Eq. 3.15 to obtain I_{str} through different cross-sections of the capillary :

$$I_{str}(z) = \frac{\epsilon_o \epsilon_{rs} \Delta P \zeta}{\mu L} \frac{1}{f_A(R_i/R_o)} \frac{{R_o}^4}{{R_z}^2} \cos\theta_A \tag{3.24}$$

where, $\cos\theta_A$ is a constant, and given by $\frac{L}{\sqrt{(R_o - R_i)^2 + L^2}}$.

U_{str} developed in the capillary is obtained by substituting the expressions for the pressure gradient (Eq. 3.23) and $\cos\theta_A$ into Eq. 3.20 :

$$U_{str}(z) = \frac{\epsilon_o \epsilon_{rs} \Delta P \zeta}{\mu \kappa} \frac{1}{f_A(R_i/R_o)} \frac{{R_o}^4}{L} \int_0^z \frac{\cos\theta_A}{{R_z}^4} \, dz \tag{3.25}$$

The total U_{str} developed across the capillary is obtained by using $z = L$ as the upper integration limit in Eq. 3.25, and upon simplification, it could be expressed in terms of non-dimensional size ratios $\gamma_1 = R_i/R_o$ and $\gamma_2 = R_o/L$:

$$U_{str} = \frac{\epsilon_o \epsilon_{rs} \Delta P \zeta}{\mu \kappa} \cos\theta_A = \frac{\epsilon_o \epsilon_{rs} \Delta P \zeta}{\mu \kappa} \frac{1}{\sqrt{1 + {\gamma_2}^2 (1 - {\gamma_1}^2)}} \tag{3.26}$$

The analytical methodology used for capillary A could also be extended to the capillaries B and C to firstly obtain expressions for $\frac{-dP}{dz}$, and thereafter for $I_{str}(z)$ and $U_{str}(z)$.

3.4.1.2 Capillary B

The pressure gradient along the length of Capillary B is given by :

$$-\frac{dP}{dz} = \frac{\Delta P}{L} \frac{1}{f_B(R_i/R_o)} \frac{{R_o}^4}{{R_z}^4} \tag{3.27}$$

where, $f_B(R_i/R_o) = \frac{1 + \gamma_1 + {\gamma_1}^2 + 3{\gamma_1}^3}{6{\gamma_1}^3}$ with $\gamma_1 = R_i/R_o$, and $R_z = R_o$ for $0 \leq z \leq \frac{L}{2}$ and $R_z = R_o - 2(\frac{R_o - R_i}{L})(z - \frac{L}{2})$ for $\frac{L}{2} \leq z \leq L$.

Using Eq. 3.15, I_{str} through different cross-sections along the capillary length is expressed as below :

$$I_{str}(z) = \frac{\epsilon_o \epsilon_{rs} \Delta P \zeta}{\mu L} \frac{1}{f_B(R_i/R_o)} \frac{{R_o}^4}{{R_z}^2} \cos\theta_B \tag{3.28}$$

where, $\cos\theta_B = 1$, for $0 \leq z \leq \frac{L}{2}$ and $\cos\theta_B = \frac{L}{\sqrt{4(R_o - R_i)^2 + L^2}}$ for $\frac{L}{2} \leq z \leq L$.

The total U_{str} developed across capillary B is evaluated and expressed in terms of non-dimensional size ratios $\gamma_1(R_i/R_o)$ and $\gamma_2(R_o/L)$ as shown below :

$$U_{str} = \frac{\epsilon_o \epsilon_{rs} \Delta P \zeta}{\mu \kappa} \left(\frac{3{\gamma_1}^3 + (1 + \gamma_1 + {\gamma_1}^2) \frac{1}{\sqrt{1+4{\gamma_2}^2(1-{\gamma_1}^2)}}}{1 + \gamma_1 + {\gamma_1}^2 + 3{\gamma_1}^3} \right) \tag{3.29}$$

3.4.1.3 Capillary C

The pressure gradient along the length of Capillary C is given by :

$$-\frac{dP}{dz} = \frac{\Delta P}{L} \frac{1}{f_C(R_i/R_o)} \frac{{R_o}^4}{{R_z}^4} \tag{3.30}$$

where, $f_C(R_i/R_o) = \frac{3+\gamma_1+{\gamma_1}^2+{\gamma_1}^3}{6{\gamma_1}^4}$ with $\gamma_1 = R_i/R_o$, and $R_z = R_o - 2(\frac{R_o - R_i}{L})(z - \frac{L}{2})$ for $0 \leq z \leq \frac{L}{2}$ and $R_z = R_i$ for $\frac{L}{2} \leq z \leq L$.

As in the case of capillaries A and B, the I_{str} through different cross-sections of capillary C is obtained using Eq. 3.15 as given below,

$$I_{str}(z) = \frac{\epsilon_o \epsilon_{rs} \Delta P \zeta}{\mu L} \frac{1}{f_C(R_i/R_o)} \frac{{R_o}^4}{{R_z}^2} \cos\theta_C \tag{3.31}$$

where, $\cos\theta_C = \frac{L}{\sqrt{4(R_o - R_i)^2 + L^2}}$, for $0 \leq z \leq \frac{L}{2}$ and $\cos\theta_C = 1$ for $\frac{L}{2} \leq z \leq L$.

The total U_{str} developed across capillary C could also be expressed in terms of non-dimensional size ratios $\gamma_1(R_i/R_o)$ and $\gamma_2(R_o/L)$, as shown below :

$$U_{str} = \frac{\epsilon_o \epsilon_{rs} \Delta P \zeta}{\mu \kappa} \left(\frac{3 + (\gamma_1 + {\gamma_1}^2 + {\gamma_1}^3) \frac{1}{\sqrt{1+4{\gamma_2}^2(1-{\gamma_1}^2)}}}{3 + \gamma_1 + {\gamma_1}^2 + {\gamma_1}^3} \right) \tag{3.32}$$

3.4.1.4 Capillary shape dependence of I_{str} and U_{str} generation

The variation of the generated I_{str} in capillaries A, B, and C, as given by Eqs. 3.24, 3.28, and 3.31, respectively, is plotted in Fig. 3.3(D) for a particular set of values of R_o, R_i, and L (30 μm, 10 μm, 300 μm, respectively). The values of R_o, R_i, and L are so chosen to ensure that $\frac{R_O - R_i}{L} \ll 1$, such that the lubrication approximation is applicable. It is easily identifiable from Fig. 3.3(D) that the contrasting shapes of capillaries lead to significant differences in the generated I_{str}.

The Eqs. 3.26, 3.30, 3.32 give the total U_{str} generated across the capillaries A, B and C, respectively. For each capillary, it is possible to define a shape correction factor (U_{scf}) as the ratio of the analytically obtained U_{str} and that given by the H-S equation $U_{str\text{-}HS}$:

$$U_{scf} = \frac{U_{str}}{U_{str\text{-}HS}} = \frac{U_{str}}{\left(\frac{\epsilon_0 \epsilon_{rs} \Delta P \zeta}{\mu \kappa}\right)} = U_{scf}(\gamma_1, \gamma_2) \tag{3.33}$$

The extent to which capillary shapes affect the generated U_{str} could be identified by plotting the function $U_{scf}(\gamma_1, \gamma_2)$ for the capillaries A-C, as shown in Fig. 3.3(E). For this plot, γ_2 is kept fixed at 0.1, whereas γ_1 is varied from 0.2 to 1. It can be easily identified from Fig. 3.3(E) that U_{str} generated in capillaries not only changes significantly with the size ratio γ_1, but is also dependent on the capillary shape (A, B or C). The results demonstrate that both I_{str} and U_{str} generation could be significantly sensitive to geometry, and these effects should thus be duly accounted for to achieve better accuracy in measurements. This effect is expected to increase significantly for larger values of $\frac{R_O - R_i}{L}$.

3.4.2 Square fiber array (model porous media)

3.4.2.1 Flow parallel to fiber axes

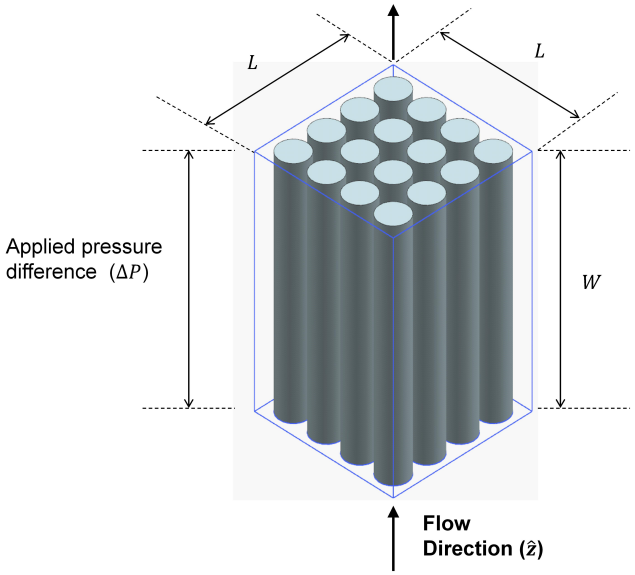

Figure 3.4.: A square array of cylindrical fibers with pressure difference applied parallel to the fiber axes.

We consider a porous structure in the form of a square array of cylindrical fibers with dimensions of $L \times L \times W$ (as shown in Fig. 3.4). Considering that a pressure difference of ΔP is applied across the fiber array in the direction parallel to the fiber axes, the generated I_{str} and U_{str} could be evaluated using the general expressions given by Eq. 3.15 and 3.20.

As the sample geometry is unchanged along the pressure gradient direction, the pressure gradient is uniform along sample length, and is equal to $\Delta P/W$. Furthermore, as liquid flow at all the

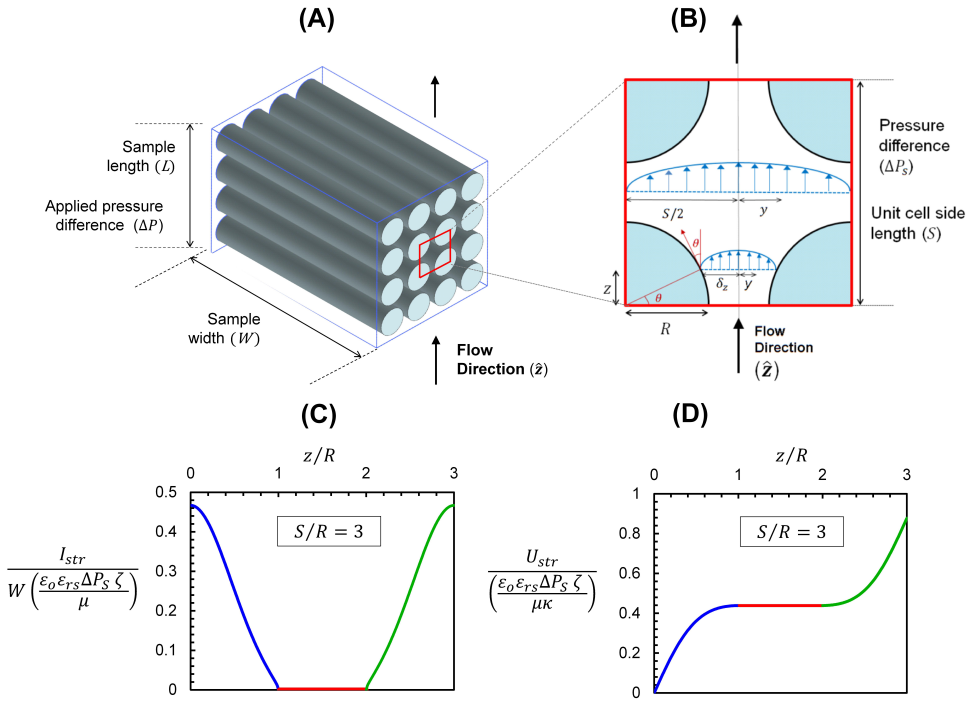

Figure 3.5.: (A) Square array of cylindrical fibers with pressure difference applied normal to the fiber axes, (B) Geometry of unit cells constituting the fiber array, and variation of the generated streaming current (C) and streaming potential (D) along the length of the unit cell.

solid surfaces is aligned with pressure gradient direction, the $\cos\theta$ term in Eq. 3.15 and 3.20 is equal to 1. Upon simplification, it is found that I_{str} and U_{str} generated in the fiber array are the same as given by the parallel capillary model (Eqs. 3.4 and 3.5). This leads us to the general conclusion that the parallel capillary model holds irrespective of the type of arrangement of fibers (i.e square/hexagonal/random), as long as all the fiber axes are oriented parallel to the pressure gradient direction. Adamczyk et. al. [42] established the same result for straight channels with different cross-sectional geometries.

3.4.2.2 Flow normal to fiber axes

In this section, we consider a square array of fibers with a pressure difference of ΔP being applied perpendicular to the fiber axes, as shown in Fig. 3.5(A). In order to simplify our analysis, we consider the square fiber array to be made up of identical unit cells, as shown in Fig. 3.5(B). The side length of the unit cell is S, and the fiber radius is equal to R. If the number of unit cells along the sample length in the pressure gradient direction is n, the pressure difference across a single unit cell is $\Delta P_s = \Delta P/n$.

The macroscopic liquid flow velocity inside such a unit cell can be approximated by the following relationship [70] :

$$V_z(y) = -\frac{1}{2\mu}\frac{dP}{dz}(\delta_z{}^2 - y^2) \tag{3.34}$$

where, δ_z is the width of liquid part of a unit cell cross-section located at a height of z along its length with $\delta_z = S/2 - \sqrt{R^2 - z^2}$ for $0 \leq z \leq R$, and $\delta_z = S/2$ for $R \leq z \leq S/2$, as shown in Fig. 3.5(B). In the derivation of Eq. 3.34 it can be assumed that the flow velocity at the borderline of two laterally adjoining unit cells is zero due to the existence of dead zones at it's ends [70].

As the unit cell is symmetrical along its horizontal center line, the liquid flow characteristics in the lower and upper halves of the unit cell are identical. It is therefore sufficient to carry out the analysis only for the lower half of unit cell ($0 \leq z \leq S/2$), and use equivalent values for the upper half ($S/2 \leq z \leq S$).

The volumetric liquid flow rate (Q) through a certain unit cell cross-section could be obtained as shown below :

$$Q = \int_{-\delta_z}^{+\delta_z} V_z(y) W dy = -\frac{2{\delta_z}^3}{3\mu} W \frac{dP}{dz} \tag{3.35}$$

Given that ΔP_s is the total pressure difference across the unit cell, ΔP_s could be expressed in terms of the volumetric liquid flow rate (Q) by integrating Eq. 3.35 along the unit cell length $0 \leq z \leq S$:

$$\Delta P_s = \frac{3\mu Q}{2W} \left\{ 2 \left(\int_0^R \frac{1}{{\delta_z}^3} dz + \int_R^{S/2} \frac{1}{{\delta_z}^3} dz \right) \right\} \tag{3.36}$$

The pressure gradients in different unit cell cross-sections could be obtained by substituting the value of Q from Eq. 3.36 in Eq. 3.35 :

$$-\frac{dP}{dz} = \Delta P_s \frac{1}{f_s(S/R)} \frac{R^2}{{\delta_z}^3} \tag{3.37}$$

where, $f_s(S/R)$ is a function of the size ratio S/R, and has been provided in its complete form in the Appendix.

A similar approach, as described above, has been used by Tamayol et. al. [70] to square fiber arrays for estimation of viscous permeability, and a good agreement with experimental data was obtained. This shows that the applicability of the approximate solution for describing pressure-driven liquid flow inside the unit cells is good.

With the pressure gradients inside the unit cell known, the generated I_{str} inside the unit cell could be obtained using Eq. 3.15. The other two variables in Eq. 3.15 are $\cos\theta_s$ and A_c. The $\cos\theta_s$ term which represents the solid surface orientation with respect to the z-direction could be expressed as a function of the non-dimensional height z/R :

$$\cos\theta_s = \frac{\sqrt{R^2 - z^2}}{R} = \sqrt{1-(z/R)^2} \tag{3.38}$$

The A_c term in Eq. 3.15 which is the area of liquid part in a unit cell cross-section is equal to $\delta_z W$. Upon substituting the expressions for $-\frac{dP}{dz}$, $\cos\theta_s$, and A_c in Eq. 3.15, I_{str} generated in the region $0 \leq z \leq R$ of the unit cell could be obtained. In the unit cell region $R \leq z \leq S/2$, I_{str} is equal to 0 due to the complete absence of solid surfaces. I_{str} generated in different parts of the unit cell is given by the following expression:

$$I_{str}(z/R) = \begin{cases} \frac{\epsilon_o \epsilon_{rs} \Delta P_s \zeta}{\mu} W \frac{1}{f_s(S/R)} \frac{\sqrt{1-(z/R)^2}}{(S/2R - \sqrt{1-(z/R)^2})^2} & \text{, if } 0 \leq z \leq R, \\ 0 & \text{, if } R \leq z \leq S/2. \end{cases} \tag{3.39}$$

The generated U_{str} in the the unit cell ($0 \leq z \leq S/2$) can similarly be obtained using Eq. 3.20:

$$U_{str}(z/R) = \begin{cases} \frac{\epsilon_o \epsilon_{rs} \Delta P_s \zeta}{\mu\kappa} \frac{g_s(z/R, S/R)}{f_s(S/R)} & \text{, if } 0 \leq z \leq R, \\ \frac{\epsilon_o \epsilon_{rs} \Delta P_s \zeta}{\mu\kappa} \frac{g_s(z/R, S/R)}{f_s(S/R)}\Big|_{z/R=1} & \text{, if } R \leq z \leq S/2. \end{cases} \tag{3.40}$$

where, $g_s(z/R, S/R)$ is a function of the non-dimensional height z/R, and the size ratio S/R. It has been provided in its complete form in the Appendix.

The Eqs. 3.39 and 3.40 allow us to directly estimate the variation of generated I_{str} and U_{str} inside the unit cells. This variation is plotted for a particular value of the size ratio $S/R = 3$, as shown in Fig. 3.5(C)-(D). It could be identified from Fig. 3.5(C) that the generated I_{str} is highest in the cross-section where the separation between fibers is minimum. The gradient of U_{str} with respect to z is maximum for the same cross-section.

The total U_{str} generated across the unit cell ($0 \leq z \leq S$) is twice of the U_{str} generated across its lower half ($0 \leq z \leq S/2$), and could be expressed as :

$$U_{str} = 2\frac{\epsilon_o \epsilon_{rs} \Delta P_s \zeta}{\mu\kappa} \frac{g_s{}^*(S/R)}{f_s(S/R)}, \tag{3.41}$$

where, $g_s{}^*(S/R) = g_s(z/R, S/R)\Big|_{(z/R)=1}$.

It could be remarked from from Eq. 3.41 that the total U_{str} generated across the unit cell is independent of fiber radius, and dependent only on the size ratio S/R, which is in turn related to the porosity (ϕ) of the fiber array :

$$\frac{S}{R} = \sqrt{\frac{\pi}{1-\phi}} \tag{3.42}$$

Thus, U_{str} developed across the unit cell could be thus expressed only as a function of porosity (ϕ) :

$$U_{str} = \frac{\epsilon_o \epsilon_{rs} \Delta P_s \zeta}{\mu \kappa} h_s(\phi) \tag{3.43}$$

where, $h_s(\phi) = 2\frac{g_s{}^*(S/R)}{f_s(S/R)}\Big|_{S/R=\sqrt{\frac{\pi}{1-\phi}}}$.

3.4.2.3 Effect of fiber orientation and sample porosity

In this section, the variation of I_{str} and U_{str} generated in the square array of fiber with sample porosity (ϕ) is plotted for both parallel and transverse orientation of fibers, as shown in Fig. 3.6(A)-(B). It is identifiable from the plots that the generation of both I_{str} and U_{str} is highly sensitive to both fiber orientation and porosity.

Effect on streaming current: Since in the case of transverse fiber orientation the generated I_{str} does not have a uniform value for all cross-sections along the unit cell length, we plot both (i) the maximum I_{str} in the unit cell ($I_{str}{}^{max}$), and (ii) the length-averaged I_{str} value ($I_{str}{}^{avg}$). It is observed from Fig. 3.6(A) that both $I_{str}{}^{max}$ and $I_{str}{}^{avg}$ are greater in the case of parallel fiber orientation than the case of transverse fiber orientation. This clearly shows that apart from porosity, the fiber orientation has a significant effect on the streaming current. Furthermore, when we consider the variation of streaming current with porosity, it can be identified that in both the two fiber orientation cases, the variation of $I_{str}{}^{max}$ and $I_{str}{}^{avg}$ with sample porosity is almost linear.

Effect on streaming potential: As described earlier, in the case of parallel fiber orientation, the generated U_{str} is equal to that given by the H-S equation ($U_{str\text{-}HS}$), and hence does not change with porosity. In the case of transverse fiber orientation, the generated U_{str} is only a function of the porosity, and it is independent of the dimensions of the fiber. The variation of U_{str} with porosity is shown in Fig. 3.6(B). It can be further noted from Fig. 3.6(B) that the difference between U_{str} generated in the two cases of parallel and transverse fiber orientation increases with sample porosity. Therefore, in the tranverse fiber orientation case, the deviation of U_{str} from the prediction of the H-S Equation increases with porosity. This indicates that in measurements involving porous substrates, the deviation of measured U_{str} from $U_{str\text{-}HS}$ due to the geometrical non-idealities would be low for densely packed samples, i.e. samples with low porosity.

3.4.2.4 Effect of sample dimensions

In the case of transverse fiber orientation, if the number of sample unit cells along the direction of applied pressure gradient is n, and ΔP is the total pressure difference applied across the

sample, the pressure drop across a single unit cell (ΔP_s) equals $\Delta P/n$. Similarly, if ${U^t}_{str}$ is the total streaming potential generated across the sample, the streaming potential generated across a single unit cell is ${U^t}_{str}/n$. Upon substituting for U_{str} and ΔP_s in Eqs. 3.39 and 3.43 in terms of ${U^t}_{str}$ and ΔP the dependence of the generated ${I^t}_{str}$ and ${U^t}_{str}$ on ΔP, n, and W could be identified.

Effect on streaming current: It is easily identifiable from Eq. 3.39 that I_{str} generated inside the unit cells decreases linearly with the number of unit cells along the pressure gradient direction (n). However, increasing the width of the sample (W) leads to a proportional increase in I_{str} generated inside the unit cells. Thus, at fixed sample porosity the magnitude of streaming current is sensitive to the ratio n/W. This inference is analogous to the prediction of H-S equation that the generated I_{str} is proportional to the cross-sectional area, and inversely proportional to the sample length.

Effect on streaming potential: The relationship given by Eq. 3.43 shows that U_{str} generated across unit cells is only dependent on the pressure difference across unit cells (ΔP_s), and porosity (ϕ). Furthermore, when ΔP_s and U_{str} are substituted in terms of ΔP and ${U^t}_{str}$ in Eq. 3.43, the number of unit cells factor (n) gets cancelled from both the sides. As a result, ${U^t}_{str}$ and ΔP are relatable via the same equation as U_{str} and ΔP (Eq. 3.43). It could be thus established that at constant porosity, the generated ${U^t}_{str}$ is independent of the physical dimensions of the porous sample.

3.4.3 Implications of obtained results in practical use

3.4.3.1 Applicability of the presented theory in practical applications

As stated in the Introduction, the theory presented in this work has the same prerequisite conditions as the H-S equation. Therefore, when considering the implications of this theory in practical cases, it is necessary to ensure that these prerequisite conditions are satisfied. The most important prerequisite condition is that the EDL thickness (δ_{EDL}) should be small in comparison to pore sizes in the substrate. When the pore sizes (a) are known, this condition could be satisfied by adjusting the the bulk electrical conductivity such that $\frac{\delta_{EDL}}{a} \ll 1$. Furthermore, if this condition is satisfied, electroviscous effects could also be neglected [64, 65].

The other important prerequisite condition is that surface conductivity effects should be negligible. If the absence of surface conductivity effects in a substrate has been shown independently, it is possible to directly apply our theoretical treatment. However, if it is not already known, it is important to ascertain if surface conductivity effects are present, and whether they could be neglected at the conditions chosen for the experiments. For a substrate of known geometry, one can identify if surface conductivity effects are present via measurements of effective conductivities of the electrolyte inside the substrate. The measured effective conductivity value is compared with the value that is obtained theoretically for the substrate under the assumption that surface conductivity effects are absent. When the measured effective conductivity is higher than the theoretically predicted value, the presence of surface conductivity effects is implied. In the case of real substrates with complex geometries like fiber plugs, a precise theoretical estimation of the effective conductivity requires information about the geometric features such as plug porosity

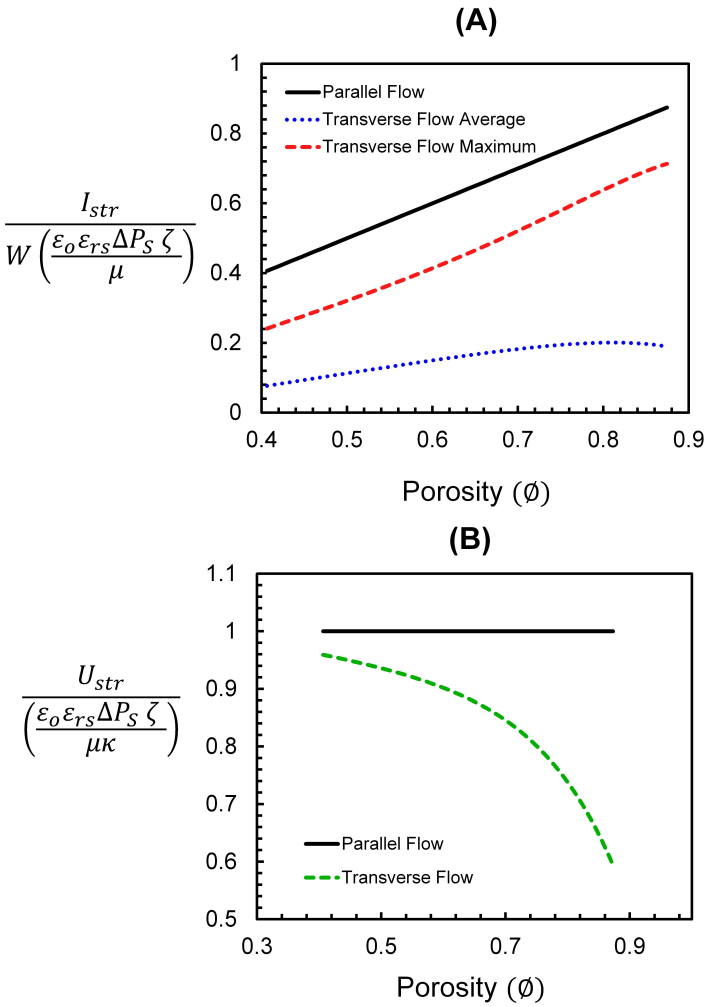

Figure 3.6.: Variation of the generated streaming current (maximum and average value) (A), and the generated streaming potential (B) with porosity in square fiber arrays for parallel and transverse flow directions.

and fiber orientation as shown by Pietrak et. al. for the similar case of thermal conductivity [72].

When dealing with fiber plugs, another commonly used approach is to compare the measured effective conductivities obtained at different packing densities with the bulk electrical conductivity [51]. If the measured effective conductivity increases with packing density and surpasses the bulk electrical conductivity, the presence of surface conductivity is implied. In such cases, the bulk electrical conductivity could be increased by increasing the electrolyte concentration until the effect of surface conductivity is minimized. This should be doable for substrates with low and moderate surface conductivities. Measuring the streaming potential at such a high bulk electrical conductivity level could be thus a way of eliminating the effect of surface conductivity on the final zeta potential measurement.

3.4.3.2 Differences between I_{str} and U_{str} approaches

The theoretical analysis carried out in this work demonstrates that the generation of both I_{str} and U_{str} is intricately linked to sample geometry. Under a certain applied pressure difference, I_{str} generation is shown to be dependent on both, the intrinsic geometrical features of the sample such as porosity and fiber orientation, as well as its physical dimensions. The theoretical results, however, indicate that U_{str} generation is only dependent on the intrinsic geometric features of the sample, and is unaffected by sample size. This inference implies that U_{str} measurements would be reproducible even on set-ups with different measurement cells given that the samples used have the same intrinsic geometry. For instance, in the case of single fibers plugs, this could be done by maintaining the same packing density in the different samples. This conclusion will, however, need to experimentally verified. It is in contrast to I_{str} measurements where the measurement cell size plays a direct role, and needs to be accounted for as well.

Another practically important aspect that is brought to light is that the generated I_{str} does not have a single uniform value for the sample, and could vary along the sample length from one cross-section to another. However, in the experiments where I_{str} values are detected externally using electrodes placed at opposite ends of the sample. The electrodes are placed the same potential and a single value for the current flowing through the electrodes is obtained [36]. Although this externally measured current is equivalent to the streaming current for samples with uniform cross-sections, the relationship between the externally detected current and the I_{str} generated inside a sample with non-uniform cross-sections is not well understood. Therefore, in order to ensure the reliability of ζ determination via I_{str} measurements, there is a need for further theoretical work.

3.4.3.3 Optimization of ζ determination via U_{str} measurements

When using U_{str} measurements to estimate ζ, an important question is whether the accuracy of ζ estimation could be improved by optimizing sample geometry. Such an optimization could be aimed at minimizing the deviation of generated U_{str} from that given by the H-S equation ($U_{str\text{-}HS}$). This question is specially relevant when dealing with samples such as porous fiber plugs where the packing density can be varied to change sample geometrical features such as fiber orientation and sample porosity. Using the obtained results, three different approaches are suggested for optimizing the fiber plug geometry for more precise ζ determination.

The first approach is based on the results obtained for U_{str} generation in square fiber arrays, as shown in Fig. 3.6(A). It could be remarked from Fig. 3.6(A) that the difference in U_{str} generation in the two contrasting cases of parallel and transverse fiber orientation is reduced at low sample porosity. Therefore, using highly dense fiber plugs with low porosity could be one possible way of minimizing the deviation of generated U_{str} from $U_{str\text{-}HS}$. Although theoretically viable, this approach would not be easily implementable in practice, since (i) compressing single fibers into such highly dense plugs could be very difficult, and (ii) obtaining appreciable liquid flow rates through such dense plugs would require much higher pressure differences than attainable in presently used commercial devices [25]. As most commercial devices use vacuum chambers, the maximum applied pressure difference is typically limited to 1 atm.

In the second approach for a precise estimation of ζ, we utilize the general observation from Eq. 3.19 that any non-ideal sample geometry which deviates from the parallel flow configuration, leads to negative deviations of the generated U_{str} from $U_{str\text{-}HS}$. Thus, if measurements are carried out for a range of fiber packing density values which in turn produce samples with different fiber orientations and porosities, the maximum obtained value of U_{str} among these measurements would be closest to $U_{str\text{-}HS}$. Therefore, when using the H-S equation, the highest obtained U_{str} values should hence be used for zeta potential determination. This approach could be more useful in experiments, as it provides us a way of working within the experimental limitations.

As the third approach, which might be useful in cases where a very accurate measurement of ζ is desired, we suggest the direct usage of Eqs. 3.19 as the relationship between ζ and U_{str}. This would of course be restricted to those cases for which the earlier described conditions required for the applicability of our theory are satisfied. Furthermore, this would require a full characterization of the substrate geometry. If the surfaces in sample cross-sections are not identically oriented, it would be necessary to obtain accurate liquid flow velocity profiles and shear stresses inside the substrate. Although obtaining analytical solutions might not be feasible for real substrates, numerical simulations could be implemented using representational 3D models to obtain a very precise relationship between ζ and U_{str} [73]. This could be a subject of future investigations.

3.5 Summary

This chapter presents an analytical treatment of pressure-driven generation of streaming current (I_{str}) and streaming potential (U_{str}) in samples which are geometrically complex, and for which the classical Helmholtz-Smoluchowski equation is known to be inaccurate. As streaming potential measurements are used extensively in subsequent chapters of this thesis, this chapter also provide the necessary theoretical background for this technique. Firstly, using linear velocity profiles inside electric double layers, a general expression is obtained to describe the I_{str} generated in different cross-sections of the sample. Thereafter, assuming that the generated U_{str} varies only along the pressure gradient direction, an expression is obtained to describe the variation of the generated U_{str} along sample length. The conditions required for the validity of this analytical approach are the same as those required for the Helmholtz-Smoluchowski equation. Additionally, surface conductivity effects have not been accounted for. The general expressions describing I_{str} and U_{str} generation form the basic theoretical framework of this work which is applied to several substrate geometries. The considered geometries include a set of 3 non-uniform cross-sectional capillaries, and square array of fibers (model porous media) for both parallel and transverse fiber orientation. The obtained results are used to illustrate that non-ideal sample geometries induce deviations in the generated I_{str} and U_{str} from the values given by the Helmholtz-Smoluchowski equation. The implications of the obtained results for experimental zeta potential determination are discussed. For the important case of fiber plugs, strategies are suggested that can be utilized to make more precise ζ measurements.

4 Deposition of cationic vesicles on single anionic cellulose fibers

This chapter describes the methodology and results of the experimental investigations on the deposition of cationic esterquat vesicles on single anionic cellulose fibers. The chapter starts with an introduction outlining the background of particle and vesicle deposition processes. This is followed by a description of the materials and experimental methods. Thereafter, the relevance of streaming potential measurements to studying colloidal deposition processes is described. The results and discussions section describes the final experimental findings and presents the mechanisms that can be used to explain the observations.

This chapter is based on the articles, *Intact deposition of cationic vesicles on anionic cellulose fibers : Role of vesicle size, polydispersity, and substrate roughness studied via streaming potential measurements*, by Kumar et al. (2016) published in the Journal of Colloid and Interface Science, and *Influence of lipid bilayer phase behaviour and substrate roughness on the pathways on intact vesicle deposition : A streaming potential study* by Kumar et al. (2017) published in Colloids and Surfaces A: Physicochemical and Engineering Aspects.

4.1 State-of-the-art

The deposition of cationic vesicles on anionic surfaces is driven by electrostatic attractive forces. Therefore, it forms an efficient and swift way of transporting encapsulated active ingredients to substrate surfaces [74]. Vesicle deposition on solid surfaces primarily results in either, (i) supported lipid bilayer (SLB) formation, if the vesicles disintegrate upon attachment [75] or upon attainment of a certain critical surface coverage [76, 77], or (ii) supported vesicular layer (SVL) formation, if the vesicles exist as intact entities in the equilibrium adsorbed layer [78]. While SLB formation has been observed on a wide range of surfaces including silica, mica, glass and quartz [79–81], SVL formation has also been reported on some substrates such as TiO_2, oxidized Pt and Au, and cellulose [12, 82–85].

Recent works have provided significant insights into the mechanism of SLB formation, and it is well understood that as SLB formation requires the breakdown of deposited vesicles, there exists an energy barrier which opposes the transition and needs to be overcome[86]. The magnitude of the energy barrier is determined by factors controlling vesicle stability [87, 88]. In the case of SLB formation, the energy barrier is overcome mostly by vesicle-substrate and/or vesicle-vesicle interaction energies. However, if the existing energy barrier is greater than the maximum interaction energy reached during the deposition process, deposited vesicles stay intact resulting in SVL formation.

The mechanism of intact vesicle deposition has been in a few preliminary studies found to be similar to that of deposition of solid particles which can be described by the random sequential

adsorption (RSA) model [89, 90]. In the RSA model, deposition is considered a 3-step process involving: (i) transport of particles from the bulk to the solid-liquid interface, (ii) intimate contact of the particle with the interface, and (iii) attachment or no attachment of particles to the interface depending upon the occupied or unoccupied state of the surface [91]. Particles are considered to get immobilized upon deposition and form a monolayer on the solid surface. Deposition proceeds until the surface is occupied in such a way that all possible pathways of attachment of unadsorbed particles to the substrate are blocked, which in the case of monodisperse particles results in a maximum surface coverage of 0.547 [92].

In earlier works, the RSA model has been used to explain the deposition characteristics of several types of colloids such as polyelectrolytes and proteins on different kinds of solid surfaces [91]. The RSA model is, however, valid only if colloids are immobilized upon deposition, and it is known to be inapplicable in cases where surface mobility has been observed in deposited colloids [93, 94]. In the case of vesicles, however, the effect of factors such as vesicle size, lipid bilayer phase behavior, and substrate roughness which might influence vesicle deposition in real-life applications has not been sufficiently investigated.

In this chapter, two different types of vesicles composed of chemically similar lipids but having different morphological properties due to the constituent lipid bilayers existing in the solid-gel and liquid-crystalline phases, respectively, are studied for their deposition behavior on both smooth and rough substrates. The lipids used, namely DEEDMAC (ditallowethylester dimethylammonium chloride) and Rewoquat WE15 (ditallowcarboxyethyl hydroxyethylmethylammonium methosulfate), are esterquats, commonly used in fabric softener formulations. Since these lipids are used in real-life for conditioning textiles, textile fibers were chosen to be used as adsorbents. Anionic textile fibers, namely cotton (natural cellulose fiber) and viscose (regenerated cellulose fiber), having rough and smooth surfaces, respectively, were selected. The properties of bioth, the vesicles as well as the single fibers are described in detail in Chapter 2.

We first examine the fate of vesicles upon deposition via fluorescence microscopy, and establish that both DEEDMAC and WE15 vesicles deposit as intact entities on anionic cellulose surfaces to form stable SVLs. Thereafter, the equilibrium deposition results on smooth and rough cellulose fibers are contrasted to draw insights into the roles played by substrate roughness and lipid bilayer phase behavior linked vesicle properties. These inferences are further substantiated by comparing the profiles of variation of fiber apparent zeta potential with vesicle deposition for different vesicle-substrate combinations.

4.2 Materials and Methods

4.2.1 Materials

The preparation and properties of large ($d_{avg} \sim 10\ \mu m$) and small ($d_{avg} < 1\ \mu m$) DEEDMAC and WE15 vesicles used for the investigation described in this chapter are described in Chapter 2. The properties of the single cellulose fibers, namely cotton and viscose, used as deposition substrate for the investigations are also described in Chapter 2.

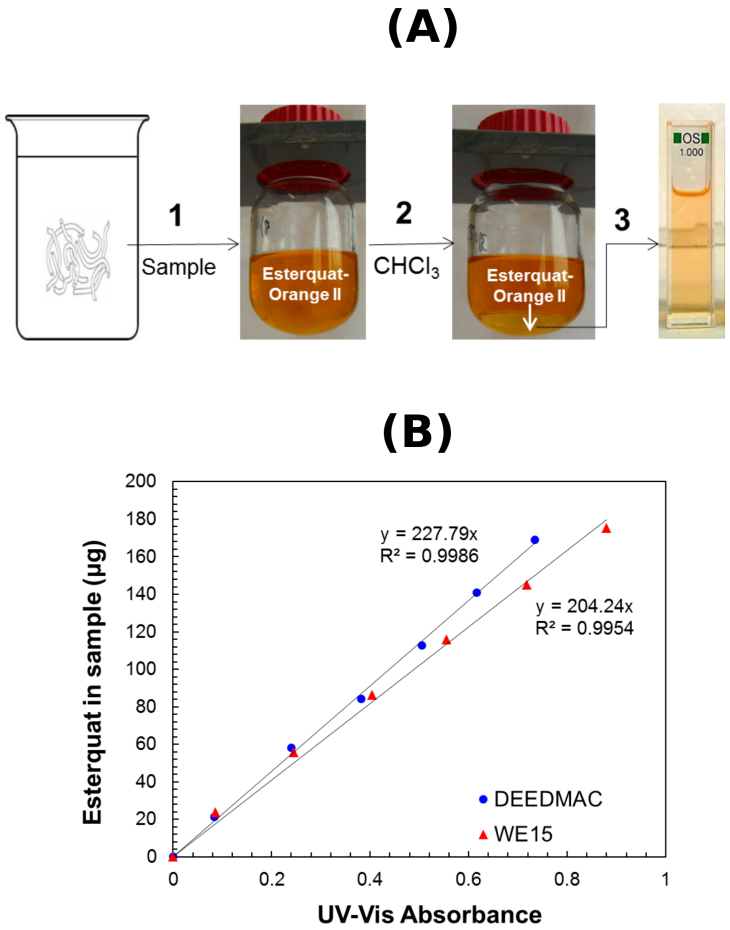

Figure 4.1.: (A) Experimental procedure for bulk esterquat concentration determination : (1) Formation of esterquat-Orange II complex, (2) extraction of the complex in chloroform, (3) measurement of chloroform phase UV-Vis absorbance, (B) Calibration curve for DEEDMAC and WE15 concentration determination

4.2.2 Spectrophotometric determination of esterquat concentrations

Cationic esterquat molecules interact with Orange II, an anionic dye, to form one to one complexes which are insoluble in water but are soluble and extractable in chloroform, and exhibit a UV-Vis absorption spectrum [95]. The UV-Vis absorbance of the post-extraction chloroform phase is proportional to the esterquat-Orange II complex concentration, which is in-turn proportional to esterquat concentrations in initial samples. A brief description of the experimental procedure and the calibration curve obtained using esterquat solutions of known concentrations in methanol is shown in Fig.4.1. This method is used to quantify deposition on the fibers by characterizing esterquat depletion in the bulk liquid due to deposition.

4.2.3 Streaming potential measurements

In this work, streaming potential measurements have been performed for bare fibers and for fibers with varying amounts of deposited vesicles. Streaming potential measurements were

carried out on the Fiber Potential Analyzer (FPA) from AFG Analytic GmbH. A certain mass of fibers, bare or after vesicle deposition, is packed inside the electrokinetic cell provided in the device to form a plug, and an electrolyte of fixed conductivity (1 mS/cm) is flown through it at two pressure difference levels, (P_{atm}-$P_{vacuum1}$) and (P_{atm}-$P_{vacuum2}$), as shown schematically in Fig. 4.2(A). When the applied pressure difference switches between the two values, the streaming potential developed between the electrodes changes by the value ΔU_{str}. A single measurement consists of several such switches, and ends when ΔU_{str} values converge.

In Chapter 3, a new theory was proposed to account for the effect of sample geometry on U_{str} measurements. In the case of single fiber plugs, the model predicts that the measured U_{str} depends upon both the fiber orientation as well as plug porosity. Although, it is difficult to apply the same model for the present system as the exact sample geometry can be easily characterized. However, by keeping the fiber plug density constant across all measurements, any changes in streaming potential due to vesicle deposition could be effectively tracked. Therefore, we use a differential form of Helmholtz-Smoluchowski equation is used to calculate the "apparent zeta potential" (ζ_{app}) of the fibers which incorporates the geometry effects :

$$\Delta U_{str} = \frac{\epsilon_o \epsilon_{rs}}{\mu \kappa} \left(P_{vacuum2} - P_{vacuum1} \right) \zeta_{app} \tag{4.1}$$

4.2.4 Deposition experiments

The vesicle dispersions were diluted with ultrapure (Milli-Q) water to different esterquat concentration levels, and a fixed mass of the fibers (1.5 g), pre-swollen in water, was added. The treatment was carried out in plastic bottles to avoid deposition of vesicles on vessel surfaces. The bottles were placed on a shaker for overnight equilibration, after which the bulk liquid was sampled for determination of residual esterquat concentration. The resultant adsorption density, i.e. mass of esterquat deposited per unit adsorbent mass, is calculated based on the measurement of esterquat depletion in the bulk liquid. Next, the equilibrated fibers were packed in the FPA cell (volume 9 ml) for streaming potential characterization. The electrolyte used is an aqueous solution of sodium chloride with a conductivity of 1 mS/cm. A sequence of 5-10 runs was made to ensure that any unadsorbed vesicles are washed away and ΔU_{str} values get stabilized, as shown in 4.2(C). The stable ΔU_{str} values are then used to calculate apparent zeta potentials using Eq. 4.1.

4.2.5 Fluorescence microscopy visualization of deposited vesicles

The fluorescent labelled esterquat vesicles deposited on anionic cellulose fibers were visualized via fluorescence microscopy using a Nikon Eclipse-Ti microscope. A cellulose fiber membrane (Sartorius FT-3-127-090) was used as the deposition substrate instead of the single fibers to facilitate it's imaging. The cellulose fiber membrane was treated with the vesicles by fully immersing the paper in vesicle dispersions.

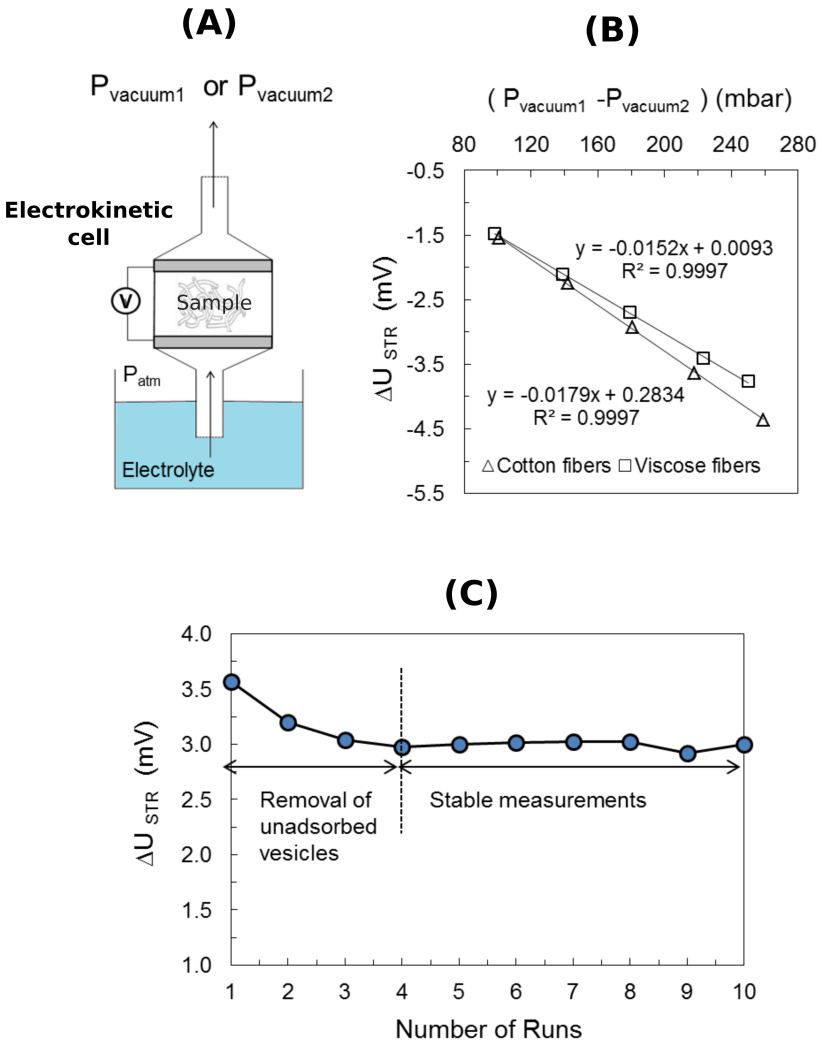

Figure 4.2.: (A) Schematic representation of the streaming potential measurement setup, (B) Variation of streaming potential of viscose and cotton fiber plugs (1.5 g) with differences in pressure difference levels ($P_{vacuum2}$ was fixed at 100 mbar, and $P_{vacuum1}$ was varied from 180 to 350 mbar), and (C) Variation of ΔU_{str} with the number of runs during a typical measurement on fibers with deposited vesicles

4.3 Investigations on colloidal deposition via streaming potential measurements

Adamczyk et al. [96] suggested that streaming potential measurements can be used to identify the post-deposition conformation of colloids, and used this idea to investigate the fate of polyelectrolytes upon deposition on mica. The proposed method involves characterizing the variation of substrate streaming potential with deposition progress, and using the profile of this variation to draw inferences about the state of the final adsorbed layer. It is established that for monolayer particle deposition, the general expression for streaming potential variation with surface coverage is given by the following equation [42] :

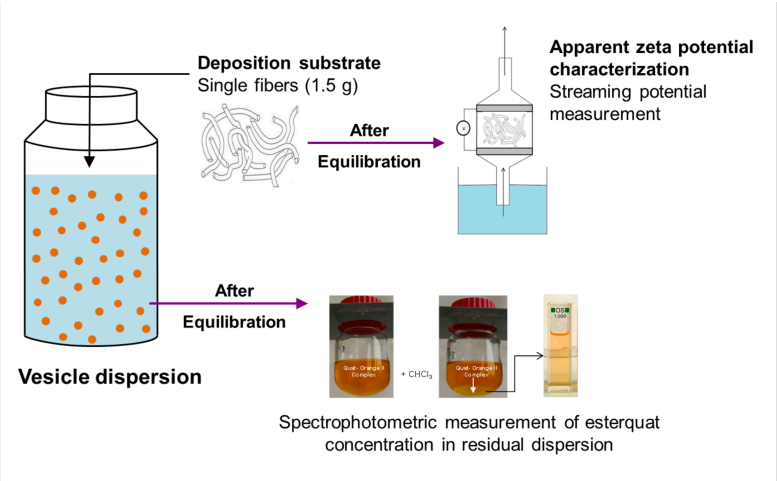

Figure 4.3.: Schematic representation of the experimental methodology for characterization of equilibrium vesicle deposition on single cellulose fibers

$$\frac{U_{\mathrm{str}}(\theta)}{U_{\mathrm{O}}} = 1 - A_{\mathrm{i}}(\theta)\theta + A_{\mathrm{P}}(\theta)\theta\frac{\zeta_P}{\zeta_O} \tag{4.2}$$

where, U_{O} and U_{str} are the substrate streaming potential before deposition and at a nominal surface coverage θ, and ζ_{P} and ζ_{O} are zeta potential values of the particle and the bare substrate, respectively. $A_{\mathrm{i}}(\theta)$ and $A_{\mathrm{P}}(\theta)$ are functions of the surface coverage (θ), and are dependent on the substrate morphology, and the shape and orientation of colloids in the adsorbed layer.

The dependencies $A_{\mathrm{i}}(\theta)$ and $A_{\mathrm{P}}(\theta)$, for deposition of monodisperse spherical particles on flat surfaces, have been computed and approximated to an accuracy better than 1% by the following analytical expressions [97]:

$$A_{\mathrm{i}}(\theta) = \frac{10.2 - 5.75\theta}{1 + 5.46\theta}, \quad A_{\mathrm{P}}(\theta) = \frac{6.51 - 2.38\theta}{1 + 5.46\theta} \tag{4.3}$$

The correlations given by Eqs. 4.2 and 4.3 have been found to be in good agreement with experimental data in several earlier studies [98, 99]. Although, the direct applicability of these equations to our system is not expected due to the inherent polydispersity of vesicle dispersion and the fibrous geometry of the deposition substrate, these equations provide us a good orientation for analyzing the results.

4.4 Results and Discussion

4.4.1 Applicability of Helmholtz-Smoluchowski equation to fiber plugs

As established in Chapter 3, the streaming potentials measured on single fiber plugs deviates from that on uniform capillaries. However, the linear dependence of streaming potential on applied pressure difference should still hold. This allows us to estimate the so-called “apparent

zeta potential" (ζ_{app}) of the fibers. It is found that the streaming potentials of fiber plugs formed by both cotton as well as viscose fibers vary linearly with pressure difference (Fig. 4.2(B)). In order to maintain the consistency of streaming potential measurements across experiments, fiber mass and difference in applied pressure difference levels were kept fixed at 1.5 g and 100 mbar ($P_{vacuum1}$ = 200 mbar, $P_{vacuum2}$ = 100 mbar), respectively. Under these conditions, the apparent zeta potentials of bare viscose and cotton fibers, based on Eq. 4.1, are found to be -20 mV and -23 mV, respectively.

4.4.2 Establishing intact deposition of vesicles

The intact deposition of DEEDMAC and WE15 vesicles on anionic cellulose surfaces is ascertained via two different experimental approaches, namely, streaming potential measurements as well as direct visualization via fluorescence microscopy.

4.4.2.1 Via streaming potential measurements

In order to ascertain the final state of esterquat vesicles after deposition, theoretical profiles of substrate apparent zeta potential variation with vesicle deposition are plotted for the two possible cases, namely, intact vesicle deposition (SVL formation) and vesicle disintegration (SLB formation), and compared with experimental results. In the possible case of intact vesicle deposition, the Eqs. 4.2 and 4.3 can be used to plot the theoretical substrate apparent zeta potential variation with surface coverage for deposition of monodisperse spherical particles having the same zeta potential as the esterquat vesicles (ζ_P = +60 mV) on a flat surface having the same zeta potential as viscose fibers (ζ_O = -20 mV) (see solid line in Fig. 4.4(A)). The saturating shape of the theoretical streaming potential profile is characteristic of particle-covered flat surfaces [96].

In cases where deposited vesicles disintegrate to form SLBs, substrate streaming potentials have been observed to change rapidly at surface coverage values corresponding to critical vesicular coverage ($\theta_{critical}$)[33]. The rapid change ensues because when vesicles rupture, the number of lipid molecules contained inside already deposited vesicles is typically comparable to or more than the number of molecules required for full bilayer coverage. Hence, the entire surface is covered by a bilayer with very little or no additional mass deposition. Although a model describing the streaming potential profile in such cases is so far not available, a schematic depicting the rapid change at a typical critical vesicular coverage (for example, $\theta_{critical}$ = 0.1) can be plotted (see dotted line in Fig. 4.4(A)). For plotting the schematic, it is assumed that the profile remains the same as for intact vesicle deposition at surface coverages below critical, and after SLB formation, once the entire surface is covered by lipid bilayers, the substrate zeta potential becomes equal to that of vesicles in the bulk liquid.

From the above discussion, it is evident that the profiles of substrate streaming potential variation with vesicle deposition are distinctly different in the two possible cases of SVL and SLB formation, and hence, a comparison of the experimental results with theoretical profiles would help us identify the case in our study. The theoretical profile has been obtained only for deposition on flat solid surfaces, however, as the radius of the fibers is much larger than the vesicle diameter it can be assumed to apply to our case. Furthermore, as the correlations given by Eqs. 4.2 and 4.3

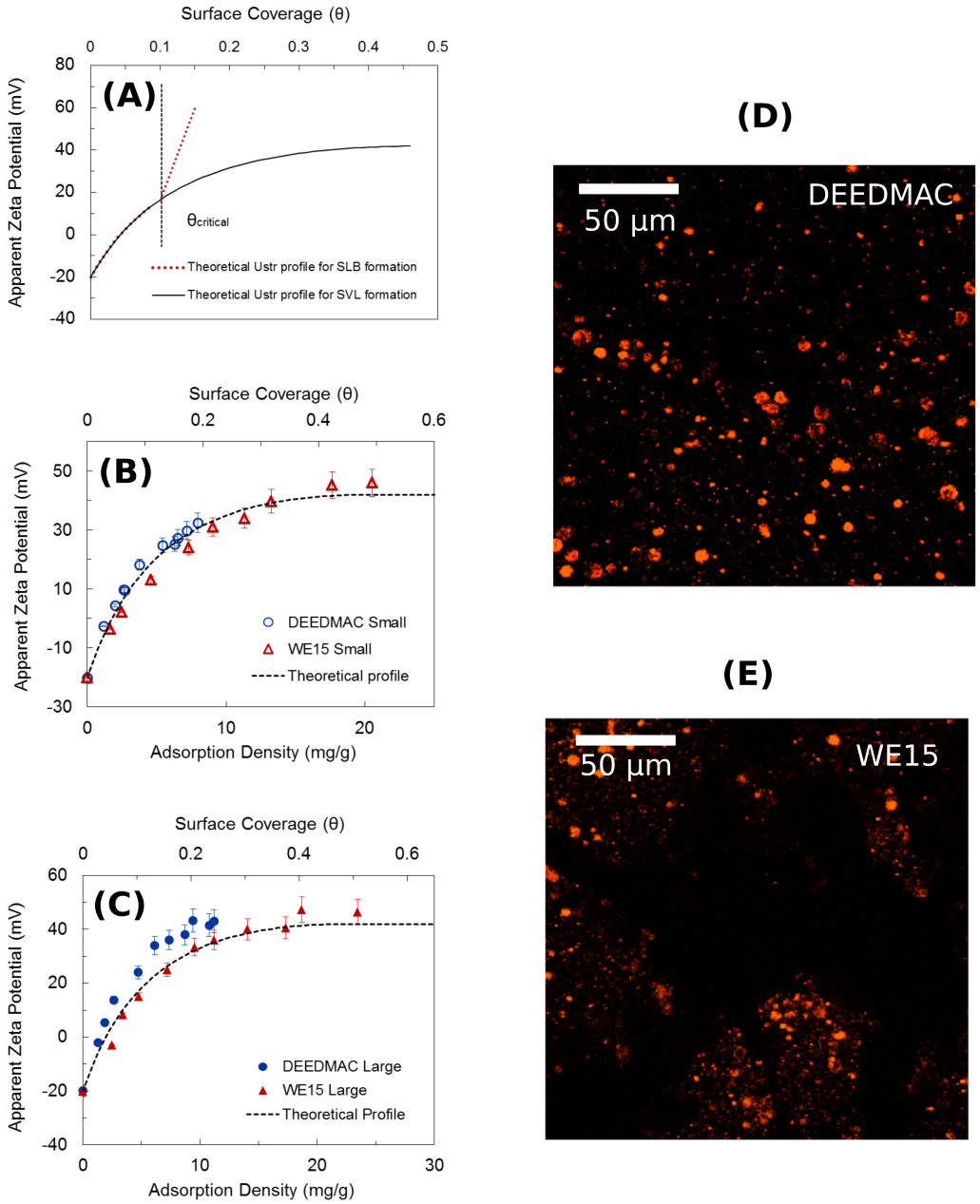

Figure 4.4.: (A) Theoretical apparent zeta potential profile for SVL formation (solid line) and schematic profile for SLB formation (dotted line). Experimental variation of viscose fiber apparent zeta potential with adsorption densities (mg esterquat per gram fiber) and comparison with the theoretical solution for SVL formation of large vesicles (B) and small vesicles (C). Note: Experimental data points are represented as apparent zeta potential (mV) vs. adsorption density (mg/g), whereas the theoretical solution for SVL formation is represented as apparent zeta potential (mV) vs. vesicle surface coverage. Intact DEEDMAC (D) and WE15 (E) vesicles visualized via fluorescence microscopy after deposition on the external surface of a cellulose fiber membrane.

are applicable only for flat surfaces, viscose fibers being smoother and more consistent in terms of shape than cotton fibers were chosen for these measurements.

A problem faced in the experiments was the impracticality of vesicular surface coverage estimation due to non-idealities such as non-circular fiber cross-sections, angular vesicle shapes, and high size polydispersity. Therefore, for the experimental profile, we substitute vesicle surface coverages by adsorption densities, i.e. the mass of esterquat deposited per unit fiber mass, which is quantifiable. Additionally, as adsorption densities are intuitively proportional to actual surface coverages they can be expected to capture the same behavior.

The experiments confirm the variation of viscose fiber streaming potentials in the form of characteristic saturating curves for deposition of both large and small vesicles. In fact, a good agreement between experimental data and the theoretical solution for SVL formation is obtained upon scaling the x-axes, as shown in Fig. 4.4(B) and (C). Streaming potential results thus, strongly support the idea that both DEEDMAC and WE15 vesicles deposit as intact entities on cellulose fibers forming supported vesicular layers.

4.4.2.2 Via fluorescence microscopy

The cellulose fiber membrane (Sartorius FT-3-127-090) equilibrated with fluorescently labelled large DEEDMAC and WE15 vesicle dispersions is visualized using the Nikon Eclipse-Ti fluorescence microscope as shown in Fig. 4.4(E) and (F), respectively. The adsorbed layer formed on the cellulose fibers at the surface of the cellulose fiber membrane confirms that both DEEDMAC and WE15 vesicles deposit as intact entities on cellulose surfaces.

Although the direct visualization of deposited vesicles appears sufficient to establish deposition as intact vesicles, coupling it with streaming potential measurements helps ascertain that vesicles exist as intact entities in the entire range of deposition and not just below some critical surface coverage. Additionally, the saturating streaming potential profile obtained with small vesicles confirms that they too deposit as intact entities which would not have been visualized via fluorescence microscopy. It is inferred that the reason underlying intact deposition of esterquat vesicles is the existent energy barrier to vesicle rupture being higher than the maximum interaction energy reachable during deposition [100]. This is not surprising, as the lipid bilayers constituting esterquat vesicles exist in relatively stable crystalline solid-gel and liquid-crystalline phases, respectively, which are difficult to rupture during adsorption [101].

4.4.3 Vesicle deposition on single viscose fibers (smooth and uniformly shaped)

Equilibrium adsorption densities obtained by treating viscose fibers with the vesicle dispersions are plotted against initial bulk esterquat concentrations, as shown in Fig. 4.5(A) and (B) for the large and small vesicles, respectively. The hypothetical adsorption density values that would be attained in case of complete vesicle deposition are plotted in the same figure as dotted straight lines.

4.4.3.1 Deposition of angular shaped DEEDMAC vesicles

The following are the main observations from Fig. 4.5 about the deposition of large and small DEEDMAC vesicles on viscose fibers,: (i) only moderate fractions of available DEEDMAC mass are deposited; (ii) adsorption density values increase gradually with initial concentration; (iii)

the maximum adsorption density attained with deposition of large vesicles is marginally higher than that with small vesicles.

As DEEDMAC vesicles deposit as intact entities on cellulose surfaces, the process can be treated similar to deposition of solid particles, described by the random sequential adsorption (RSA) model [102]. The basic RSA model states that particles that get immobilized upon deposition, and deposition proceeds until all possible pathways of attachment of unadsorbed particles to the substrate are blocked, which in the case of monodisperse particles on flat surfaces results in a maximum surface coverage of 0.547 [92]. The outcome is however significantly different when particles are polydisperse, like in our case, as particle-sizes affect both the transport and attachment of particles to the substrate [103].

A hypothesis is hereby proposed along the lines of the RSA model to provide a qualitative explanation for the deposition behavior of DEEDMAC vesicles on viscose fibers. Deposition is considered a 3-step process [91] involving: (i) transport of particles from the bulk to the vicinity of the interface, (ii) formation of an intimate contact with the interface, and (iii) attachment or no attachment depending upon available or blocked state of the surface. When the particles are monodisperse, equilibrium is not affected by the particle transport step, as all entities being transported to the adsorbent surface are identical. However, if the particle dispersion is polydisperse, the particle transport step plays a differentiating role.

In our deposition experiments, as the fibers are equilibrated with the vesicle dispersions by mildly agitating them on a shaker, the transport of vesicles is expected to occur via a combination of diffusive and convective processes, wherein small vesicles would transport faster than larger ones due to higher diffusivities and lower inertial effects [92]. Thus, the surface would be preferentially occupied by smaller vesicles from the dispersion. Deposition would proceed analogous to the RSA model and stop when the surface is occupied in such a way that the attachment of remaining vesicles to the surface is blocked. The high polydispersity of vesicle dispersions would enable a small surface deposition of small vesicles to block the entire surface for remaining unadsorbed vesicles [104]. Thus, at equilibrium, only a fraction of the vesicles, constituting mostly of smaller entities from the initial polydisperse batch would be deposited, as observed in the experiments. The deposition mechanism, as described above, is represented schematically on Fig. 4.6(A).

The validity of the proposed hypothesis is confirmed by investigating the effect of presence of additional small vesicles on the deposition behavior of the large vesicle dispersion. This is done by equilibrating a mixture of large and small vesicle dispersions (5:1 by mass) with viscose fibers, and comparing resultant adsorption densities with those obtained initially, as shown in Fig. 4.5(C). It is observed that the presence of additional small vesicles results in remarkable reductions in adsorption density values. This is in agreement with our expectation based on the hypothesis that the presence of new small vesicles would result in an enhanced blocking effect preventing the deposition of a larger proportion of vesicles. The results thus support the proposed hypothesis for the deposition mechanism of polydisperse vesicles on viscose fibers.

Adsorption densities increase gradually with increasing initial concentrations due to the increased population of vesicles with similar sizes which leads to a higher number of vesicles being deposited before the surface is blocked. It is however found that the overall proportion

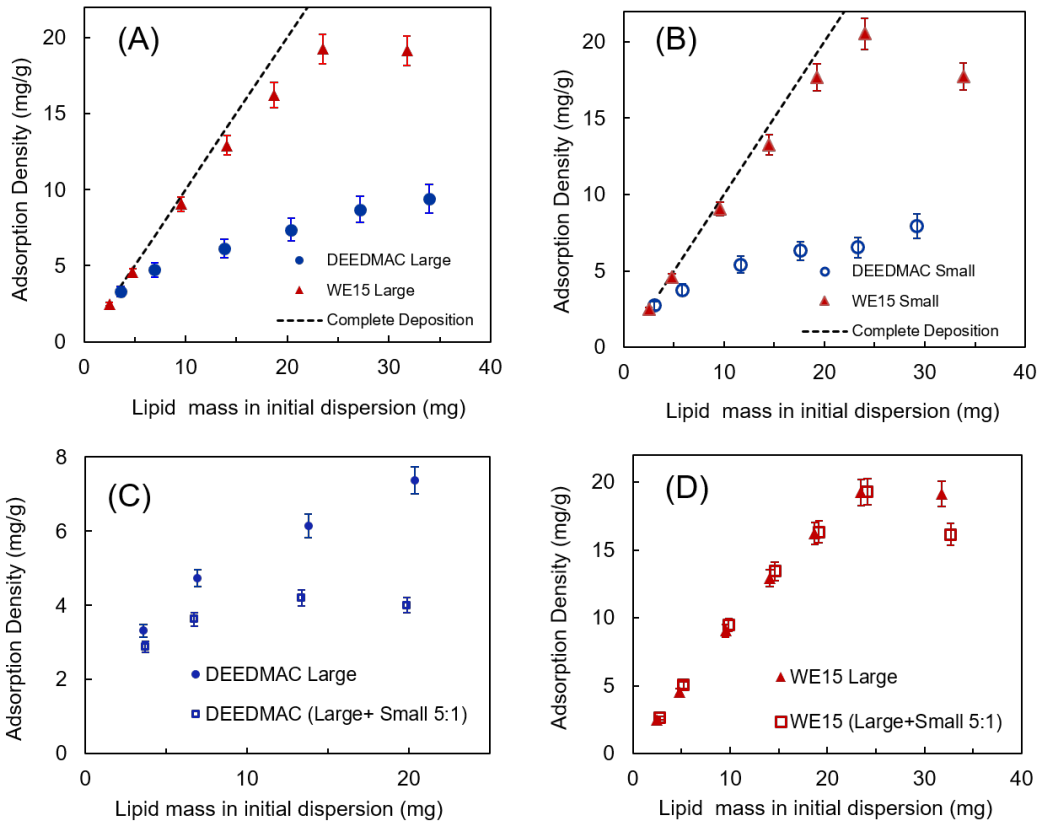

Figure 4.5.: Adsorption densities obtained by deposition of large (A) and small (B) DEEDMAC and WE15 vesicles on viscose fibers. Effect of presence of additional small vesicles on adsorption densities of large DEEDMAC (C) and WE15 (D) vesicles.

of available DEEDMAC mass being deposited continues to decrease with increasing initial concentration. Additionally, it is seen that the variation of adsorption densities of both large and small vesicles with initial concentrations follows similar trends, thus reassuring that both the deposition processes are governed by the same mechanism.

Another significant observation from Fig. 4.5(A) is that the maximum adsorption density obtained with large vesicles is only marginally higher than that obtained with small vesicles. Smaller particles, owing to higher specific surface areas, typically require less mass than larger particles to cover a certain surface, and this is expected to be the primary factor behind the lower adsorption density of small vesicles. However, other factors such as higher DEEDMAC density in microfluidized vesicles, and physical attributes of the fibers such as non-circular cross-sections, which allow smaller vesicles to access larger substrate areas, reduce this difference significantly.

4.4.3.2 Deposition of round shaped WE15 vesicles

The deposition behavior of WE15 vesicles is found to be significantly different from that of DEEDMAC vesicles, where (i) nearly all the available vesicles in the dispersion are deposited until a certain maximum deposition level is attained (see Fig. 4.5(A) and (B)), and (ii) the presence of additional small vesicles has no significant effect on equilibrium adsorption densities of the large vesicle dispersion (see Fig. 4.5(D)).

It is thus evident that the deposition mechanism on viscose fibers as established for DEEDMAC vesicles is not applicable for deposition of WE15 vesicles. However, as both the large and small WE15 vesicle dispersions are significantly polydisperse (see Table NA), the smaller WE15 vesicles in starting dispersions would certainly transport faster and attach to the substrate earlier than the larger ones, just as in the case of DEEDMAC vesicles. The observed contrasting behavior should therefore result from the way deposited WE15 vesicles interact with new incoming vesicles, which apparently leads to a mechanism wherein an early deposition of small vesicles does not block the attachment of larger unadsorbed vesicles to the substrate.

From the existing knowledge of deposition mechanisms in other colloidal systems such as proteins [105], it is understood that one possible reason behind such a deposition behavior could be the existence of lateral mobility in surface-bound WE15 vesicles. In such a case, deposition would proceed with deposited vesicles moving on the surface to make way for new incoming vesicles (as shown schematically in Fig. 4.6(B)), thus allowing complete deposition until the entire surface is occupied. However, if such a mechanism is responsible for the observed deposition behavior, the maximum surface coverages attained by deposition of WE15 vesicles should be substantially higher than that attained in the case of immobilized deposition. The same is supported by the apparent zeta potential profiles for DEEDMAC and WE15 vesicle deposition as shown in Fig. 4.4(E) and (F). Assuming that the surface coverage increases with adsorption density, it could be identified that the surface coverage obtained with WE15 vesicles deposition is higher than obtained with DEEDMAC vesicles.

Although the profiles of apparent zeta potential variation for DEEDMAC and WE15 vesicle deposition are very similar in the initial stages, with both the profiles reaching saturation at adjoining adsorption density values, the extent to which the saturation regime extends is significantly higher for WE15 vesicles as compared to that for DEEDMAC vesicles. A comparison of the experimental profiles clearly indicates that the maximum surface coverage attained by deposition of WE15 vesicles is considerably higher than that attained with DEEDMAC vesicles for both large and small vesicles. Thus, the hypothesis that the deposition of WE15 vesicles on viscose fibers is governed by a surface mobility driven deposition mechanism is supported by the results of both, the equilibrium deposition results as well as the streaming potential measurements.

4.4.4 Vesicle deposition on rough cotton fibers

Equilibrium adsorption densities obtained by treatment of cotton fibers with dispersions of large and small esterquat vesicles are plotted against initial bulk concentrations in Fig. 4.5(A) and (B), respectively. It is seen that experimental adsorption densities of both DEEDMAC and WE15 vesicles coincide with theoretical values for complete deposition up to a certain level and do not increase appreciably thereafter. The observation signifies that all vesicles available in the dispersion are deposited on cotton fibers until a certain maximum level of deposition is reached. This is in striking contrast with the behavior on viscose fibers where only fractions of available vesicles are deposited, and it is established that deposition is controlled by the blocking effect resulting from an early deposition of smaller vesicles from the polydisperse batch. In the case of cotton fibers, it is, however, imminent that such a blocking effect does not play an observable role.

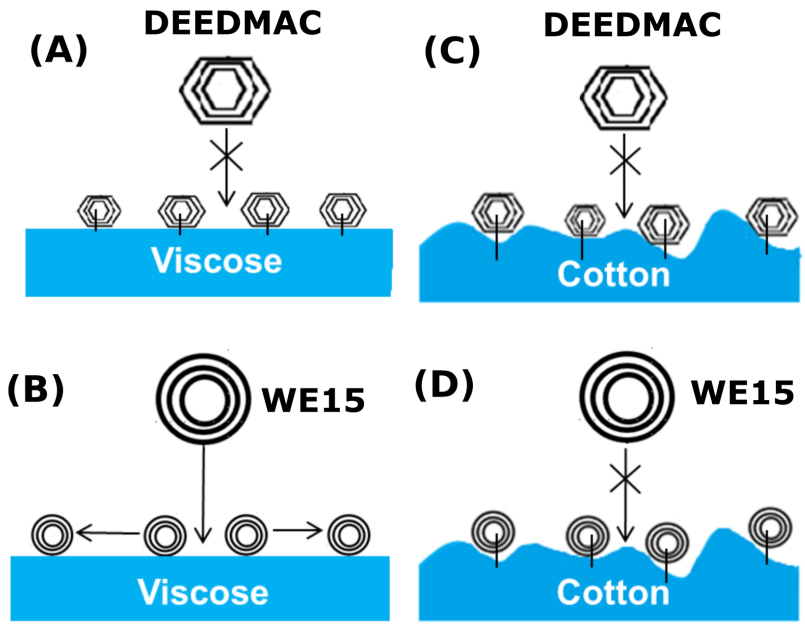

Figure 4.6.: Schematic representation of the deposition mechanisms of DEEDMAC and WE15 vesicles on viscose (smooth) and cotton (rough) fibers. DEEDMAC vesicles are shown as hexagons to illustrate their non-spherical angular shapes and presence of sharp edges, whereas WE15 vesicles are smoothly shaped and round, and are therefore represented as circles.

As cotton fibers are fundamentally different from viscose fibers only in terms of their physical form, a consideration of the effect of fiber morphology helps us understand the differences in deposition behavior. As viscose fibers are smooth and uniformly shaped, a low surface coverage of small vesicles is able to efficiently obstruct and bar the attachment of larger vesicles to the surface. Cotton fibers are however rough and irregularly shaped where deposited vesicles would partially penetrate into local holes on the fiber surface such that despite an early deposition of small vesicles, new incoming vesicles would still find a segment of the fiber which is accessible and can be attached to. Therefore, deposition continues with complete pick-up until a certain stage is reached whereafter the substrate is no longer accessible.

As the deposition of both the vesicle types proceeds with complete pick-up, and leads to deposition of comparable lipid masses, it appears that both the vesicles are deposited on cotton fibers via the same underlying mechanism. This would imply that the behavior of deposited WE15 vesicles on cotton fibers is identical to that of DEEDMAC vesicles with both of them being immobilized upon deposition as shown schematically in Fig. 4.6(C) and (D).

A comparison of the variation of apparent zeta potential of cotton fibers with DEEDMAC and WE15 vesicle deposition (Fig. (D)) provides more evidence to support this idea. The linear variation of cotton fiber apparent zeta potentials with adsorption densities as opposed to the saturating profile obtained with viscose fibers is a result of the difference in morphologies of the two fibers [12]. The shape of the streaming potential profile is determined by local electrolyte flow velocities in electric double layers along the surfaces of deposited colloids and the remaining bare substrate [98]. Although saturation streaming potential profiles are pronounced on smooth surfaces, if the substrate is rough and irregularly shaped (cotton fibers) such that deposited

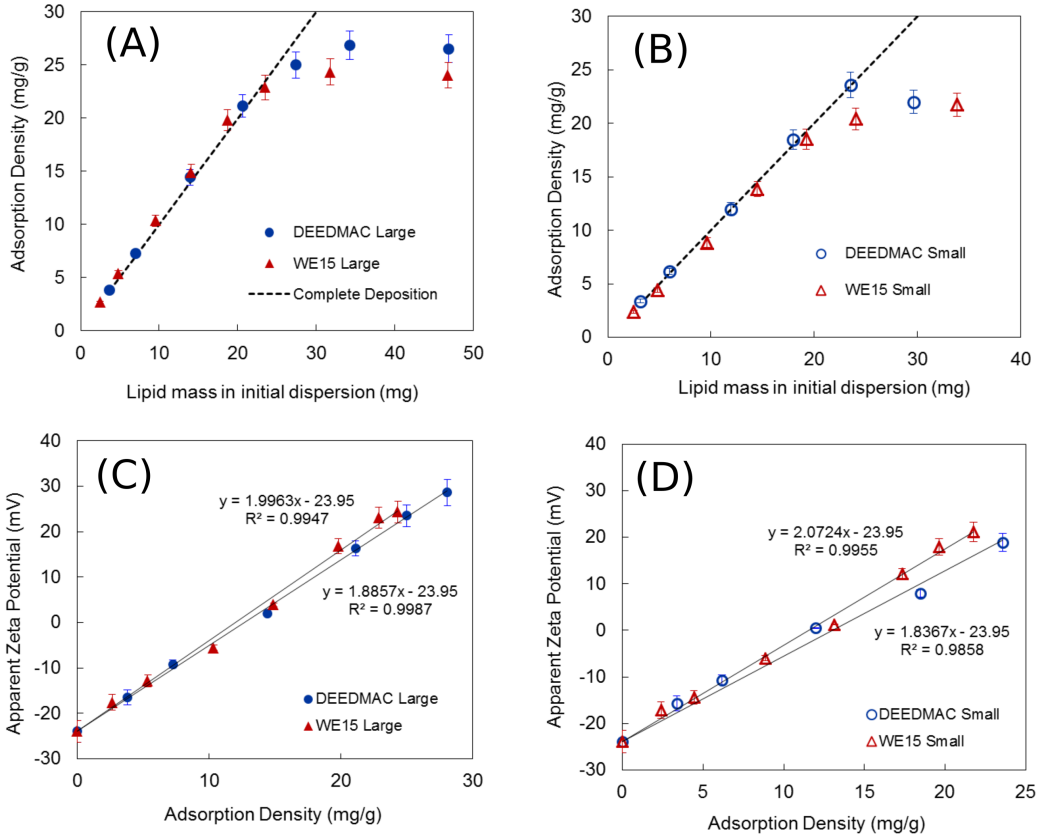

Figure 4.7.: Adsorption densities obtained by deposition of large (A) and small (microfluidized) (B) DEEDMAC and WE15 vesicles on cotton fibers. Variation of apparent zeta potential of cotton fibers with deposition of large (C) and small (D) vesicles

vesicles are partially penetrating into local holes on the surface, a saturating profile might not be observed. The experimentally observed linear profile on cotton fibers confirms the same [12].

It is observed from Fig. 4.5(D) that the variation of cotton fiber apparent zeta potentials with adsorption densities of the two vesicle types follows very similar trends indicating the attainment of similar surface coverages, and thus pointing towards the existence of the same underlying mechanism. Vesicle size is again found to not play a major differentiating role as similar results are obtained with both large and small vesicles.

The imminent surface immobility of deposited vesicles on rough surfaces (cotton fibers) can be explained by extending the same concept of vesicle surface mobility as employed in the case of smooth surfaces (viscose fibers). The rough morphology of cotton fibers would lead to much higher vesicle-substrate contact areas, and hence much higher vesicle-substrate adhesion forces for both the vesicle types. As a result the energy barrier to surface mobility of the vesicles would be significantly high, irrespective of vesicle shape, leading to surface immobility of both DEEDMAC and WE15 vesicles on cotton fibers. This would therefore lead to similar deposition mechanisms of both the vesicles on cotton fibers, as observed in the experiments.

4.5 Summary

In this Chapter, a systematic experimental investigation of the deposition of cationic vesicles on natural and regenerated cellulose fibers having rough and smooth surfaces, respectively, is presented. Using streaming potential measurements as the primary probing technique, it is established that both large and small vesicles deposit as intact entities on cellulose surfaces. The existence of intact deposited vesicles on cellulose surfaces is also verified by confocal fluorescence microscopy. Experiments show that the mechanism of cationic vesicle deposition is highly dependent on vesicle size, vesicle shape, polydispersity, and substrate roughness. Vesicle deposition behavior on smooth surfaces (viscose fibers) is governed by the contrasting surface mobility characteristics of the two vesicle types with smoothly-shaped and round WE15 vesicles being capable of moving, and non-spherical and sharp-edged DEEDMAC vesicles being immobilized upon deposition. For deposition on rough surfaces (cotton fibers), the surface mobility of both DEEDMAC and WE15 vesicles is suppressed, and hence similar deposition behavior is observed for both the vesicle types.

5 Deposition of cationic vesicles on porous cotton yarns

In this chapter, the experimental study investigating the deposition of cationic vesicles on anionic porous cotton yarns is described. The deposition process is investigated by combining two experimental techniques, namely, spectrophotometric measurement of the adsorption density of deposited vesicles, and determination of apparent zeta potential of cotton yarns via streaming potential measurements. Under the employed conditions, measured cotton yarn apparent zeta potentials are selectively sensitive to the external yarn surfaces. Thus, streaming potential measurements could be used to distinguish between deposition on external and internal yarn surfaces. The phase behavior of lipid bilayers constituting the vesicles, and bulk electrical conductivity are found to be important factors influencing the distribution of deposited vesicles. The effect of above factors is explained in terms of their effect on deposition kinetics and electrostatic interactions which influence the process significantly.

This chapter is based on the article, *Electrokinetic investigation of fabric softener vesicle deposition on porous cotton fabrics*, by Kumar et al. (2018) published in the Journal of Colloid and Interface Science.

5.1 Background of vesicle deposition on porous substrates

In conventional applications of vesicle-based formulations such as fabric softening and hair conditioning, the mode of action involves deposition of active ingredient-loaded vesicles onto the solid substrate [106]. The deposition process is typically driven by attractive vesicle-substrate electrostatic interactions, and results in the formation of a monolayer of the vesicles on the oppositely charged solid surface. The deposition of esterquant vesicles on single cellulose fibers is investigated and the mechanism of the deposition process is elucidated in Chapter 4.

In real life applications, the substrates to be treated usually do not exist as flat surfaces, instead, they occur as substrates with porous structures such as textile, paper, hair, and the human skin (see Fig. 1.2). On such substrates, the vesicles could not only deposit on the substrate's external surfaces but also on its internal surfaces. Furthermore, depending upon the intended purpose of the formulation, desired results are obtained either when vesicle deposition is confined to external substrate surfaces, or when vesicles permeate deeply into the porous substrate so that deposition is homogeneously distributed throughout the substrate. In some cases, a combination of deposition on both, internal and external substrate surfaces, produces optimal performance.

In a conventional fabric conditioning application, a superior and easily perceptible softening effect is produced when deposition is localized on the external surfaces of treated textiles [107]. On the other hand, deposition on internal surfaces of textiles produces a sense of bulk softness and loft, which could also be desirable. In other applications, such as antimicrobial treatment of textiles, a homogeneous distribution of active ingredients throughout the textile is preferable

[108]. Therefore, in order to develop formulations whose properties are tailored to provide optimal performance, it is important to have a good understanding of the main factors governing the post-treatment distribution of deposition across the porous substrate.

Depending upon the location of deposition sites, colloidal deposition on porous substrates could be classified into : (i) deposition on external substrate surfaces, and (ii) deposition on internal substrate surfaces. When the porous substrate is completely immersed inside a colloidal dispersion, the external substrate surfaces are directly accessible to the colloids in the bulk dispersion. Deposition on external surfaces could thus occur simply when a colloid from the bulk dispersion contacts an unoccupied deposition site on the substrate. The deposition of colloids on internal substrate surfaces is, however, a complex two-step process. For deposition on internal surfaces to occur, the colloids should first permeate from the bulk dispersion to the internally located deposition site through the porous structure of the substrate.

As the deposition of colloids on internal surfaces of a porous substrate is related to the characteristics of colloidal permeation into porous substrates, it is useful to consider the literature in this area. In the absence of flow fields, the permeation of colloids into saturated porous substrates occurs predominantly via diffusion [109]. In earlier works investigating the diffusion of colloids through saturated porous media, it has been reported that the dynamics of diffusion through pores is much slower that the characteristic Fickian dynamics in bulk dispersions [110]. The slower diffusion through pores is attributed to a range of factors including pore-scale hydrodynamic hindrances, physical barriers, and colloid-pore electrostatic interactions [111, 112]. Lieleg et. al. [113] in their work dealing with colloidal diffusion in porous extra-cellular matrices showed that repulsive electrostatic interactions between similarly charged pores and colloids could slow down and even completely block diffusive colloidal transport. Other works have shown that the extent of hindrance to colloidal diffusion is dependent on both pore sizes as well as the geometry of pores [114, 115].

Although the diffusive transport of colloids through saturated porous media has been a subject of earlier investigations, so far very few works considered simultaneous diffusive permeation and deposition of colloids on porous substrates. The main reason being that it is very difficult to characterize deposition on the internal surfaces of a porous substrate using conventional methods. Although techniques like confocal and multiphoton microscopy have been implemented to observe deposition inside a porous substrate [6–8, 116], these techniques are highly restrictive in terms of the properties of usable substrates. Additionally, the quantification of deposition levels is not straightforward.

In this work, the everyday fabric softening process which is a typical example of deposition of cationic vesicles on anionic porous textile substrates is taken up as the main subject of investigation. In an earlier work on this topic, Venzmer [106] used fluorescence microscopy to identify the effect of vesicle size on the location of deposited vesicles on treated cotton yarns (see Fig. 5.1). It was observed that the deposition of large vesicles remains localized in the region near the periphery of yarns, whereas the deposition of small vesicles is distributed almost homogeneously throughout the yarn cross-sections. Although this work provided important primary insights into the fabric softening process, the effect of other important factors such as type of lipid, and electrical conductivity of the bulk liquid could not be elucidated.

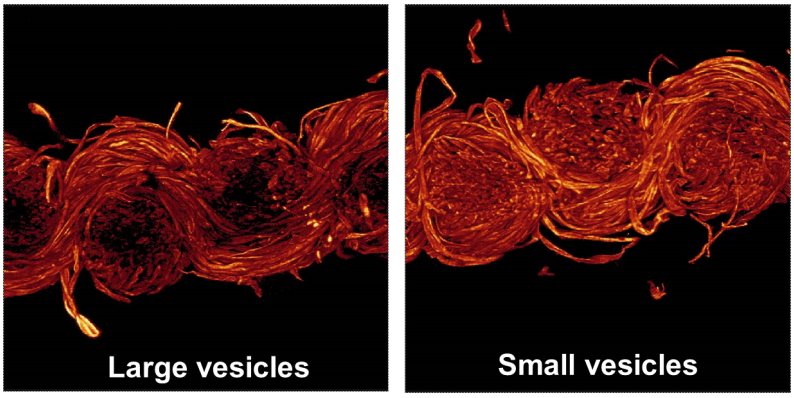

Figure 5.1.: Fluorescence microscopy images showing the distribution of fabric softening vesicles deposited across cotton yarn cross-sections. As is evident, the deposition of large solid-gel vesicles is localized near the yarn periphery, whereas the deposition of small liquid-crystalline vesicles in homogeneously distributed across the yarn cross-section. This figure has been reprinted with permission from Venzmer et. al. [107].

The present study improves upon the earlier work of Venzmer [106] and uses new streaming potential based techniques to obtain further insights into the factors governing the deposition of fabric softener vesicles. The earlier limitations are overcome by characterizing the equilibrium vesicle deposition using an experimental methodology which combines streaming potential measurements and measurements of bulk lipid concentrations via UV-Vis spectroscopy. Pre- and post-treatment measurements of bulk lipid concentrations are used to obtain a measure of the total lipid mass of deposited vesicles. The apparent zeta potential values which are obtained via streaming potential measurements are used to distinguish between deposition on external and internal substrate surfaces.

The basic theory underlying streaming potential measurements has been outlined in Chapter 3. In this chapter. the fundamental theory is applied to the case of plugs of porous cotton yarns. Furthermore, streaming potential measurements could also be used to carry out an in-situ investigation of vesicle deposition kinetics as later described in this chapter. A similar experimental methodology was implemented by Hubbe et. al. [117, 118] to study the deposition of polyelectrolytes on mesoporous silica beads.

5.2 Materials and Methods

5.2.1 Materials

The preparation and properties of DEEDMAC and WE15 vesicles used for the investigations are described in Chapter 2. Only the small vesicles were used for the experiments, in order to focus on other important factors such as vesicle lipid bilayer phase behavior and bulk electric conductivity. The porous cotton yarns used as deposition substrate for the investigations are also described in Chapter 2.

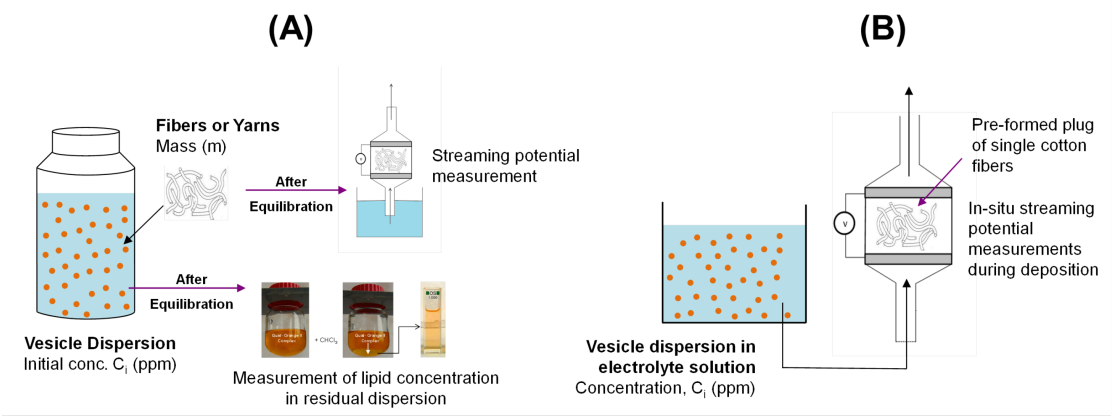

Figure 5.2.: Schematic representation of the experimental methodology for (A) characterization of equilibrium vesicle deposition on single cotton fibers and cotton yarns, and (B) in-situ investigation of vesicle deposition kinetics on single cotton fibers.

5.2.2 Determination of bulk lipid concentrations

The UV-Vis spectroscopy based method used to quantitatively determine the mass concentration of lipids in bulk vesicle dispersions has already been described in Chapter 4. In the deposition experiments, a measurement of lipid mass depletion in bulk liquid is used to estimate the lipid mass in vesicles deposited on the substrate.

5.2.3 Streaming potential measurements

Streaming potential measurements on single cotton fibers and cotton yarns were carried out using the Fiber Potential Analyzer (FPA) from AFG Analytic GmbH using the same approach as described in Section 4.2.3. The measurements involve packing a certain mass of the substrate inside the electrokinetic cell provided in the device to form a plug. An electrolyte of fixed conductivity (1 mS/cm) is thereafter flown through the plug under a certain applied pressure difference. A detailed description of the functioning of the device has been provided in Chapter 4. The apparent zeta potential of the substrate is estimated from measured streaming potentials using the Helmholtz-Smoluchowski equation. For measurements on single cotton fibers, all the fiber surfaces contribute equally to the measured apparent zeta potential. However, for measurements on porous cotton yarns, the measured apparent zeta potential is predominantly sensitive only to the external surfaces of cotton yarns.This is demonstrated with the help of a theoretical analysis in Section 5.3.2.

5.2.4 Deposition experiments

The deposition experiments were carried out using two different schemes, as shown in Fig. 5.2(A) and (B), respectively. The first experimental scheme is aimed at characterizing the equilibrium deposition of vesicles. The second experimental scheme is aimed at contrasting the in-situ deposition kinetics of the DEEDMAC and WE15 vesicles on single cotton fibers. The kinetics of vesicle deposition play an important role in determining the final distribution of vesicles deposited on the porous substrate. It, therefore, forms an important part of these investigations described in this Chapter.

5.2.4.1 Equilibrium vesicle deposition

The experimental procedure implemented to investigate the equilibrium deposition of vesicles is shown schematically in Fig. 5.2(A). The experimental procedure followed to investigate equilibrium deposition has been described in Chapter 4 where only single cotton fibers were used as deposition substrate.

Milli-Q water was used for the dilution of vesicle dispersions and for pre-soaking the substrates before deposition. For the deposition experiments involving porous substrates, Milli-Q water was used either unmodified (bulk electrical conductivity $\approx 5 \times 10^{-5}$ mS/cm), or after adding a certain mass of sodium chloride to increase the bulk electrical conductivity to 1 mS/cm. By doing so, we can carry out deposition experiments at two different levels of bulk electrical conductivity. This enables us to investigate the effect of electrostatic interactions on the process. As the electrical conductivity of tap water is typically high (0.5 mS/cm), the experiments carried out at high bulk conductivity provide a glimpse of what happens in real applications.

The above-described experimental protocol is similar to the treatment of textiles by fabric softeners in real applications. In washing machines, the fabric softener is typically diluted to a concentration of around 250 ppm before being added in the last rinse cycle to a batch of textiles. In our experiments, we have, however, varied the initial concentration in the range 0-2000 ppm.

5.2.4.2 In-situ investigation of vesicle deposition kinetics on single cotton fibers

A simple experiment, as shown schematically in Fig. 5.2(B), was implemented to obtain insights into the deposition kinetics of DEEDMAC and WE15 vesicles on single cotton fibers. A certain mass of single cotton fibers (1.5 g) was packed inside the electrokinetic cell provided in the FPA device to form a fiber plug. Thereafter, instead of flowing a pure electrolyte solution through the fiber plug as done in typical streaming potential measurements, a dilute dispersion of vesicles in the same electrolyte solution is used. The concentration of the used vesicle dispersions was 20 ppm.

This enables us to measure the apparent zeta potentials of cotton fibers in-situ while vesicle deposition occurs on the fibers. A comparison of the rates at which apparent zeta potentials of cotton fibers increase is used to compare the deposition kinetics of DEEDMAC and WE15 vesicles. The above experimental scheme ensures that the bulk colloidal concentration and the conditions of colloidal transport, are the same during the deposition of DEEDMAC and WE15 vesicles. Any observed difference in the deposition kinetics of the two vesicle types could be attributed to an inherent difference in vesicle properties. An understanding of the difference in deposition kinetics of the two vesicle types is helpful in explaining their contrasting deposition behavior on porous cotton yarns, and it is hence include in the present Chapter.

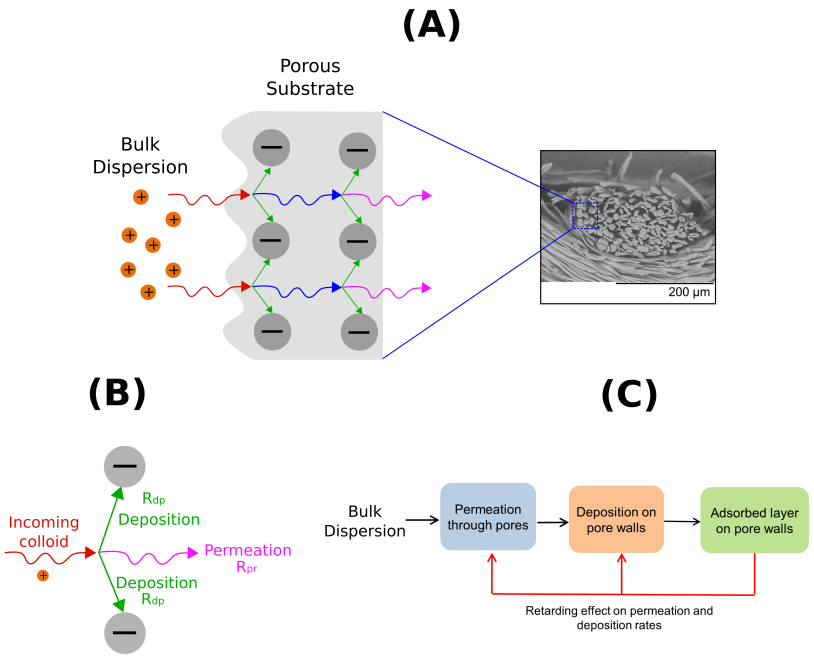

Figure 5.3.: (A) Schematic representation of the colloidal permeation and deposition mechanism on a sequence of pores, (B) Schematic diagram depicting colloidal permeation and deposition on a single pore, (C) Flow diagram depicting the influence of the adsorbed layer on the deposition and permeation rates

5.3 Theory

5.3.1 Qualitative model of permeation and deposition of colloids on porous substrates

In this section, we present a Qualitative model to describe the permeation and deposition of colloids on porous substrates. Let us consider the trajectory of a colloid as it permeates via diffusion from the bulk dispersion to an attachment site located inside a porous substrate, as shown schematically in Fig. 5.3(A). This trajectory could be treated as a sequence of pores labelled p_i, where $0 \leq i \leq n$. Here, p_0 corresponds to the pore-like geometry in the immediate external vicinity of the substrate, and p_n refers to the last pore in the sequence.

A colloid upon being transported into a pore could either be deposited on its confining surfaces, or be transported to the next pore in the sequence where the same decision is reiterated as shown schematically in Fig. 5.3(B). Let $p_{dp,i}$ be the probability that a colloid entering the i-th pore is deposited on its confining surfaces, and $p_{pr,i}$ be the probability that the colloid is not deposited, and is permeated to the next pore. If $R_{dp,i}$ and $R_{pr,i}$ are the rates of colloidal mass deposition and diffusive colloidal permeation in the i-th pore, respectively, $p_{dp,i}$ and $p_{pr,i}$ could be expressed as :

$$p_{dp,i} = \frac{R_{dp,i}}{R_{dp,i} + R_{pr,i}}, \; p_{pr,i} = \frac{R_{pr,i}}{R_{dp,i} + R_{pr,i}} \tag{5.1}$$

Using the above relationships for p_{dp_i} and p_{pr_i}, the probability that the deposition of a colloid occurs in the j-th pore of the sequence (P_j) could be expressed as :

$$\begin{aligned} P_j = p_{dp,j}\Pi_{i=0}^{j-1}p_{pr,i} &= \frac{R_{dp,j}}{R_{dp,j}+R_{pr,j}}\Pi_{i=0}^{j-1}\frac{R_{pr,i}}{R_{dp,i}+R_{pr,i}} \\ &= \frac{1}{1+\frac{R_{pr,j}}{R_{dp,j}}}\Pi_{i=0}^{j-1}\Big(\frac{1}{\frac{R_{dp,i}}{R_{pr,i}}+1}\Big) \end{aligned} \tag{5.2}$$

The objective of the above analysis is, however, not to estimate the probability of deposition in each pore of the substrate, but to understand how the deposited colloids are overall distributed into external and internal surfaces of the substrate. If we assume that $M_{\Delta t}$ is the colloidal mass deposited on the porous substrate during a short time interval Δt during which the colloidal deposition and permeation rates, $R_{dp,i}$ and $R_{pr,i}$, remain constant, the colloidal mass deposited on external surfaces of the porous substrate ($M_{0,\Delta t}$) could be expressed using Eq. 5.2 :

$$M_{0,\Delta t} = \Big(\frac{1}{1+\frac{R_{pr,0}}{R_{dp,0}}}\Big)M_{\Delta t} \tag{5.3}$$

where, $R_{dp,0}$ is the rate of deposition on external substrate surfaces, and $R_{pr,0}$ is the rate at which colloids permeate from the bulk dispersion to the inside of the porous substrate.

It follows from Eq. 5.3 that the extent of deposition on external substrate surfaces is related to the value of the ratio $\frac{R_{dp,o}}{R_{pr,o}}$. Deposition on external substrate surfaces would be greater at higher values of $\frac{R_{dp,o}}{R_{pr,o}}$ and vice-versa. The level of deposition attained on external substrate surfaces could also be treated as an indication of how the overall deposition is distributed on the porous substrate. Higher deposition levels on external substrate surfaces indicate that deposition is mostly localized near the substrate periphery. On the other hand, relatively lower deposition levels on external surfaces indicate that a larger proportion of deposition occurs on internal substrate surfaces, and deposition is more homogeneously distributed.

It should be, however, taken into account that the colloidal deposition and permeation rates vary during the course of the process since deposition levels on substrate surfaces increase leading to a variation of the ratio $\frac{R_{dp,o}}{R_{pr,o}}$. As the ratio $\frac{R_{dp,o}}{R_{pr,o}}$ varies with increasing deposition levels, the distribution of deposition into internal and external surfaces also varies simultaneously. Thus, on a particular porous substrate the final distribution of deposition is dependent on both: (i) the initial value of $\frac{R_{dp,0}}{R_{pr,0}}$ which is dependent on the properties of the colloidal dispersion and the porous substrate, and (ii) the variation of $\frac{R_{dp,0}}{R_{pr,0}}$ during the process which is influenced by the interaction of the deposited colloidal layer with free colloids. This has been depicted schematically on the flow diagram in Fig. 5.3(C). The reasons underlying the variation of the deposition and permeation rates, $R_{dp,0}$ and $R_{pr,0}$, is described below.

The deposition rate of colloids on solid surfaces is typically described using the Random Sequential Adsorption (RSA) model [119]. According to the RSA model, the deposition rate decreases with increasing levels of surface coverage on the substrate surface. Thus, $R_{dp,o}$ would be its maximum at the start of deposition when all the substrate surfaces are unoccupied. $R_{dp,o}$ would thereafter decrease gradually as the surface coverage on external surfaces increases, and eventually would go to zero when the external surface is completely saturated with deposited colloids [91]. Additionally, the rate of deposition could be different for different types of colloids. Furthermore, when the colloids and the substrate are electrically charged, the deposition rate could also be affected by electrostatic interactions.

Similarly, the rate of colloidal permeation into the porous substrate, $R_{pr,0}$, could also vary with increasing deposition levels on substrate surfaces. Such a variation results from the slowing down effect that deposited colloids have on diffusive permeation of free colloids. In the Introduction, it was established based on the findings of earlier works that the diffusive permeation of colloids into a porous substrate could be slowed down or blocked via several mechanisms. However, the blocking mechanism which is important when colloids are electrically charged results from the repulsive electrostatic interactions between deposited and free colloids. The magnitude of the electrostatic repulsion increases with increasing deposition levels, and thus results in a variation of $R_{pr,o}$ during the process. It can be thus concluded that $R_{pr,o}$ is highest at the start of the process, and decreases as the process proceeds.

The variations of both $R_{dp,o}$ and $R_{pr,o}$ during deposition are influenced by the presence of electrostatic interactions. However, these electrostatic interactions can be screened when deposition is carried out at higher bulk electrical conductivities. Although it is known that both, $R_{dp,0}$ and $R_{pr,0}$, decrease during the deposition process, the variation of the ratio $\frac{R_{dp,0}}{R_{pr,0}}$ during deposition at low and high bulk electrical conductivities is not well known. The experimental results provide insights into how deposition is distributed inside the substrate, and as a result insights could be drawn into the variation of the ratio $\frac{R_{dp,0}}{R_{pr,0}}$ during deposition. Furthermore, comparing the results obtained at low and high bulk electrical conductivity levels can be used to understand the role played by electrostatic interactions.

5.3.2 Theory of streaming potential measurements on porous yarns

The sample geometry during streaming potential measurements on single fiber plugs is shown schematically in Fig. 5.4(A) has been described in Chapter 3. The sample geometry is, however, even more complex when the measurements are carried out on plugs formed out of porous substrates, since the electrolyte flows through both inter-substrate as well as intra-substrate voids. The geometry of such plugs is generally described using the internal- and external- porosity parameters (ϕ_{ext} and ϕ_{int})[120]. The theoretical model described in Chapter 3, however, cannot be directly applied to the present bi-porous system due to the complex sample geometry. Therefore, there is a need for simplification.

Yaroshchuk et. al. [58] proposed an equation to estimate the streaming potential generated in simple forms of such bi-porous geometries (see Fig. 5.4(B)), as given below :

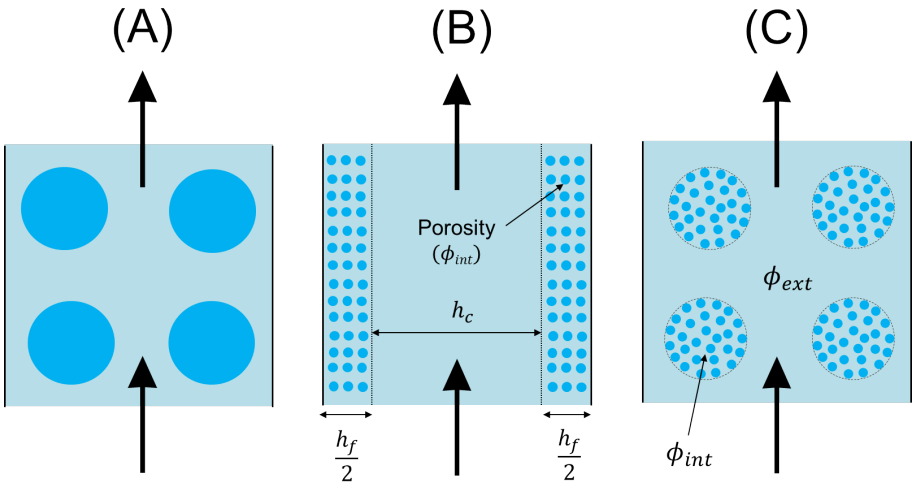

Figure 5.4.: Schematic representation of the plug configuration during streaming potential measurements on single fibers (A), model bi-porous substrate (B) and cotton yarns (C)

$$U_{str} = \frac{\epsilon \Delta P}{\mu \kappa} \frac{h_c \zeta_{ext} + h_f \phi_{int} \zeta_{int}}{h_c + h_f \phi_{int}} \tag{5.4}$$

where, h_c and h_f are the widths of the inter- and intra-substrate regions (see Fig. 7(B)), respectively, and together determine the external porosity as $\phi_{ext} = \frac{h_c}{h_c + h_f}$. ϕ_{int} is the internal porosity of the porous substrate. ζ_{ext} and ζ_{int} are the zeta potentials of external and internal substrate surfaces, respectively.

Eq. 5.4 could be rewritten in the following form :

$$U_{str} = \frac{\epsilon \Delta P \zeta_{ext}}{\mu \kappa} \frac{1 + (h_f/h_c)\phi_{int}(\zeta_{int}/\zeta_{ext})}{1 + (h_f/h_c)\phi_{int}} \tag{5.5}$$

where, the term $(h_f/h_c)\phi_{int}$ can be expressed as $(\frac{1}{\phi_{ext}} - 1)\phi_{int}$.

Under the conditions that : (i) the porous substrate has low internal porosity ($\phi_{int} \ll 1$), and (ii) the plug is formed by loosely packing the porous substrate such that $\frac{1}{\phi_{ext}} - 1 \ll 1$, the term $(h_f/h_c)\phi_{int} \ll 1$. Furthermore, given that the magnitudes of ζ_{int} and ζ_{ext} are comparable, Eq. (5.5) could be simplified as :

$$U_{str} \approx \frac{\epsilon}{\mu \kappa} \Delta P \zeta_{ext} \tag{5.6}$$

Under the conditions at which Eq. 5.6 is applicable, the electrolyte flow through inter-substrate voids is much larger than the flow through intra-substrate voids. The contribution of internal substrate surfaces to the generated streaming potential is hence much lower than that of the

external surfaces, and could be neglected. The streaming potential is therefore predominantly sensitive only to the zeta potential of external substrate surfaces.

In contrast to the simple geometry (Fig. 5.4(B)) considered in the above analysis, the plugs formed during measurements on cotton yarns are more complex, and are depicted schematically in Fig. 5.4(C). Although the plug geometry is more complex, the underlying phenomena are the same, and the relationship given by Eq. 5.6 should still be roughly applicable. The above-described configuration thus enables the independent determination of the zeta potentials of external substrate surfaces. Therefore, it could be used as an effective tool to investigate the characteristics of colloidal deposition on porous substrates as demonstrated in this work.

5.4 Results and Discussion

5.4.1 Deposition kinetics of vesicles on single cotton fibers

It has been postulated in Section 5.3.1 that the deposition kinetics of colloids plays a significant role in the determining their post-deposition distribution on porous substrates. It is therefore important to know how the deposition kinetics of the two vesicle types used in this study compare with each other. As this is expected to significantly effect deposition on the porous substrate, these results are included in the present Chapter and not in Chapter 4 which deals with deposition on single fibers.

The kinetics of deposition of colloids on solid surfaces, as described by the RSA model, depends on three main factors : (i) the rate of colloidal transport from the bulk liquid to the adsorption boundary layer at the solid-liquid interface, (ii) the blocking function which depends upon the existing state of the adsorbed colloidal layer on the solid surface, and (iii) the rate constant of colloidal adsorption which is an intrinsic property of the colloids and the substrate [91, 119].

It is difficult to obtain insights into the different factors governing the deposition kinetics of colloids via batch deposition experiments. In batch deposition experiments, the concentration of colloids in the bulk dispersion varies continuously, thus the transport rate of colloids from the bulk liquid to the solid-liquid interface varies throughout the experiment. Investigations via in-situ streaming potential measurements as described in Section 5.2.4.2, however, provide a possibility to overcome the above limitation [121, 122].

In this method, a dilute colloidal dispersion of fixed concentration is flown across the substrate. Thus, the bulk concentration of the incoming colloidal dispersion is the same throughout the deposition process. The liquid flow conditions across the fibers are maintained constant by keeping the applied pressure difference levels unchanged for different experiments. The measurement conditions are the same as described in our earlier work [26]. Therefore, the rate of transport of colloids from the bulk liquid to the solid-liquid interface, which in this case occurs via convection, can be kept constant.

It has been shown in Chapter 4 that the apparent zeta potentials of single cotton fibers vary linearly with vesicle adsorption density. Thus, the apparent zeta potential provides a good measure of the adsorption density of vesicles. The evolution of the apparent zeta potential of cotton fibers with deposition time could used to compare the deposition kinetics of DEEDMAC

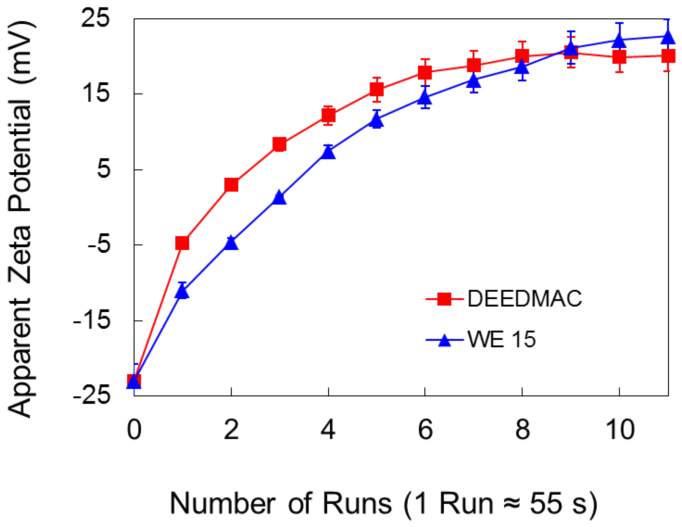

Figure 5.5.: Comparison of the deposition kinetics of DEEDMAC and WE15 vesicles on single cotton fibers via in-situ streaming potential measurements

and WE15 vesicles. Deposition time is measured in terms of the number of measurement runs, with each run lasting approximately 55 s.

The variation of the apparent zeta potential of single cotton fibers with deposition time is plotted in Fig. 5.5. It can be observed from Fig. 5.5 that the apparent zeta potential of cotton fibers evolve with time in the form of saturating profiles for both DEEDMAC and WE15 vesicles. This indicates that the deposition rate is the highest at start, slows down as an adsorbed layer forms on fiber surfaces, and reduces to zero upon when the fiber surfaces are completely occupied. The above observations are consistent with the postulates of the RSA model, and could be correlated with the variation of the blocking function during the process [119]. The blocking function is equal to 1 at the start of deposition, decreases as deposition proceeds, and goes to zero when the substrate surface is saturated with deposited colloids.

The most important observation from Fig. 5.5 is the difference between the deposition kinetics of DEEDMAC and WE15 vesicles which is evident from the faster increase in apparent zeta potentials for deposition of DEEDMAC vesicles. For the deposition of DEEDMAC vesicles, the apparent zeta potential of cotton fibers reaches saturation after 6 measurement runs, while it takes 9 measurement runs for the same with WE15 vesicles. This indicates than the deposition kinetics of DEEDMAC vesicles is around 50% faster than that of WE15 vesicles. This difference was obtained consistently in multiple repetitions of the experiment. As the bulk vesicle concentration and flow conditions are the same for the two vesicles, the faster deposition kinetics of DEEDMAC vesicles could be a result of a higher deposition rate constant of DEEDMAC vesicles.

The difference in value of the deposition rate constant can possibly be related to differences in intrinsic properties of the vesicles, namely, vesicle shape and the flexibility of lipid bilayers. As DEEDMAC vesicles are hard and non-spherical, their deposition might occur via the “hit and stick" mode [123]. On the other hand, WE15 vesicles being flexible and spherical, might be capable of

rolling on solid surfaces, and thus might deposit via the slower “hit, roll and stick" mode. The above is, however, only a hypothesis, and has not yet been confirmed independently.

As postulated in Section 5.3.1, the faster deposition kinetics of DEEDMAC vesicles should have a distinct effect on the post-deposition distribution of deposited vesicles on cotton yarns. Given that the permeation rates of the two vesicles are similar, a faster deposition kinetics would lead to higher values of the ratio $\frac{R_{dp,o}}{R_{pr,o}}$. Therefore, it can be suggested that the deposition of DEEDMAC vesicles should be confined more to the external surfaces in comparison to the WE15 vesicles. This hypothesis is verified with the help of further experiments in the next section.

5.4.2 Equilibrium deposition of vesicles on cotton yarns

5.4.2.1 Role of lipid bilayer phase behavior : DEEDMAC vs. WE15 vesicles

The equilibrium deposition of the vesicles on porous cotton yarns was investigated via the experimental scheme shown in Fig. 5.2(A). The adsorption densities obtained on cotton yarns after deposition of DEEDMAC and WE15 vesicles are plotted in Fig. 5.6(A) against the vesicle concentrations in starting bulk dispersions. The dashed line in Fig. 5.6(A) represents the theoretical adsorption density values that would be attained if all the vesicles available in the starting dispersions are deposited. The variation of the apparent zeta potentials of cotton yarns with adsorption density is plotted in Fig. 5.6(B). In order to contrast the deposition behavior of the two vesicle types, in this section we consider only those experiments which are carried out at low bulk electrical conductivity (no salt). The prominent observations from Fig. 5.6(A) and 5.6(B) are the following :

1. Deposition of vesicles on cotton yarns proceeds with complete pick-up of all vesicles available in bulk dispersions until certain threshold adsorption density levels are attained. Once the threshold value is reached, very little or no additional deposition occurs. The data points representing these threshold adsorption densities have been marked with black borderlines. Unlike on single cotton fibers, the maximum adsorption density obtained on cotton yarns for the deposition of WE15 vesicles (70 mg/g) is much higher than that for DEEDMAC vesicles (37.5 mg/g).
2. The apparent zeta potential of cotton yarns increases much faster with adsorption densities for the deposition of DEEDMAC vesicles than for that of WE15 vesicles. As the apparent zeta potential of cotton yarns is sensitive mainly to deposition on external yarn surfaces, the above result indicates that for the same total deposited lipid mass, deposition on external yarn surfaces is greater for DEEDMAC vesicles than that for WE15 vesicles.
3. Once the threshold adsorption density as described above is reached, the cotton yarn apparent zeta potential increases very sharply whereafter deposition is completely stopped. The apparent zeta potentials of cotton yarns corresponding to these transition points are similar in magnitude and lie between +10 mV and +20 mV.

The relatively higher deposition on external yarn surfaces of DEEDMAC vesicles in comparison to that of WE15 vesicles could be explained in terms of differences in inherent deposition rates of the two vesicle types, as established in the Section 5.4.1. According to the deposition mechanism proposed in Section 5.3.1, a faster deposition rate of DEEDMAC vesicles would lead to a higher

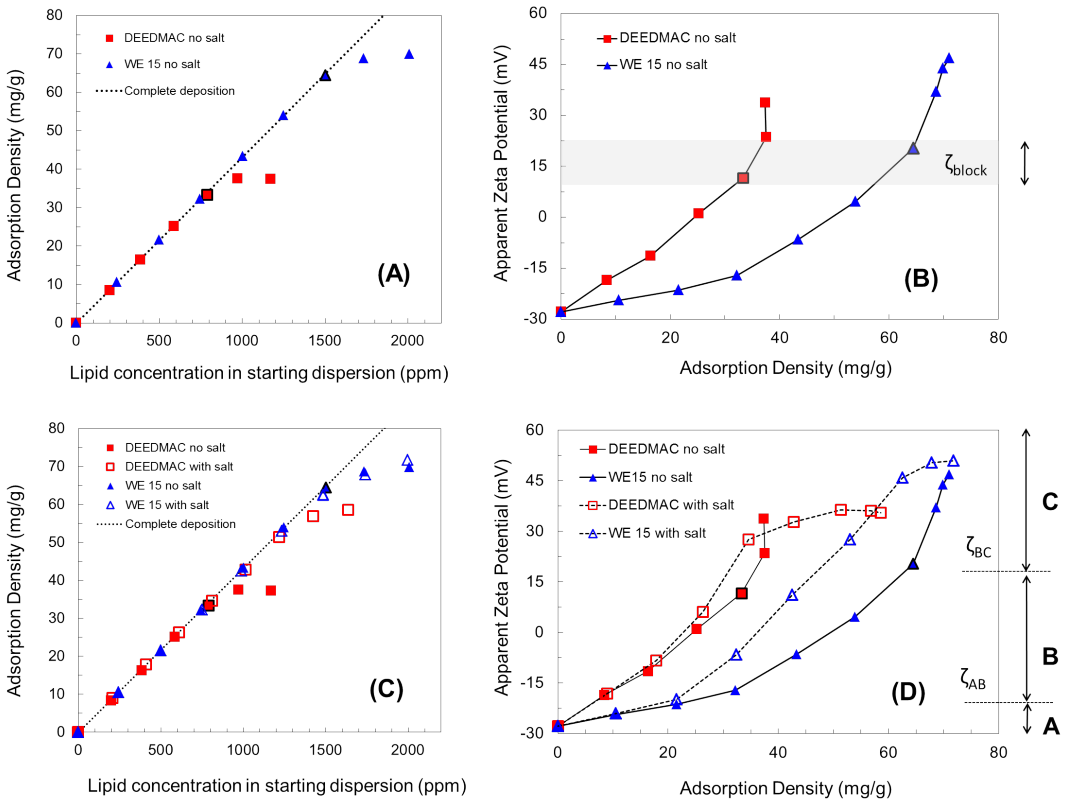

Figure 5.6.: Adsorption densities obtained by deposition of DEEDMAC and WE15 vesicles on porous cotton yarns in the absence of salt (A) and with salt (C). Variation of the apparent zeta potentials of porous cotton yarns with adsorption density of DEEDMAC and WE15 vesicles in the absence of salt (B) and with salt (D).

value of the ratio $\frac{R_{dp,0}}{R_{pr,0}}$, and hence more deposition occurs near the yarn periphery. The theory proposed in Section 5.3.1 thus explains this result quite well.

The other significant observation is the considerable difference in maximum adsorption densities obtained with DEEDMAC and WE15 vesicles, which is in contrast with the result on single cotton fibers where similar maximum adsorption density levels are obtained with the two vesicle types. A possible reason underlying this behavior could be that once deposition on external yarn surfaces reach a certain level, it blocks the further inwards permeation of colloids. Thereafter, deposition takes place only on external yarn surfaces which could be accessed directly by the vesicles from the bulk dispersion. The deposition process stops completely when the external surfaces are saturated with no more further deposition possible. The observed sharp increase in apparent zeta potentials of cotton yarns after the attainment of maximum adsorption densities also points towards the existence of such a blocking effect. A similar effect was observed by Kleinen et. al. [124] in their work dealing with polyelectrolyte deposition on porous microgels.

As the average size of the vesicles is quite small in comparison to the pore sizes in cotton yarns, the apparent blocking of inwards vesicle permeation, as discussed above, is improbable to occur via mechanical blocking. A plausible explanation could be that the inwards diffusive colloidal permeation is blocked due to electrostatic repulsion from already deposited vesicles on pore walls. Since these experiments were carried out at low bulk electrical conductivity levels where the electric double layers are thick ($\approx 1\mu m$), the electrostatic interactions have their maximum

possible strength, and could effect such a blocking. A similar electrostatic blocking phenomenon has been reported by Lieleg et. al. [113].

Additionally, the fact that the observed blocking takes effect only when the apparent zeta potential reaches a certain positive value (ζ_{block} in Fig. 9(B)) further supports the above-inference. Although most of the pores in cotton yarns are much larger than the sum of vesicle diameter and electric double layer thickness, some of the pores are small enough where such electrostatic repulsion might be strong enough to enforce such a blocking [125]. Additionally, the inter-fiber pores in the yarns during deposition would be smaller than those present initially. The swelling of fibers could reduce the pore volume in cotton textiles by as much as 40 % [21].

The proposed hypothesis can be verified by carrying out the experiments in the presence of sufficient electrolyte in the bulk liquid such that the electrostatic interactions are suppressed, as reported in the next section.

5.4.2.2 Influence of presence of electrolyte : Role of electrostatic interactions

The adsorption densities obtained on cotton yarns after deposition of DEEDMAC and WE15 vesicles at high bulk electrical conductivity (1 mS/cm) are plotted against the lipid concentrations in starting dispersions in Fig. 5.6(C). The variation of cotton yarn apparent zeta potentials with adsorption densities is plotted in Fig. 5.6(D). In order to be able to identify the effect of bulk electrical conductivity on the process, the results obtained earlier at low bulk electrical conductivity (no salt) have been shown again in the plots.

It can be observed from Fig. 5.6(C) that for DEEDMAC vesicles the maximum adsorption density attained at high bulk electrical conductivity (with salt) is much higher than that at low bulk electrical conductivity (no salt). On the other hand, the presence of salt in the bulk liquid has no significant effect on the maximum adsorption density attained for WE15 vesicle deposition. Furthermore, it can be observed from Fig. 5.6(D) that the profile of variation of cotton yarn apparent zeta potentials with adsorption density is considerably different at low and high bulk electrical conductivity levels for both DEEDMAC and WE15 vesicles.

Based on the obtained results, the profile of variation of cotton yarn apparent zeta potentials with adsorption density can be divided into three regimes (A, B, and C in Fig. 5.6(D)) :

- In regime A ($\zeta_{app} < \zeta_{AB}$), the variation of cotton yarn apparent zeta potentials with adsorption density is independent of the presence of salt in the bulk liquid.
- In regime B ($\zeta_{AB} < \zeta_{app} < \zeta_{BC}$), the cotton yarn apparent zeta potentials increase faster in the presence of salt than in its absence.
- In regime C ($\zeta_{app} > \zeta_{BC}$), the cotton yarn apparent zeta potentials increase sharply in the absence of salt, before deposition stops completely. In the presence of salt in the same regime the cotton yarn apparent zeta potentials are seen to reach a plateau before deposition stops.

The contrasting results obtained at the two different bulk electrical conductivity levels in regimes B and C point towards an important role played by the electrostatic interactions in the process. There are two kinds of electrostatic interactions experienced by the colloids during the deposition

process, namely, attractive electrostatic interactions between anionic cotton fibers and cationic vesicles, and mutually repulsive electrostatic interactions between cationic vesicles. Furthermore, when cationic vesicles are deposited on fiber surfaces, the repulsive interaction between deposited and dispersed vesicles effectively acts as a repulsive interaction between the vesicles and the fibers.

Since the zeta potential of the anionic cotton fibers ($\zeta = -20mV$) is lower in magnitude than that of the cationic vesicles ($\zeta = +60mV$), the attractive electrostatic interactions between cotton fibers and the vesicles are significantly weaker than the repulsive electrostatic interactions between the vesicles. The weaker attractive vesicle-substrate electrostatic interaction thus only plays a role in securing the attachment of vesicles to the fibers once the vesicles have been transported via diffusion to the fiber surface. These attractive interactions are, however, not strong enough to significantly influence the kinetics of vesicle permeation and deposition.

The repulsive electrostatic interactions between deposited vesicles and free vesicles are much stronger. The intensity of the repulsive interaction depends on the quantity of deposited vesicles, and thus increases with increasing vesicle adsorption density. These strong repulsive interactions can have a significant effect on the deposition and permeation kinetics, R_{dp} or R_{pr}, respectively. These interactions can thus influence the course of the deposition process, as postulated in Section 5.3.1. The intensity of the above-described electrostatic interaction is, however, reduced at high bulk electrical conductivity. The role played by electrostatic interactions in the deposition process can be hence elucidated by comparing the results obtained at low and high bulk conductivity, as described below.

In regime A, as deposition is still in its early stages, deposition levels on the fibers are low. Therefore, the repulsive electrostatic interactions between deposited and free vesicles are not strong enough to cause any significant changes to either R_{dp} or R_{pr}. In this regime, the post-treatment distribution of deposited vesicles is thus unaffected by bulk electrical conductivity, as is evident from the very similar profiles of apparent zeta potential variation in Fig. 5.6(D).

In regime B, the faster increase of apparent zeta potential with adsorption densities at high bulk conductivity indicates that repulsive electrostatic interactions do have an observable influence on deposition when ζ_{app} surpasses ζ_{AB}. It can be inferred from the results that in regime B more deposition occurs on external substrate surfaces in the case where electrostatic interactions are screened (i.e. with salt). According to the theory we postulated in Section 5.3.1, higher deposition levels on external substrate surfaces are attained due to high values of the ratio $\frac{R_{dp,0}}{R_{pr,0}}$. The above condition could be rewritten as below :

$$\frac{R_{\text{dp, }_0\text{ with salt}}}{R_{\text{dp, }_0\text{ no salt}}} > \frac{R_{\text{pr, }_0\text{ with salt}}}{R_{\text{pr, }_0\text{ no salt}}} \tag{5.7}$$

In earlier works investigating the deposition of charged colloids on solid surfaces, it has been demonstrated that once deposition on solid surfaces reaches a certain level, the deposition rate (R_{dp}) is slowed down due to repulsive electrostatic interactions between deposited and free colloids [126–128]. In such cases, R_{dp} is higher at high bulk conductivity where the electrostatic

interactions are screened. A similar situation is expected to exist in regime B. Therefore, the value of the ratio $\frac{R_{\text{dp, }_0 \text{ with salt}}}{R_{\text{dp, }_0 \text{ no salt}}}$ in Eq. 5.7 would be greater than 1.

On the other hand, the permeation rate (R_{pr}) would be influenced by these electrostatic interactions only when a significantly high level of adsorption density has been reached. The strong repulsive interactions between the vesicle-covered fibers and free vesicles would then be strong enough to retard the inwards diffusive permeation of vesicles. However, as the cotton fiber apparent zeta potential is largely negative in regime B, it is expected that the repulsive electrostatic interactions would not have as strong an effect on the permeation process as it would on the deposition process. Hence, the value of the ratio $\frac{R_{\text{pr, }_0 \text{ with salt}}}{R_{\text{pr, }_0 \text{ no salt}}}$ in Eq. 5.7 is expected to be close to 1. Hence, the condition given by Eq. 5.7 would be satisfied for regime B.

In regime C, apparent zeta potential of cotton yarns is observed to increase sharply for the low electrical conductivity case. It was hypothesized in the last section that the sharp increase in apparent zeta potential of cotton yarns observed in the absence of salt, and the subsequent stoppage of deposition is an outcome of the blockage of vesicle permeation into the yarns enforced by repulsive electrostatic interactions. The validity of this hypothesis could be validated by considering the results at high bulk electrical conductivity where such electrostatic interactions are screened. It could be seen from Fig. 5.6(D) that in the presence of salt neither a such sharp increase in apparent zeta potentials nor a stoppage of deposition is observed. Here, deposition continues to take place even as the apparent zeta potential of cotton yarns reaches its maximum value. This indicates that unlike in the case without salt, the formation of an adsorbed layer on the external yarn surfaces does not hinder vesicle permeation to the internal yarn surfaces when salt is present in the bulk liquid.

The above described results validate that repulsive electrostatic interactions could hinder vesicle permeation into a porous substrate, and thus influence the deposition process significantly. In the case of DEEDMAC vesicles such an electrostatic blocking results in a reduction in total deposition with the internal surfaces remaining relatively unoccupied. However, in the case of WE15 vesicles, the electrostatic blocking does not significantly affect the total deposition because when it takes effect, the internal surfaces are almost occupied.

5.5 Summary

In this Chapter, an experimental investigation of the deposition of fabric softener cationic vesicles on porous anionic cotton yarns has been carried out. The experimental difficulty of characterization of distribution of deposition across the porous substrate is overcome via an implementation of streaming potential measurements coupled with adsorption density measurements. Such a methodology enables the evaluation of distribution of deposition into external and internal cotton yarn surfaces. A hypothesis is proposed to describe the mechanism governing the distribution of deposition into external and internal porous substrate surfaces. The ratio of colloidal deposition and permeation rates is postulated as the main governing factor.

In the experiments, the phase behavior of lipid bilayers constituting the vesicles and the presence of electrolyte in the bulk liquid are found to be the important parameters influencing the process. While the deposition of vesicles with solid-gel phase bilayers (DEEDMAC) is found to be confined

to the yarn periphery, the deposition of vesicles with liquid-crystalline phase bilayers (WE 15) occurs quite homogeneously across the yarn cross-section. Additionally, the presence of inter-particle electrostatic interactions which could be tuned by adding electrolyte (salt) to the bulk liquid is found to influence the deposition of both the vesicle types. The effect of these parameters on the process could be explained in terms of their effect on the ratio of colloidal deposition and permeation rates.

The experimental results demonstrate that the distribution of deposition across the porous structure varies during the process with increasing adsorption density levels on the substrate. It is also demonstrated that once vesicle deposition on the external surfaces of cotton yarns reach a certain level the subsequent inwards permeation of vesicles could be blocked due to repulsive electrostatic interactions. However such a blocking effect could be inhibited by increasing the bulk electrolyte concentration.

6 Spreading and imbibition of vesicle dispersion droplets on porous substrates

The wetting of porous substrates by vesicle dispersion droplets which involves simultaneous droplet spreading and liquid imbibition into the substrate pores is the subject of investigation in this chapter. The wetting process constitutes an important step in the spray application of complex liquid formulations on porous substrates as outlined in the Introduction of this thesis. Once the wetting of the substrate is complete, it is followed by the liquid evaporation and eventually leads to stain formation due to the deposited non-volatile particles. These evaporation and deposition processes are described in the next Chapter.

This chapter is based on the article, *Spreading and imbibition of vesicle dispersion droplets on porous substrates*, by Kumar et al. (2018) published in Colloids and Interfaces.

6.1 Background of liquid droplet spreading on porous substrates

The process of simultaneous spreading and imbibition of droplets of Newtonian and non-Newtonian liquids on dry porous substrates is relevant in several applications such as inkjet printing [129], dried spot sampling of blood and other biological liquids [130, 131], softening of paper and textiles [132], and transdermal delivery of drugs and cosmetic ingredients [133, 134]. The mechanism of such spreading processes has been investigated in earlier works for Newtonian liquids like water, silicone oil [9, 135], and more recently also for non-Newtonian complex liquids like blood [10, 136]. However, there is not much known about the about the spreading behavior on dry porous substrates of vesicle dispersions which form a commercially important class of complex liquids. Considering the widespread interest in usage of vesicle dispersions in various applications where they are sprayed as droplets onto porous substrates like paper, textile [26, 123], hair [106] and human skin [137, 138], it is important that their spreading behavior on porous substrates be well understood.

When liquid droplets loaded with actives are sprayed onto a porous substrate with the goal of attaining a certain desired result, the final performance among several factors is influenced by the kinetics of droplet spreading and imbibition. Depending upon the purpose of the treatment either a fast or a slow rate of droplet spreading and imbibition could be desirable. A practical example is the industrial surface modification of paper and textiles where an aqueous dispersion of active ingredients is sprayed onto the substrate, and subsequently dried before being spooled onto rolls at high speeds, as shown schematically in Fig. 6.1. For a superior surface modification performance, it is desirable that most of the active ingredients are deposited on the external paper surfaces. This could be achieved by minimizing the penetration of the liquid formulation into the porous substrate. Therefore, it is very important to have a good understanding of the spreading and wetting process.

The spreading of Newtonian liquids over smooth homogeneous surfaces has been investigated in several earlier works [139, 140]. However, the mechanism of the spreading process is different

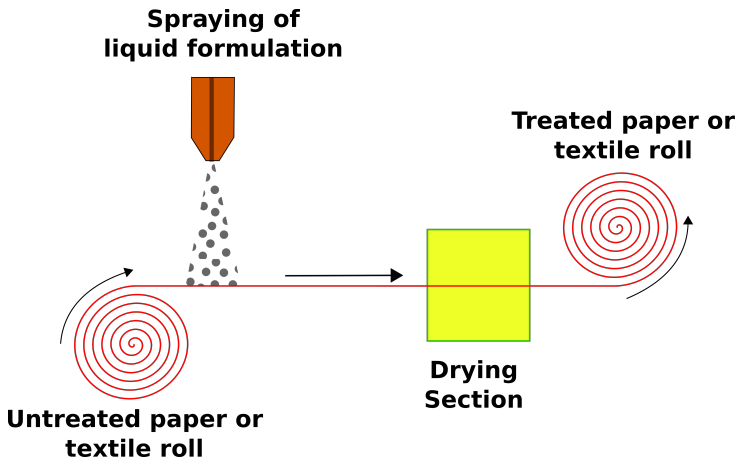

Figure 6.1.: Schematic representation of a typical surface modification treatment as carried out in industries

in the presence of substrate porosity [141]. Starov et. al. [141] described the spreading of small drops of Newtonian liquids over thin porous layers saturated with the same liquid. The mechanism of droplet spreading on dry porous substrates is considerably different.

The spreading process of liquid droplets on dry porous substrates kicks off once the droplets contact the porous substrate, and proceeds with the formation of a liquid cap over the porous substrate and simultaneous imbibition-driven liquid penetration into the porous substrate, as shown schematically in Fig. 6.2(A). The kinetics of the process is characterized in terms of the rates of variation of spreading parameters, namely, the base radius ($L(t)$) and dynamic contact angle of the liquid cap ($\theta_c(t)$), and radius of the wetted region ($l(t)$) [9]. The spreading kinetics is typically governed by the porous substrate's structure, the wettability of solid surfaces by the liquid, and the liquid's rheological properties . Other physico-chemical interaction between the dispersion and the substrate such as adsorption, blockage of pores could also be important [142]. The effect of gravity could be neglected for low droplet volumes where the Bond number, Bo, is much less than 1.

In previous works [136], based on the characteristic trends observed in variation of spreading parameters, $L(t)$, $l(t)$ and $\theta_c(t)$, such droplet spreading processes have been classified qualitatively into two categories, namely, the so called partial and complete wetting cases. The spreading cases were so named as they were initially observed on a porous substrate with complete and partially wetting liquids, respectively. In reality, the wetting case is identified by the mode of variation of spreading parameters, $L(t)$, $l(t)$ and $\theta_c(t)$, with time. The characteristic profiles of variation of $L(t)$, $l(t)$ and $\theta_c(t)$, with time which are used to determine whether the spreading process is of the complete or the partial wetting type has been shown schematically in Fig. 6.3(B), and discussed in detail in Section 6.2.

After the primary wetting process involving simultaneous spreading and imbibition, comes to an end, further radial penetration of liquid has been reported [143]. The secondary penetration has been explained to occur due to competitive spreading between pores in the porous substrate until equilibrium is finally attained [143]. The extent of secondary liquid penetration could depend on factors such as droplet volume and thickness of the porous substrate. The extent of

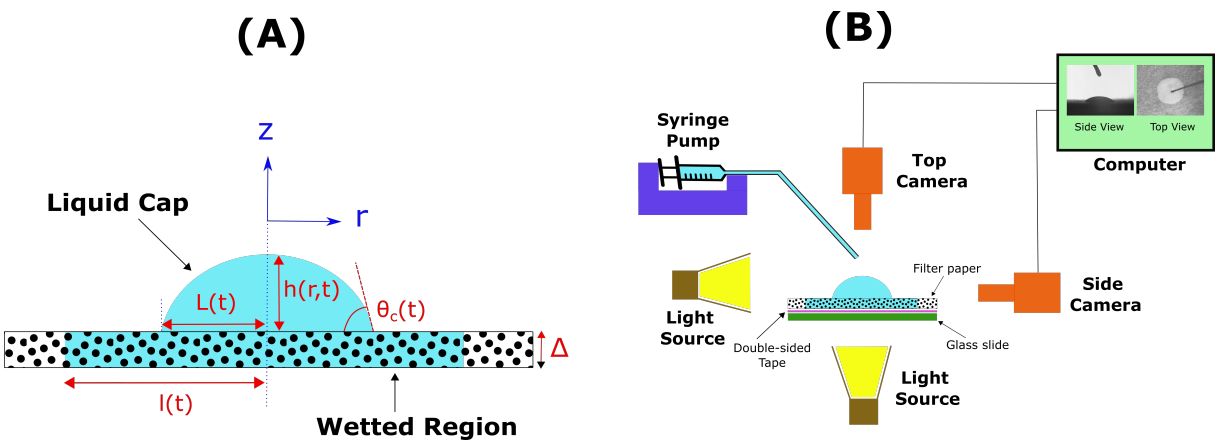

Figure 6.2.: (A) Schematic representation of the simultaneous droplet spreading and imbibition process showing the spreading parameters, the base radius, $L(t)$, the dynamic contact angle of the liquid cap, $\theta_c(t)$, and radius of the wetted region, $l(t)$. (B) Sketch of the experimental setup used for the experiments

secondary radial liquid penetration of complex liquid droplets has also been investigated in this Chapter.

6.2 Partial vs. Complete wetting case

In the partial wetting case, the overall spreading process could be divided into three stages A, B and C, as shown in Fig. 6.3(A). Stage A involves a relatively rapid spreading of the droplet until the liquid cap base radius, $L(t)$, reaches its maximum value L_m, and the dynamic contact angle, $\theta_c(t)$, reaches the transition value of θ_{ad}. In stage B, $L(t)$ remains fixed at L_m while $\theta_c(t)$ decreases from θ_{ad} to θ_r. In stage C, $\theta_c(t)$ remains fixed at θ_r while L decreases from L_m to zero. The partial wetting case is characterized by the presence of Phase B in which the liquid cap base remains pinned and results in a contact angle hysteresis.

The complete wetting case is different from the partial wetting case due to the non-existence of Stage B (as shown in Fig. 6.3(A)). In this case, as the liquid cap base radius, $L(t)$ reaches its maximum value of L_m at the end of Stage A, the liquid cap starts receding almost instantaneously without being pinned. Furthermore, as the liquid cap base recedes during Phase C, the contact angle, $\theta_c(t)$, remains constant at a certain value of θ_f.

6.3 Materials and Methods

6.3.1 Materials

Solid-gel WE18 and liquid-crystalline WE15 vesicles are used for the investigations are described in Chapter 2. Only the small vesicles were used for the experiments as the large vesicles are comparable in size to the substrate pores. Commercial cellulose fiber filter papers, namely, Whatman 903 and Sartorius 388, were used as porous substrate for the spreading experiments. The properties of the filter papers are described in Chapter 2. Although the two substrates have

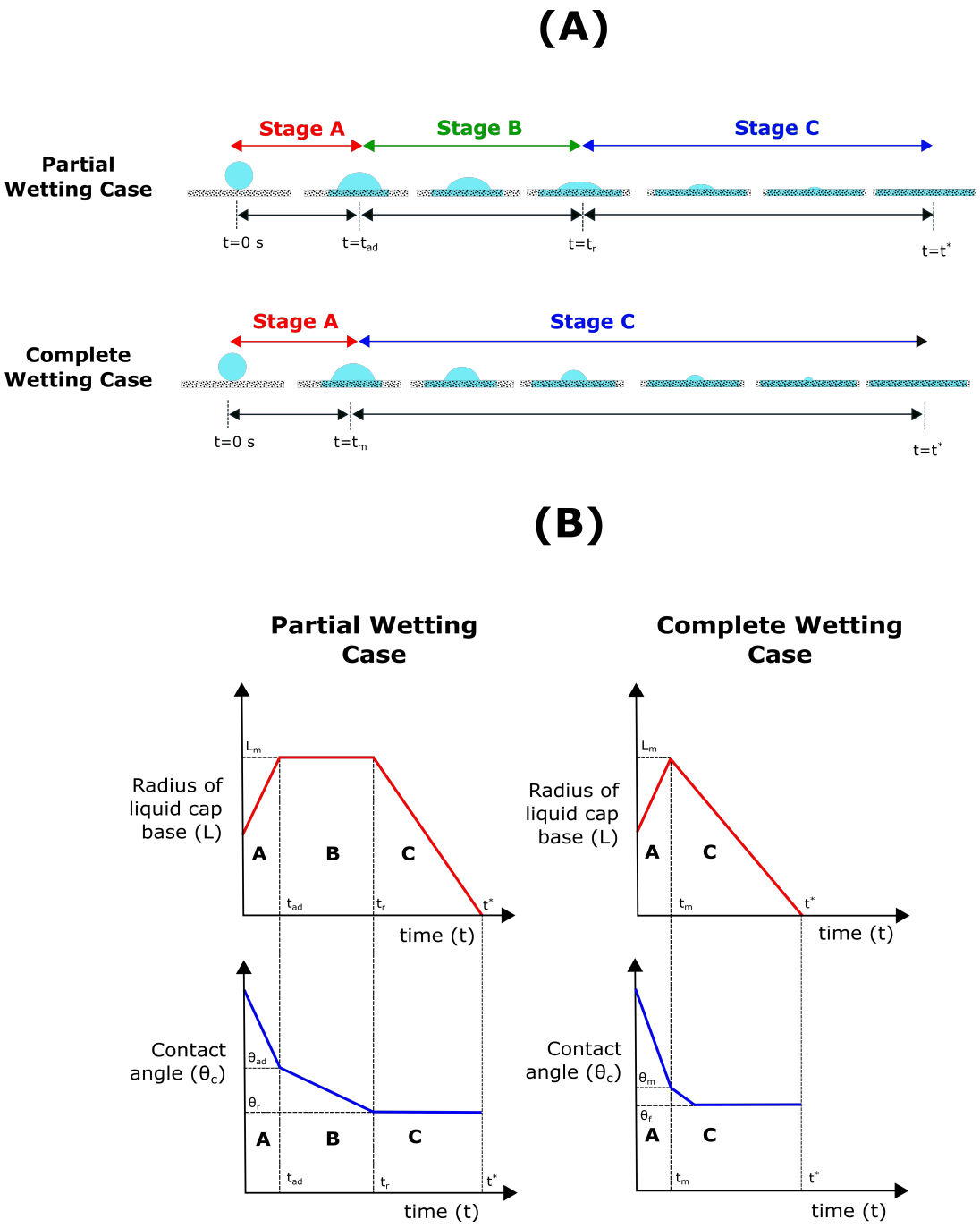

Figure 6.3.: Schematic representation of the characteristic trends in variation of the spreading parameters, L (liquid cap base radius) and θ_c (contact angle) in the cases of partial and complete wetting

similar pore sizes and the thicknesses of Whatman 903 and Sartorius 388 are 500 μm and 210 μm, respectively.

6.3.2 Spreading experiments

The simultaneous spreading and imbibition of liquid droplets on porous substrates is observed using an experimental setup as shown schematically in Fig. 6.2(B). The liquid cap which is formed over the porous substrate is imaged from the side using a high speed camera (i-Speed

LT from Olympus). The wetted area formed inside the porous substrate due to imbibition is simultaneously imaged using a camera from the top (Pike F-032 from Allied Vision). The liquid droplets with volume of 10 ± 0.5 μl were produced using a syringe pump (Nanomite from Harvard Apparatus). A set of images obtained in a particular experiment from the top-view and side-view cameras have been shown in Fig. 6.4. The values of the spreading parameters ($L(t)$, $l(t)$ and $\theta_c(t)$) were measured directly from the recorded images using the open source image analysis software ImageJ. The experiments were conducted twice to ensure the reproducibility of the results.

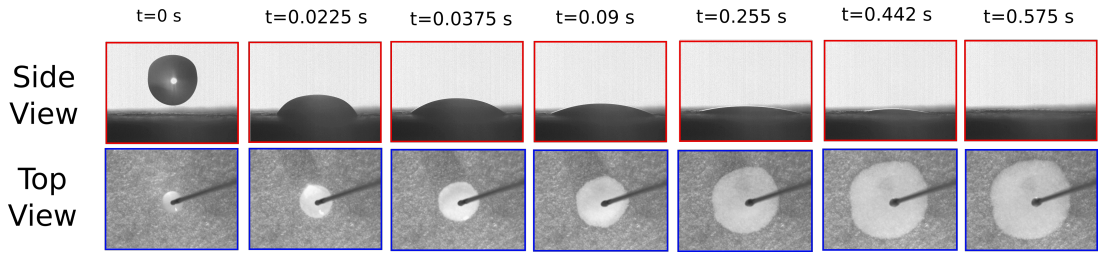

Figure 6.4.: Evolution of the liquid cap and the wetted area with time for the spreading of a WE18 droplet on Sartorius 388 filter paper, as observed from the side and top cameras, respectively. The dimensions of the side view and the top view images are 7.4 mm × 5.6 mm and 18.3 mm × 13.8 mm, respectively.

6.4 Results and Discussion

6.4.1 Droplet spreading kinetics

The variation of the spreading parameters, $L(t)$, $l(t)$ and $\theta_c(t)$, with time as obtained in the experiments is plotted in Fig. 6.5. The most important observation from Fig. 6.5 is that the spreading behavior of both WE15 and WE18 droplets is of the complete wetting type on Whatman 903 while it is of the partial wetting type on Sartorius 388. Furthermore, the time required for full imbibition of the droplets is much less for Whatman 903 than that for Sartorius 388. As the porosities of the two substrates are comparable, the difference in spreading behavior could be attributed to the greater thickness of Whatman 903. The greater thickness of Whatman 903 leads to an higher rate of liquid penetration into the porous substrate due to imbibition. The higher rate of liquid penetration into the porous substrate leads to “complete” wetting behavior in the case of Whatman 903. On the other hand, due to the slower liquid penetration rate, the wetting behavior on Sartorius 388 is of the partial wetting type.

The second most important observation from Fig. 6.5 (A) and (D) is the difference between spreading kinetics of WE18 and WE15 droplets on both Whatman 903 and Sartorius 388. It is observed that the spreading of WE15 droplets is faster than that of WE18 droplets. As the difference in phase behavior of lipid bilayers inside the vesicles has no effect on capillary forces, the difference in spreading kinetics should be a result of the difference in viscosities of the two vesicle dispersions. Given that the capillary forces are unchanged, the liquid with lower viscosity penetrates into the porous substrate faster [144]. As a result the spreading of WE15 droplets is faster than the spreading of WE18 droplets. The same was observed in an earlier work involving blood droplets where the blood droplet with higher viscosity was spread and imbibed faster on the substrate [145].

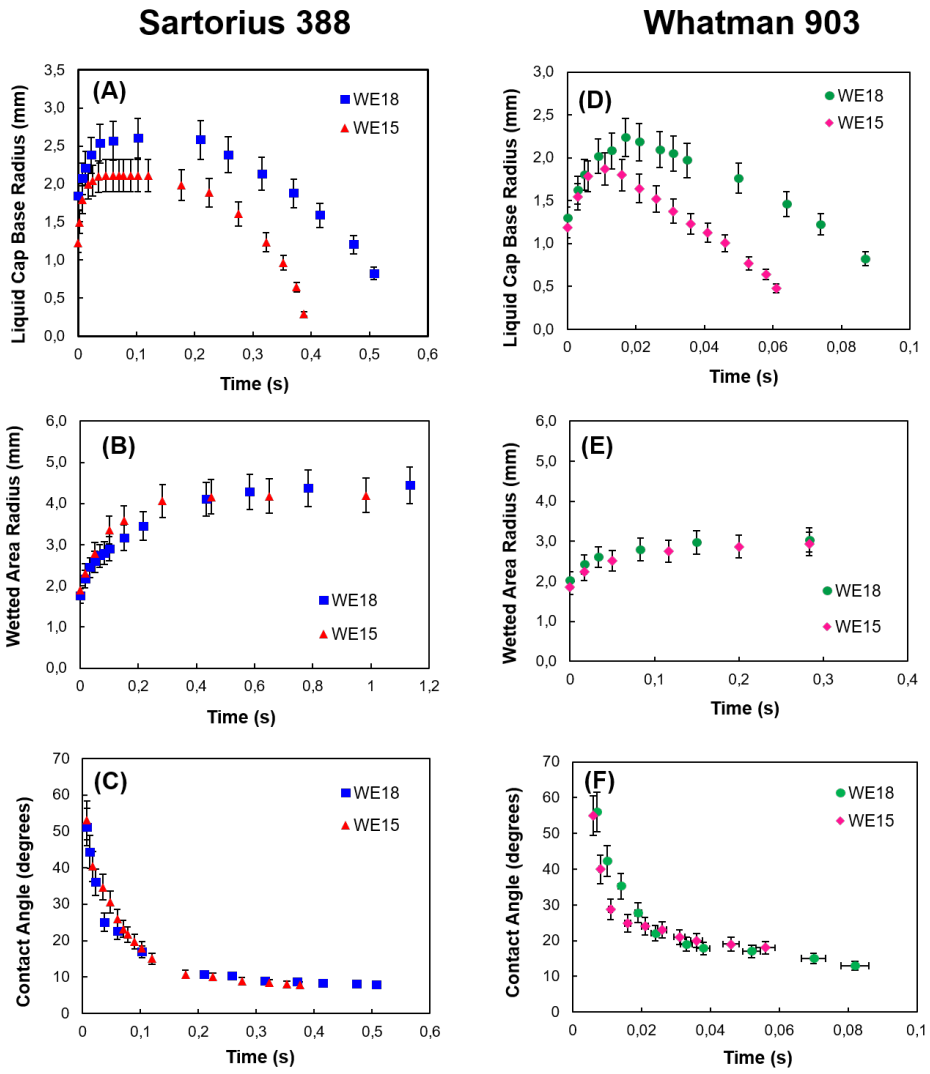

Figure 6.5.: Evolution of the liquid cap base radius, the wetted area radius, and the contact angle with time for the spreading of WE18 and WE15 droplets on Sartorius 388 (A,B and C) and Whatman 903 (D, E and F)

6.4.2 Non-dimensionalized droplet spreading kinetics

The spreading parameters, $L(t)$, $l(t)$ and $\theta_c(t)$, and the spreading time, t, are non-dimensionalized according to the method described by Chao et. al. [136] :

$$\overline{L} = \frac{L(t)}{L_{ad}} \tag{6.1}$$

$$\overline{l} = \frac{l(t)}{l^*} \tag{6.2}$$

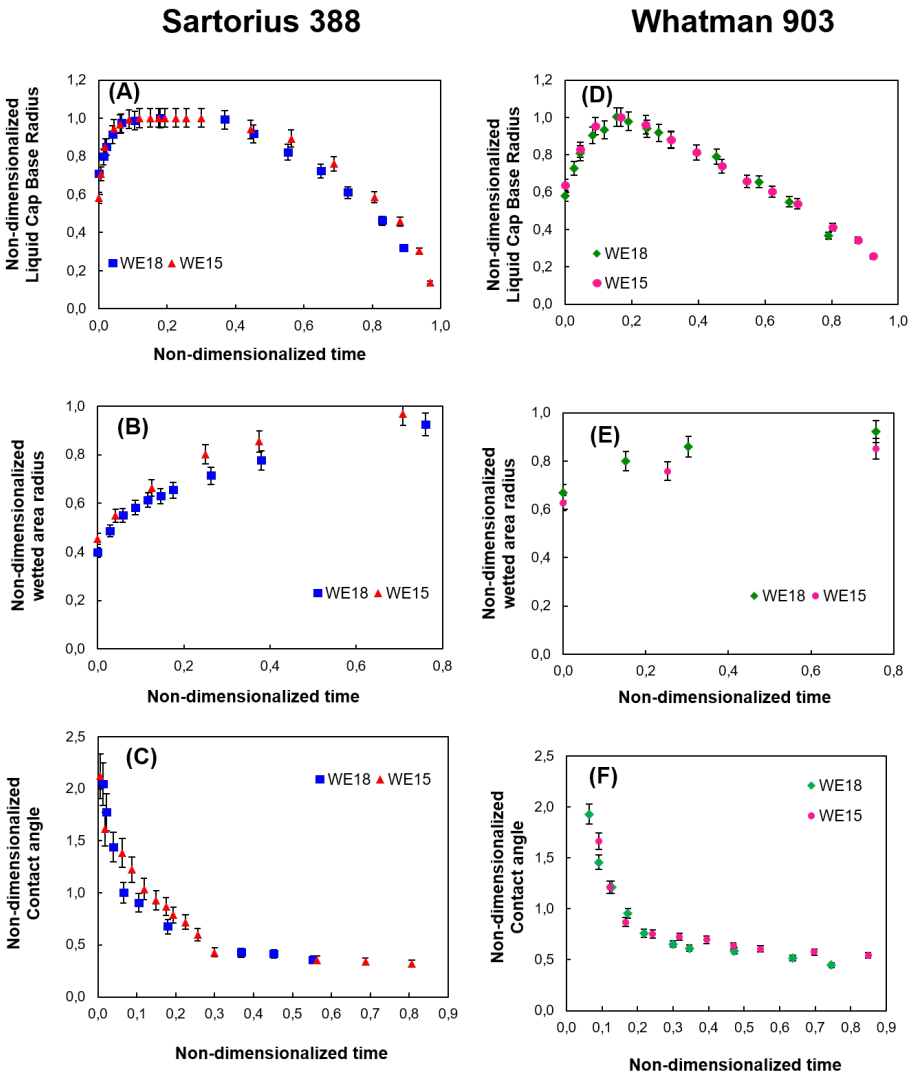

Figure 6.6.: Evolution of the non-dimensionalized liquid cap base radius, the wetted area radius, and the contact angle with non-dimensionalized time for the spreading of WE18 and WE15 droplets on Sartorius 388 (A,B and C) and Whatman 903 (D, E and F)

$$\overline{\theta} = \frac{\theta(t)}{\theta_{ad}} \tag{6.3}$$

$$\overline{t} = \frac{t}{t_*} \tag{6.4}$$

where, L_{ad} is the maximum radius of the liquid cap base, l^* is the radius of wetted region at the end of the process, t_* is the time when complete imbibition is finished. The variation of non-dimensionalized parameters, $\overline{L}$, $\overline{l}$, $\overline{\theta}$ with non-dimensionalized time, $\overline{t}$, is plotted in Fig. 6.6. It could be identified from Fig. 6.6 that the non-dimensionalized spreading kinetics of WE18 and WE15 droplets are identical on Sartorius 388 and Whatman 903. This confirms that the

Liquid type	Ratio of final to intermediate wetted area diameters	
	Sartorius 388	Whatman 903
Water	1.23	1.55
WE18	1.11	1.18
WE15	1.08	1.17

Table 6.1.: Secondary radial penetration of water, WE18 and WE15 vesicle dispersions on Sartorius 388 and Whatman 903

phenomena governing the spreading of WE18 and WE15 droplets are identical and the difference in spreading kinetics is only a result of the difference in rheological properties of the vesicle dispersions.

6.4.3 Secondary radial liquid penetration

The secondary radial penetration of the liquid occurs after the liquid cap has disappeared over the substrate and is shown schematically on Fig. 6.7(A). In the experiments, the wetted areas observed right after the disappearance of the liquid cap and after equilibrium has been reached are reported for the different liquid-substrate combinations on Fig. 6.7(B). Apart from the WE18 and WE15 vesicle dispersions, the secondary penetration of water droplets was investigated as well. The ratio of the equilibrium wetted area to the intermediate wetted area provides a measure of the extent of secondary liquid penetration and is enlisted in Table 6.1 for both the types of papers.

It can be observed from Table 6.1 that the extent of secondary liquid penetration is higher on Whatman 903 than on Sartorius 388 for all the liquids. Among the liquids, the extent of secondary liquid penetration is highest for water followed by both WE18 and WE15 which are comparable. The above observations indicates that the extent of secondary liquid penetration is dependent on both substrate thickness as well as liquid viscosity. A higher substrate thickness leads to a higher number of capillaries pulling out the liquid in the radial direction, and hence results in greater secondary spreading. The peripheral region gets filled at the expense of liquid from the center. In addition, as a liquid with high viscosity would not flow easily under the action of the radial capillary forces, WE18 and WE15 vesicle dispersions with higher viscosities exhibit much lower secondary liquid penetration.

6.5 Summary

In this Chapter, the simultaneous spreading and imbibition of vesicle dispersion droplets on porous cellulose fiber filter papers is investigated. Two porous substrates of comparable porosity but different thicknesses (500 μm and 210 μm) were used. Two vesicles dispersions containing sub-micron size vesicles which are composed of chemically similar lipids but exhibit contrasting lipid bilayer phase behavior are used. It is shown that the spreading behavior of vesicle dispersions on porous substrates is strongly influenced by the thickness of the porous substrate as well as the phase behavior of the lipid bilayers constituting the vesicles. Droplet spreading behavior is of the complete wetting type on Whatman 903 which has a thickness of 500 μm, while it is of the partial wetting type on Sartorius 388 which has a thickness of 210 μm. On

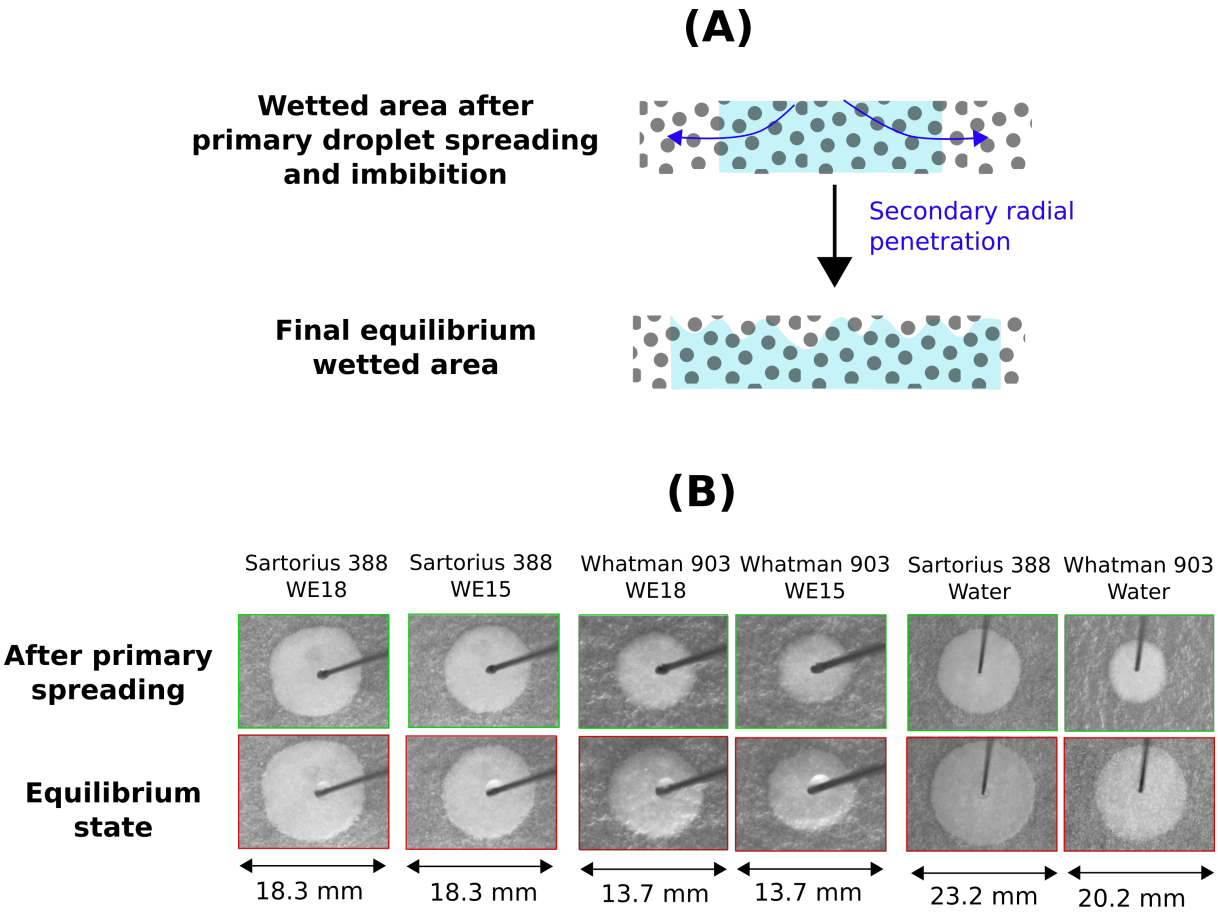

Figure 6.7.: (A) Schematic representation of secondary radial liquid penetration, (B) Wetted areas observed right after the disappearance of the liquid cap and after equilibrium has been reached for different liquid-substrate combinations

both the filter papers, the spreading kinetics of the liquid droplets containing WE18 vesicles with solid-gel phase bilayers is slower than that of liquid droplets containing WE15 vesicles with liquid-crystalline phase bilayers. It is shown that the faster spreading kinetics of WE15 vesicles is due to its lower viscosity which results in a faster rate of liquid penetration into the porous substrate via imbibition. A good understanding of the droplet spreading kinetics could be useful in real-life applications such the softening treatment of paper, where the process parameters could be optimized to attain much better results.

7 Evaporation of imbibed complex liquids droplets on porous substrates

7.1 Introduction to liquid droplet evaporation on porous substrates

The evaporation of colloidal droplets on flat solid surfaces typically results in the accumulation of colloids near the 3-phase contact line which is referred to as the coffee ring effect [146]. The reason underlying the formation of the coffee rings was described to be the pinning of the 3-phase contact line during evaporation and the radial capillary transport of colloids due to the higher rate of evaporation at the droplet periphery [146].

A similar phenomenon is observed on porous substrates, where the colloidal droplet is firstly imbibed by the porous substrate to form a wetted region, and thereafter gradually evaporated. In this case, at the end of evaporation the deposition of colloids is greater near the periphery of the wetted region [5]. Although the underlying mechanism of coffee ring formation on flat solid surfaces is well known, the corresponding effect on porous substrates is still not very well elucidated. Niglaz et. al. [5], one of the first works to investigate coffee ring formation on filter paper, showed that it is influenced by both, the evaporation as well as the substrate properties. A comprehensive understanding of the mechanism of this process is still not available. A good understanding of this phenomena is desirable due to its relevance in numerous applications such as inkjet printing on porous substrates, dried spot sampling of biological samples, and spray application of formulations on paper substrates.

In this chapter, the formation of coffee rings on porous substrates has been investigated experimentally. The dispersion of cationic lipid vesicles is used as model complex liquid for the investigations. Cellulose fiber filter papers were used as porous substrates. The droplets were placed on the porous substrate, and the evaporation process was observed from the top. The rate of evaporation was simultaneously characterized using an analytical balance. A combination of the two measurement techniques is used to obtain insights into the mechanism underlying the coffee ring formation. Furthermore, the trends in variation of size of the coffee rings with different parameters such as droplet size, colloidal concentration, porous substrate pore size and temperature are investigated and explained.

7.2 Materials and Methods

7.2.1 Materials

Dispersion of small vesicles ($d_{avg} < 1\ \mu m$) composed of the esterquat, Rewoquat WE18, as described in Chapter 2, has been used as the model complex liquid for most of the evaporation experiments in this Chapter. The used vesicle dispersion has a lipid concentration of 8 wt. %. Cellulose fiber filter papers, namely, Whatman 903 and different grades of Sartorius filter

papers, namely, 388, 389, 390 and 392 were used as porous substrates for the experiments. The properties of these filter papers have also been described in Chapter 2. Whatman 903 and Sartorius 388 were used as porous substrates in Chapter 6 where their wetting by droplets of the same vesicle dispersions is investigated.

7.2.2 Evaporation experiments

The evaporation of liquid droplets imbibed on the porous filter papers is investigated using the experimental setup shown schematically in Fig. 7.1(A). The mass variation during evaporation is characterized using a high precision analytical balance, the Sartorius Cubis MSE524P-100-DU which has a resolution of 0.1 mg. The evaporation process is visualized from the top using a digital color microscope, the Tagarno FHD Trend, which records the evolution of the evaporating area. The liquid droplets are generated using the syringe pump LA 100 from HLL. The whole experimental arrangement is housed inside a Glovebox, the Labmaster SP from MBraun, which is filled with pure nitrogen (see Fig. 7.1(B)).

The porous filter papers are stuck onto transparent glass slides using transparent double-sided tape to prepare the substrate samples used for the experiments. These samples allow us to visualize the substrate from the top as well as the bottom. A homemade plexiglass table is used as a platform on which the samples are placed. The plexiglass table has a highly reflective metallic mirror which is placed at an inclination of 45 degrees below the samples. In order to observe the evaporating area more distinctly the substrate is illuminated from the back with UV light. The used light source is a 51 LED UV blacklight lamp from Vansky. The UV lamp is placed horizontally adjacent to the plexiglass table wherein the mirror reflects the UV light towards the back of the sample. The real arrangement with the plexiglass table, the UV lamp and the illuminated sample could be seen in Fig. 7.1(C).

Once the evaporation process is completed, the UV illumination is switched off, and the final stains formed on the substrate are imaged under normal white light from both the top as well as bottom (see Fig. 7.1(D)). Each evaporation experiment is repeated twice to ensure the reproducibility of the measurements.

7.2.3 Elimination of the zero drift

The employed experimental scheme involves obtaining the kinetics of liquid evaporation via mass measurements at fixed timed intervals using an analytical balance. A common problem associated with such continuous mass measurements is an anomalous negative drift in the mass measurements. In our case, it was observed that when the plexiglass table was placed on the balance, the mass measurements decreased at a steady rate even in the absence of any evaporating liquid. However, the mass reduction was not present when the plexiglass table was not placed on the balance. It was speculated that the observed negative mass drift might occur due to the air trapped inside the plexiglass table escaping into the outside due to being heated by UV light. The mass of the escaped air results in a reduction of the measured mass.

In order to minimize this effect, the original plexiglass table was modified and a large rectangular window was manifactured at it's back which allows air from outside and inside to mix well. As a result, the heat added to the system by the UV light is distributed throughout the air enclosed in

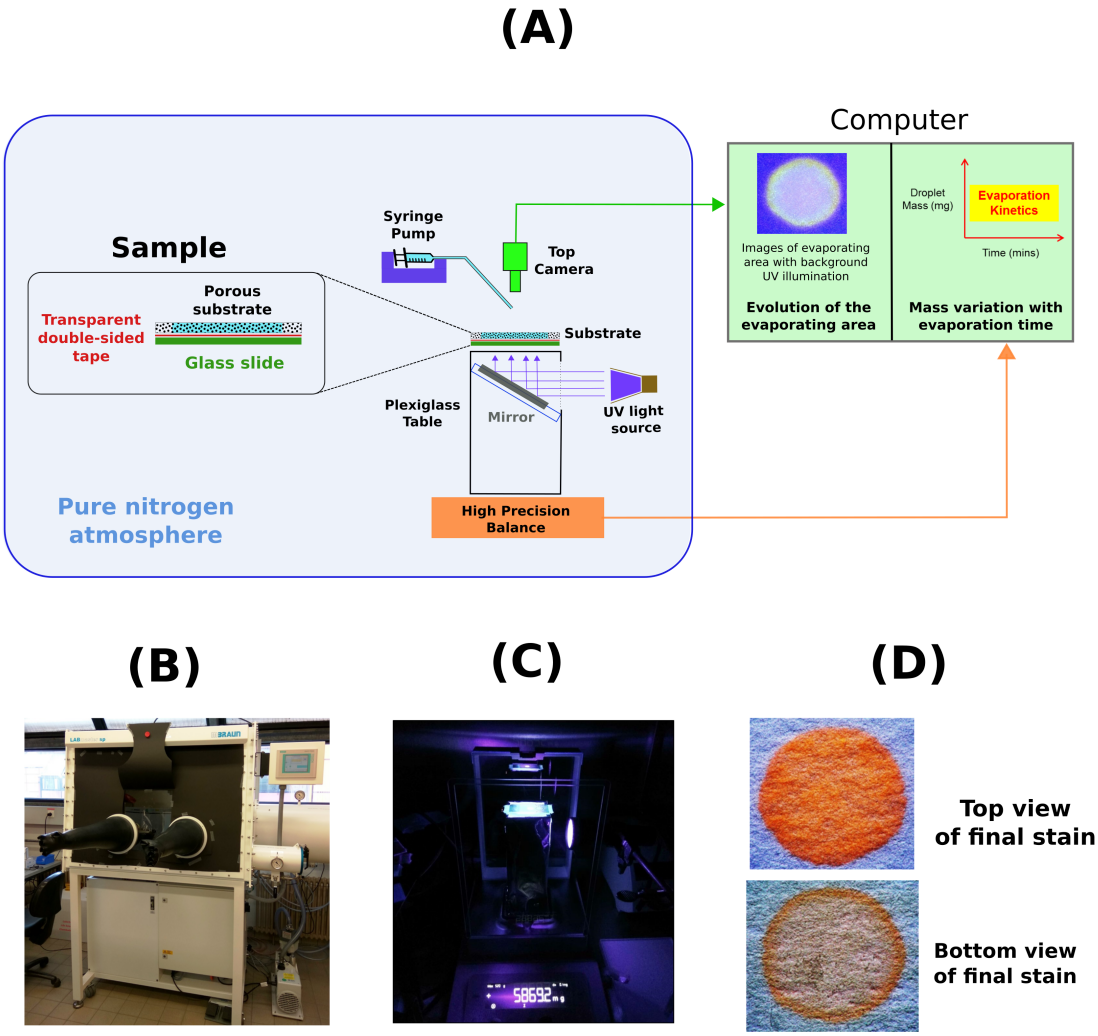

Figure 7.1.: (A) Schematic representation of the experimental setup, (B) The Glovebox, Labmaster SP, which houses the experimental setup, (C) The arrangement showing the plexiglass table, the analytical balance, the UV light source, (D) Typical images of the top and botton views of the final stains

the large Glovebox and hence the zero drift is reduced. The zero drift effect could be further minimized by waiting for around 15 mins before placing the liquid on the substrate. During this time the substrate and air temperatures reach equilibrium and no subsequent zero drift is observed. The original and modified plexiglass tables are shown schematically in Fig. 7.2(A) and (B). The zero drifts obtained with the two arrangements are shown in Fig. 7.2(C), where the reduced zero drift obtained with the modified plexiglass table is quite evident. In order to validate that the zero drift in evaporation experiments has almost been eliminated, the mass variation obtained in two similar evaporation experiments carried out with and without the UV lighting and the plexiglass setup are compared as shown in Fig. 7.2(D). It could be identified that there is no significant difference between the two mass variation curves indicating that zero drift has been almost eliminated.

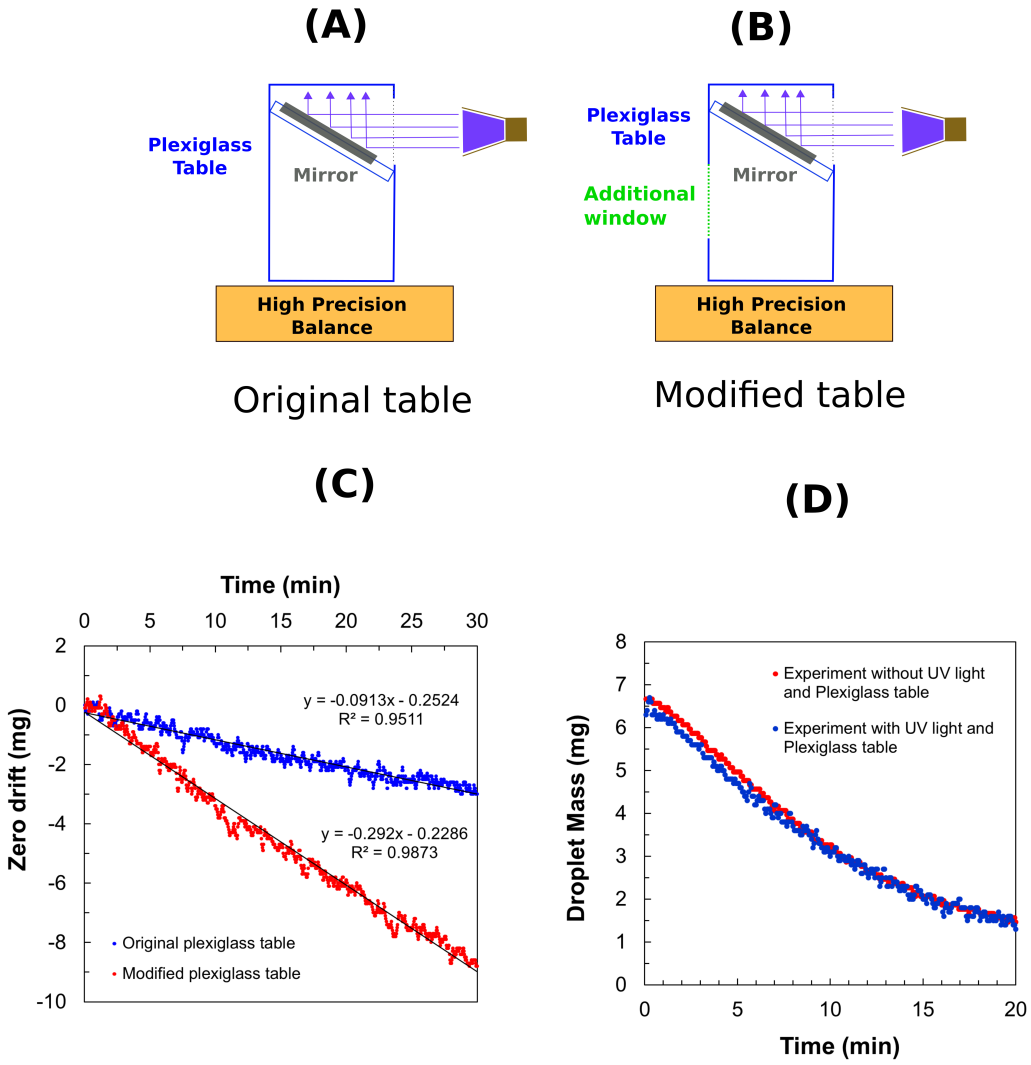

Figure 7.2.: Schematic representation of the (A) original and (B) modified plexiglass tables, (C) Observed zero drifts with original and modified plexiglass tables

7.3 Data processing and analysis

7.3.1 Analysis of images of the evaporating area

In this section, the methodology implemented for the analysis of the images obtained from the top camera are discussed. The images obtained during evaporation of a wetted area formed by 30 mg of the model complex liquid (Small WE18 vesicle dispersion) has been considered as test case for the analysis. During the evaporation process, the camera placed at the top captures the evolution of the evaporating area with time. In these images, the bare substrate appears blue in color, the liquid filled area appears white, and as time proceeds, an orange colored ring is seen forming at the periphery of the initially wetted area. The evolution of the evaporation area is tracked via the color intensity profiles along the horizontal and vertical center lines of the images. In order to avoid local aberrations in pixel intensity values, the color intensities are averaged over the height of thin rectangular windows aligned along the horizontal and vertical

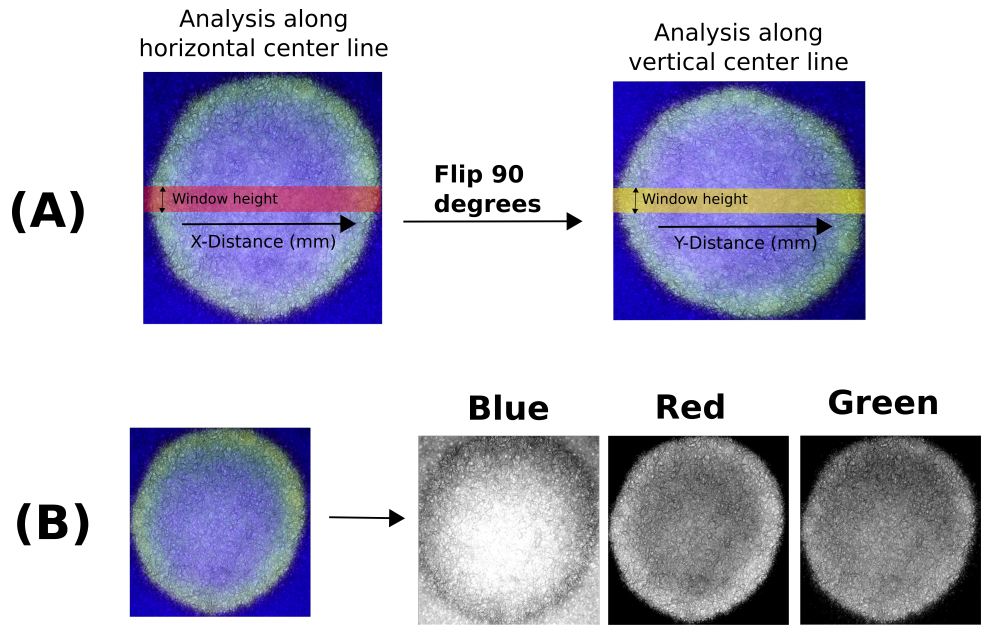

Figure 7.3.: (A) Rectangular sections for the extraction of color intensity profiles along the horizontal and vertical center lines of images, (B) View of evaporation area in the red, green and blue color channels.

center lines as shown in Fig. 7.3(A). The height of the rectangular window is typically set to $(1/10)^{th}$ of the total wetted area diameter.

It is identified from the images that among the three colors, Red, Green and Blue, the blue color is the one which is sensitive to both, the presence of non-evaporated liquid as well as the stain formed due to deposition. This is distinctly identifiable in Fig. 7.3(B) where the images corresponding to the red, green and blue channels of a certain image are shown separately. In the blue channel, a bright area is observed in the center which most likely represents the area predominantly occupied by the liquid, whereas the dark periphery represents the area where less liquid is present and significant deposition has already taken place. The red and green channel images appear more homogeneous where it is difficult to distinguish the liquid-dominated and deposition-dominated regions. Hence, the intensity profiles of the blue color are chosen for analysis of the evaporating area.

The images obtained at different times during the test evaporation experiment have been shown in Fig. 7.4(A). The blue color intensity profiles obtained along the horizontal center line of images at different times have been plotted in Fig. 7.4(B). It could be identified that the profiles are composed of two distinct parts, a plateau region in the center and a slope region near the periphery. The existence of the plateau region represents the region containing the most amount of liquid at any stage during the process. The slope region of the intensity profile corresponds to the region containing less liquid and deposited particles. In the image at the beginning of the evaporation process, the slope part represents the area containing less liquid which is filled in the secondary liquid penetration stage of the wetting process as described in Chapter 6.

During the course of evaporation, the plateau region diminishes both in terms of its height as well as its diameter. It is conceptualized that the mode of variation of the plateau diameter could provide us important insights into process mechanism. As the plateau height and diameter vary

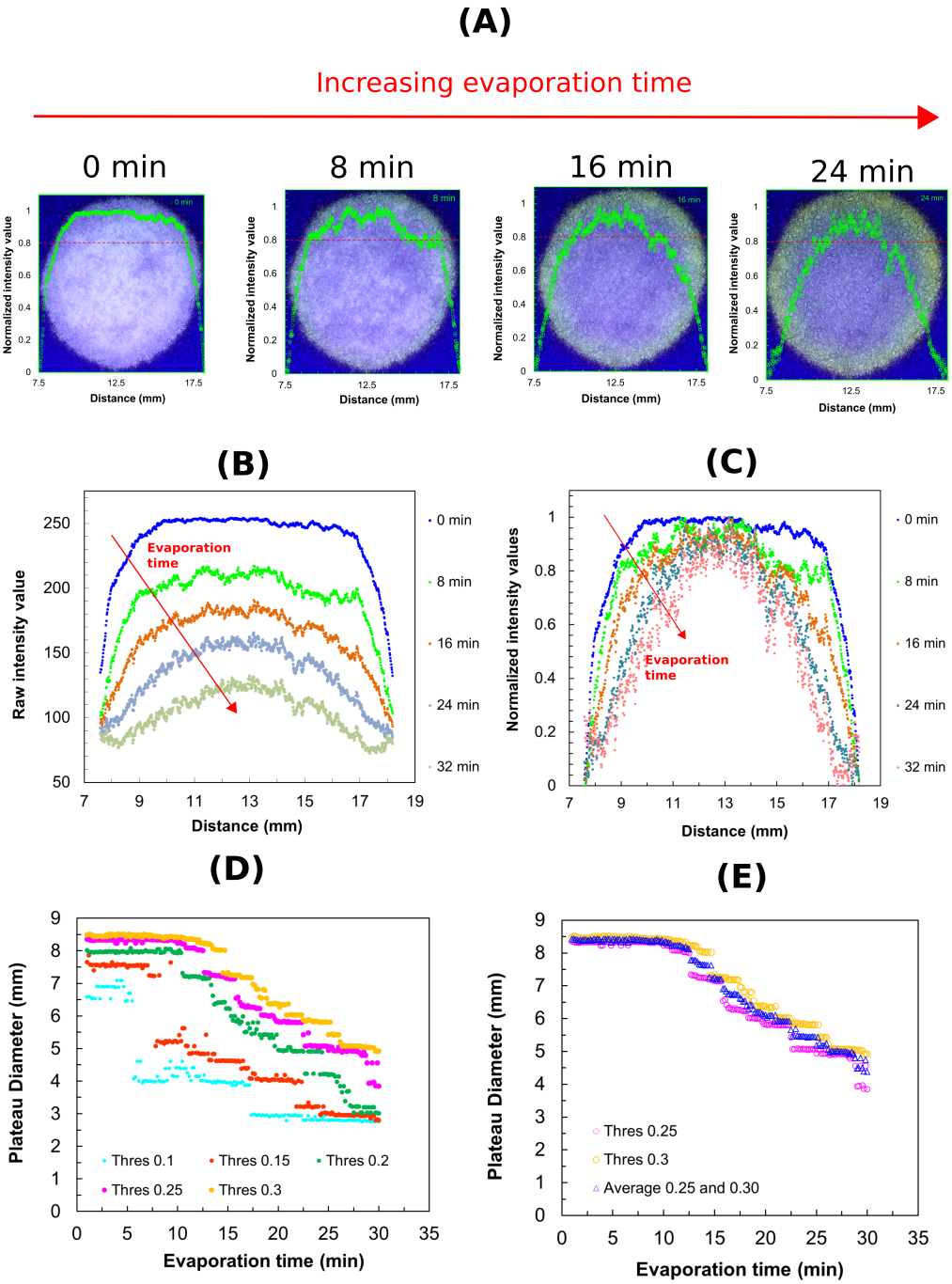

Figure 7.4.: (A) Images captured by the top camera at different times during the test evaporation experiment with the blue channel normalized intensity profile overlapping with it. The dotted red line represents the lower normalized intensity threshold for the plateau region. (B) The raw blue color intensity profiles along the horizontal center line at different times during the evaporation process, (C) Normalized blue color intensity profiles along the horizontal center line at different times during the evaporation process, (D) Variation of the plateau diameter with time as obtained using different threshold values, (E) Final plateau diameter variation obtained by averaging the plateau diameter values obtained at the threshold values 0.25 and 0.30

simultaneously, the color intensity profiles are normalized in order to be able to determine the plateau diameters. The normalized intensities (I_{norm}) are calculated with respect to maximum and minimum intensity values in the intensity profile (I_{max} and I_{min}) as below :

$$I_{norm} = \frac{I - I_{max}}{I_{max} - I_{min}} \tag{7.1}$$

The normalized intensity profiles corresponding to the raw intensity profiles in 7.4(B) are plotted in 7.4(C). The normalized color intensity profiles corresponding to images are shown by plotting them on as an overlap the images in Fig.7.4(A). The plateau diameters could be estimated by determining a certain threshold value (Thres) which helps distinguish the values belonging to the plateau from the rest of the region. Five different threshold values, 0.1, 0.15, 0.2, 0.25 and 0.3 have been considered. The plateau diameters are determined assuming that the normalized intensity values lying between 1 and $(1-Thres)$ belong to the plateau. For any particular image, the final plateau diameter is obtained by averaging the plateau diameters measured along the horizontal and vertical directions.

For the sequence of images obtained for the test case evaporation experiment, the plateau diameters as determined using the different threshold values are plotted in Fig. 7.4(D). It could be observed from Fig. 7.4(D) that the threshold values 0.1 and 0.15 produce inconsistent plateau diameter values with several aberrations. The threshold values 0.2 , 0.25 and 0.3 are found to produce more continuous and realistic plateau diameter values. The initial plateau diameters obtained with the thresholds 0.25 and 0.30 are comparable which indicates that these values are highly suited for this estimation. An average of the plateau diameters obtained for the threshold values 0.25 and 0.3 as shown in Fig. 7.4(E) is therefore used to obtain the final variation of the plateau diameter.

It could be noted from 7.4(E), that in the model evaporation experiment, the plateau diameter remains almost unchanged initially as evaporation proceeds. After a certain point of time, the wetted diameter starts decreasing at a more rapid rate. The initial evaporation phase during which the plateau diameter remains unchanged could be considered analogous to the pinned phase which is typically observed during the evaporation of sessile droplets on flat surfaces wherein the droplet base diameter remains fixed. The reasons underlying the existence of this quasi-pinned evaporation phase have been discussed subsequently in this Chapter.

7.3.2 Analysis of the final stains

The final stain formed on the substrate after evaporation is over is imaged under normal white light both from the top as well as the bottom (Fig.7.5(A) and (B)). The top and bottom view images provide insights into how deposition near the top and bottom layers of the porous substrate look like. The characteristics of the final stain is examined using a methodology similar to that implemented for the analysis of the images of the evaporating area. The intensity profile of the blue color is used to obtain a measure of the distribution of deposition in the final stain as shown in Fig. 7.5(C). In could be identified from the profiles that both the top as well as bottom profiles could be divided into two regions, the central uniform deposition region which appears as a plateau and the peripheral coffee ring stain which appears as a valley. These profiles

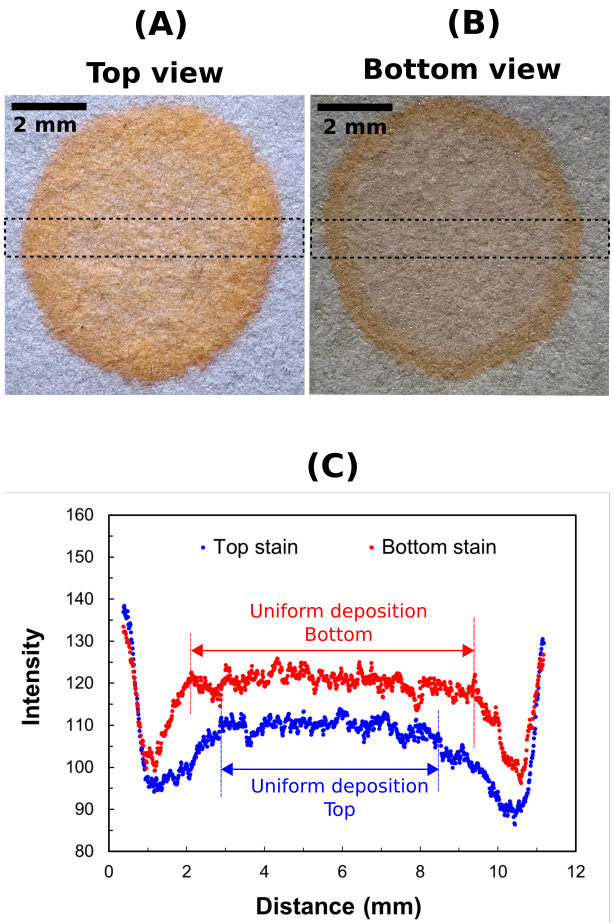

Figure 7.5.: Final stain images formed as observed from the top (A) and bottom (B). Blue color intensity profiles of the top and bottom view images along the center line of the images of the final stain.

enable us to determine the diameter of the uniform deposition region from the top as well as the bottom. From the stains shown in Fig. 7.5(A) and (B), it could be remarked that the top uniform deposition diameter is distinctly smaller than the bottom uniform deposition diameter. This indicates that the peripheral coffee rings as observed from the top are bigger than the coffee rings observed from the bottom.

7.3.3 Analysis of the mass variation data

The measurements made by the analytical balance during evaporation experiment provide the kinetics of liquid mass evaporation. The evaporation kinetics obtained in the sample evaporation experiment (30 mg WE18 vesicle dispersion on Whatman 903) has been shown on Fig. 7.6(A). The evaporation rate at any point of time is obtained by estimating the slopes on the liquid mass variation curve and has been plotted on Fig. 7.6(B). It could be identified from Fig. 7.6(B) that the evaporation rate initially remains approximately constant for a certain period of time indicating that the mass decreases linearly. After a certain point of time, it is observed that the evaporation rate starts diminishing and it decreases continuously until the liquid is completely evaporated.

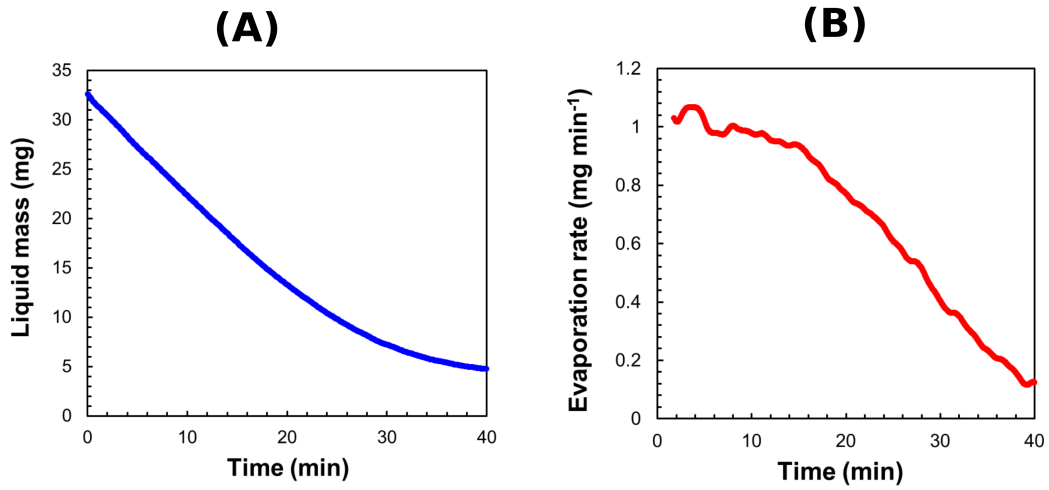

Figure 7.6.: (A) Liquid evaporation kinetics as obtained in the sample evaporation experiment (30 mg WE18 vesicle dispersion on Whatman 903), (B) Variation of the evaporation rate as estimated for the evaporation kinetics data

7.4 Model for liquid evaporation from wetted areas on porous substrates

After the liquid wets and imbibes into the porous substrate, the evaporation process sets forth. The imbibed liquid thereafter acts like a liquid reservoir confined inside the porous substrate from which evaporation occurs. In earlier works, it was hypothesized that evaporation from such liquid filled domains occurs in a manner similar to evaporation from thin sessile droplets as shown schematically in Fig.7.7(A) [147]. When evaporation rate is diffusion-controlled, the distribution of liquid mass evaporation flux (J) along the radius (r) of the liquid droplet is given by [148] :

$$J(r) = \frac{2D(1-H)c_{sat}(T_a)}{\pi\sqrt{(R^2-r^2)}} \tag{7.2}$$

where, R is total radius of the thin droplet, H is the relative humidity far away from the droplet, D is the diffusion coefficient of the vapor in the atmosphere, $c_{sat}(T_a)$ is the saturation vapor concentration which is dependent on the temperature T_a.

The above equation can be further simplified when it is applied to the evaporation of wetted areas formed on the porous substrate in our experiments as shown in Fig. 7.7(B). As the experiments have been carried out in an atmosphere of pure nitrogen inside a Glovebox, the relative humidity, H in Eq. 7.2, can be set to zero :

$$J(r) = \frac{2Dc_{sat}(T_a)}{\pi\sqrt{(R^2-r^2)}} \tag{7.3}$$

In order to describe the variation of the evaporation flux along the radius of wetted spot, the above equation is rewritten as :

$$J(r) = \frac{J_O}{\sqrt{1-(r/R)^2}} \tag{7.4}$$

where, $J_O = \frac{2Dc_{sat}(T_a)}{\pi R}$. The variation of the evaporation flux along the radius of the wetted spot as given by Eq. 7.4 is plotted in Fig. 7.7(C). It can be identified from this plot that the evaporation flux near the periphery of the wetted spot is much higher than at the center of the spot.

The total mass evaporation rate from the wetted area can be estimated by integrating the above evaporation flux over the entire area of the thin droplet :

$$-\frac{dM}{dt} = 4RDc_{sat}(T_a) \tag{7.5}$$

It can be observed from the above equation that the mass evaporation rate is predicted to be linearly dependent on the radius of the wetted area.

7.5 Results and Discussions

7.5.1 Initial evaporation rates from wetted areas

The theoretical model described in the last section predicts that the mass evaporation rate of the wetted spots is linearly dependent on the diameter of the wetted spots. This could be validated by comparing the initial evaporation rates obtained in the experiments with those predicted by Eq. 7.5. Evaporation experiments are carried out using both the porous filter paper substrates, Whatman 903 and Sartorius 388. Different masses of both water as well as the complex liquid, WE18 vesicle dispersion are used. The mass variation during evaporation obtained using the analytical balance provides us information about the evaporation rates from the wetted areas formed on the porous substrates. As an example for the obtained experimental data, the mass variation for different initial masses of WE18 vesicle dispersion on Whatman 903 has been plotted on Fig. 7.8. Each experiment was repeated twice to ensure the reproducibility of the experiments.

The wetted area diameters obtained with water and WE18 vesicle dispersion on Whatman 903 and Sartorius 388 are plotted against the square root of liquid masses in Fig. 7.9(A) and (B), respectively. Due to the lower thickness of Sartorius 388, the diameters of the wetted areas formed on Sartorius 388 are larger than that on Whatman 903.

As given by Eq. 7.5, the evaporation rate is linearly dependent on the saturation vapor concentration which depends on the temperature. On the other hand, the other variable in Eq. 7.5, the diffusion coefficient, D, can be reasonably assumed to remain constant with temperature. In the evaporation experiments, the temperature varies between 25 and 30 °C, and therefore

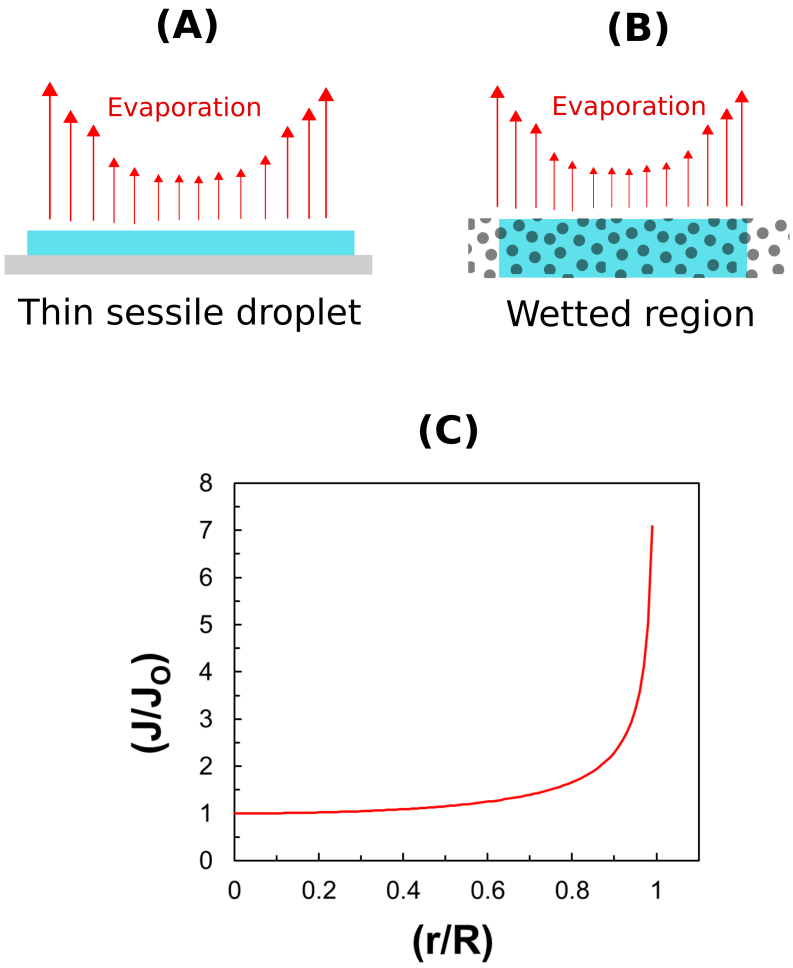

Figure 7.7.: (A) Liquid evaporation from a thin liquid droplet, (B) Liquid evaporation from the wetted region formed on the porous substrate, (C) Variation of the evaporation mass flux along the radius of the wetted region as predicted by Eq.7.4

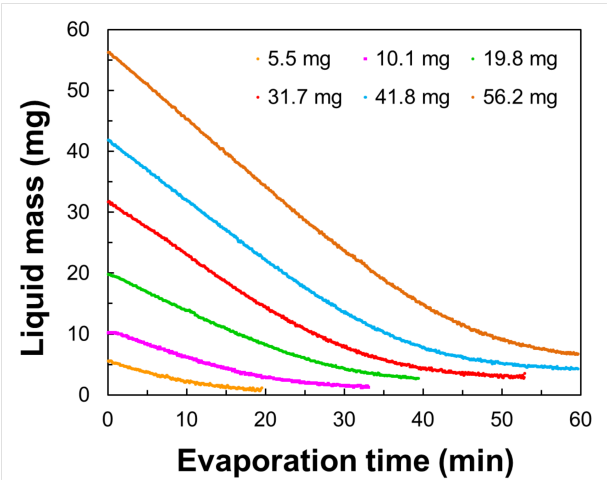

Figure 7.8.: Mass variation during evaporation of different initial droplet masses of WE18 vesicle dispersion on Whatman 903 filter paper

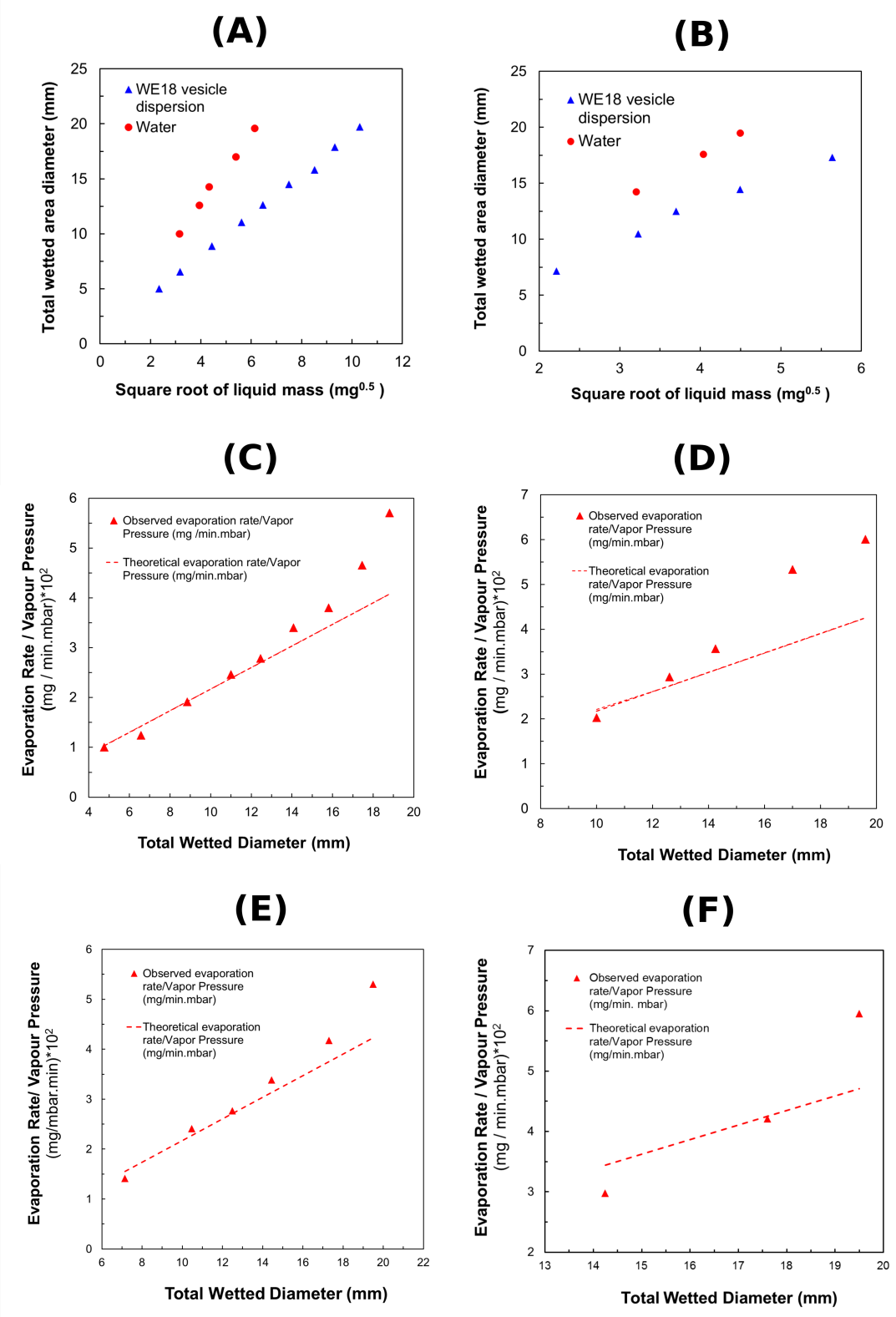

Figure 7.9.: Total initial wetted diameters obtained on Whatman 903 (A) and Sartorius 388 (B) with different masses of both the WE18 vesicle dispersion and water. Variation of the initial evaporation rates with the total wetted diameters on Whatman 903 (WE18 vesicle dispersion (C) and water (D)) and Sartorius 388 (WE18 vesicle dispersion (E) and water (F))

dividing the obtained evaporation rate with the saturation vapor pressure which is proportional to the saturation vapor concentration provides a parameter which is comparable for different experiments conducted even at different temperatures.

The initial evaporation rates divided by the respective saturation vapor pressures obtained in the experiments for the evaporation of WE18 vesicle dispersion and water on Whatman 903 are plotted against their initial total wetted diameters on Fig. 7.9(C) and (D), respectively. The results obtained with Sartorius 388 of WE18 vesicle dispersion and water has been plotted against the wetted area diameters on Fig. 7.9(E) and (F), respectively. The theoretical variation is given by Eq. 7.5 has also been plotted on Fig. 7.9(C)-(F).

As a general observation from Fig. 7.9(C)-(F), it is identified that the experimental evaporation rates match well with the theoretical prediction at wetted diameters below 12-14 mm. For larger wetted diameters, the experimentally measured evaporation rates are found to exceed the theoretically predicted values.

7.5.2 Simultaneous plateau diameter and liquid mass variation during evaporation

The experimental data obtained for the variation of the wetted area plateau diameter and the mass evaporation rate with time are plotted on Fig. 7.10 for different liquids and substrates. The results for evaporation of the WE18 vesicle dispersion and water on Whatman 903 are shown on Fig. 7.10(A) and (B), respectively. The results for the evaporation of the same two liquids on Sartorius 388 are plotted on Fig. 7.10(C) and (D), respectively. The mass of WE18 vesicle dispersion and water used for these evaporation experiments was 20 mg and 15 mg, respectively.

It is observed from Fig. 7.10(A) that in the evaporation of WE18 vesicle dispersion on Whatman 903, both the plateau diameter as well as the evaporation rate remain relatively fixed or vary marginally during the initial stages of evaporation. After a certain time, the plateau diameter starts decreasing more rapidly. Thereafter, after some more time has elapsed the evaporation rate starts diminishing as well. It has been described in the last section that the evaporation rate is linearly related to the diameter of the evaporating spot. Therefore, if the plateau region is the only part of the wetted area contributing to evaporation, it should start decreasing as soon as the wetted diameter starts diminishing. However, in the experiments, It is important to note that a certain time gap exists between the times at which the plateau diameter and the evaporation rates start decreasing at much faster rates.

In the evaporation of water on Whatman 903 (see Fig. 7.10(B)), it is observed that the plateau diameter starts decreasing at a faster rate as soon as evaporation process starts. As the total wetted diameter formed on Whatman 903 by water is much greater than that formed by the complex liquid, it can be suggested that the height upto which the porous substrate is filled with water is lower for water than that for the complex liquid. This could be the possible reason underlying the observed earlier fast reduction in wetted plateau diameter and is explained with the help of a model in the next section. The evaporation rate, however, similar to that observed in the complex liquid, starts decreasing after some more time has elapsed.

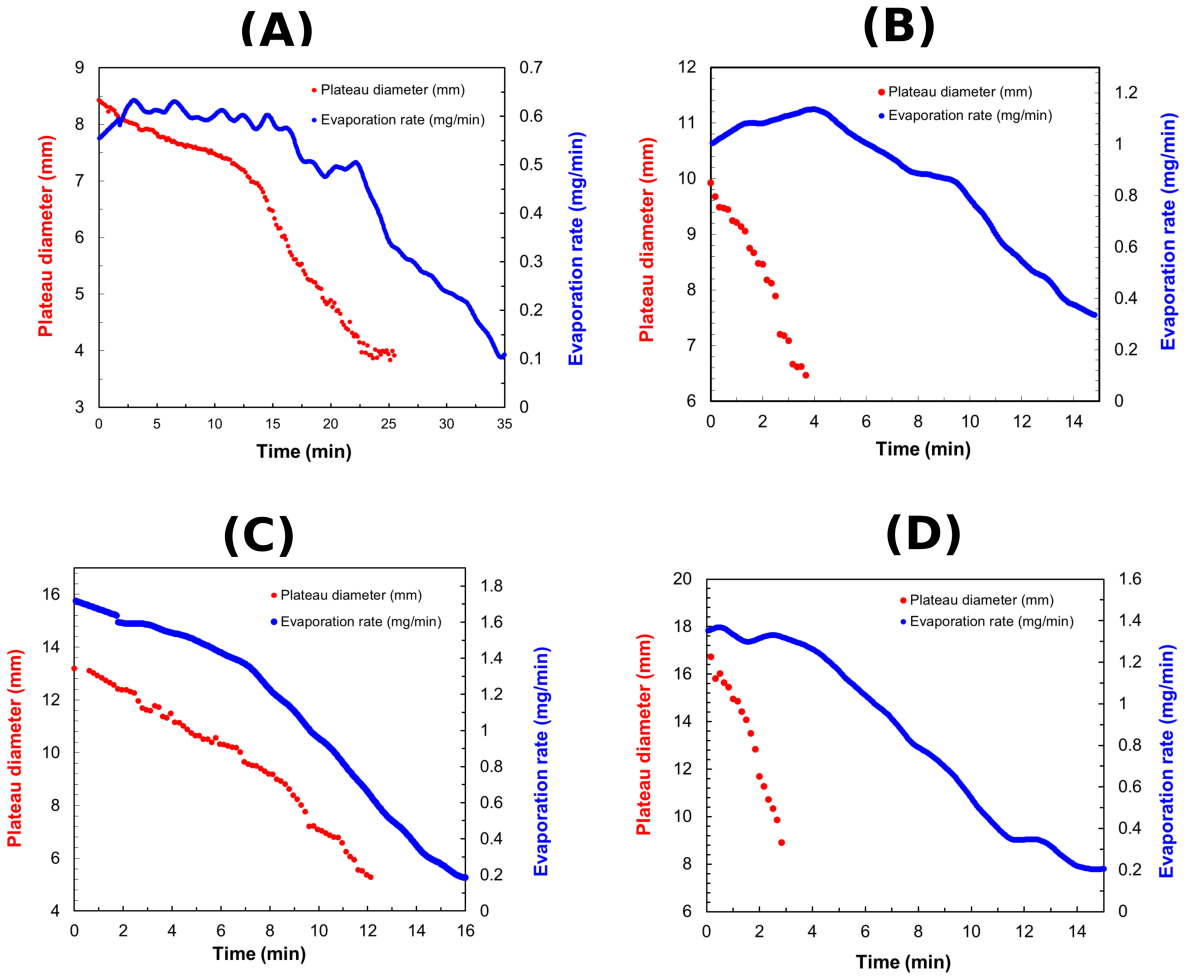

Figure 7.10.: Variation of the plateau diameter and evaporation rate with evaporation time for on Whatman 903 (WE18 vesicle dispersion (A) and Water (B)) and Sartorius 388 (WE18 vesicle dispersion (C) and Water (D))

It is observed from Fig. 7.10(C) that during the evaporation of WE18 vesicle dispersion on Sartorius 388 both the plateau diameter and the evaporation rates start decreasing sharply much earlier than in the case of Whatman 903. As the main difference between the two porous substrates is their thickness, the observed difference indicates that the porous substrate thickness also plays a significant role in determining how evaporation of the wetted spots proceeds. These observations are explained with the help of the evaporation model described in Section 7.5.4.

7.5.3 Characteristics of coffee ring stains formed on porous substrates

The non-volatile dispersed ingredient of the complex liquid is left deposited on the porous substrate when the bulk liquid is evaporated. Due to the high evaporation rate at the periphery of the wetted spot, most of the dispersed ingredients are deposited in this region. The final deposition pattern therefore resembles the typical coffee rings which are formed when a colloidal dispersion droplet evaporates on a solid surface. The characteristics of the formed stains were examined from both, the top as well as the bottom. The diameter of the region in which uniform deposition is observed was measured. The diameters of the total wetted area, the uniform deposition area (top and bottom), and the plateau area of the wetted area obtained

with different masses of the complex liquid on Whatman 903 are plotted on Fig. 7.11(A). Taking the difference between the total wetted diameter and the uniform deposition diameter provides a measure of the width of the coffee rings formed at the top and bottom of the porous substrate. Similarly, the difference between the total wetted diameter and the initial plateau diameter provides the width of the unsaturated region filled during secondary radial imbibition of the liquid. The widths of the coffee rings (top and bottom) and the unsaturated zone obtained for different masses of the complex liquid on Whatman 903 are shown on Fig. 7.11(B).

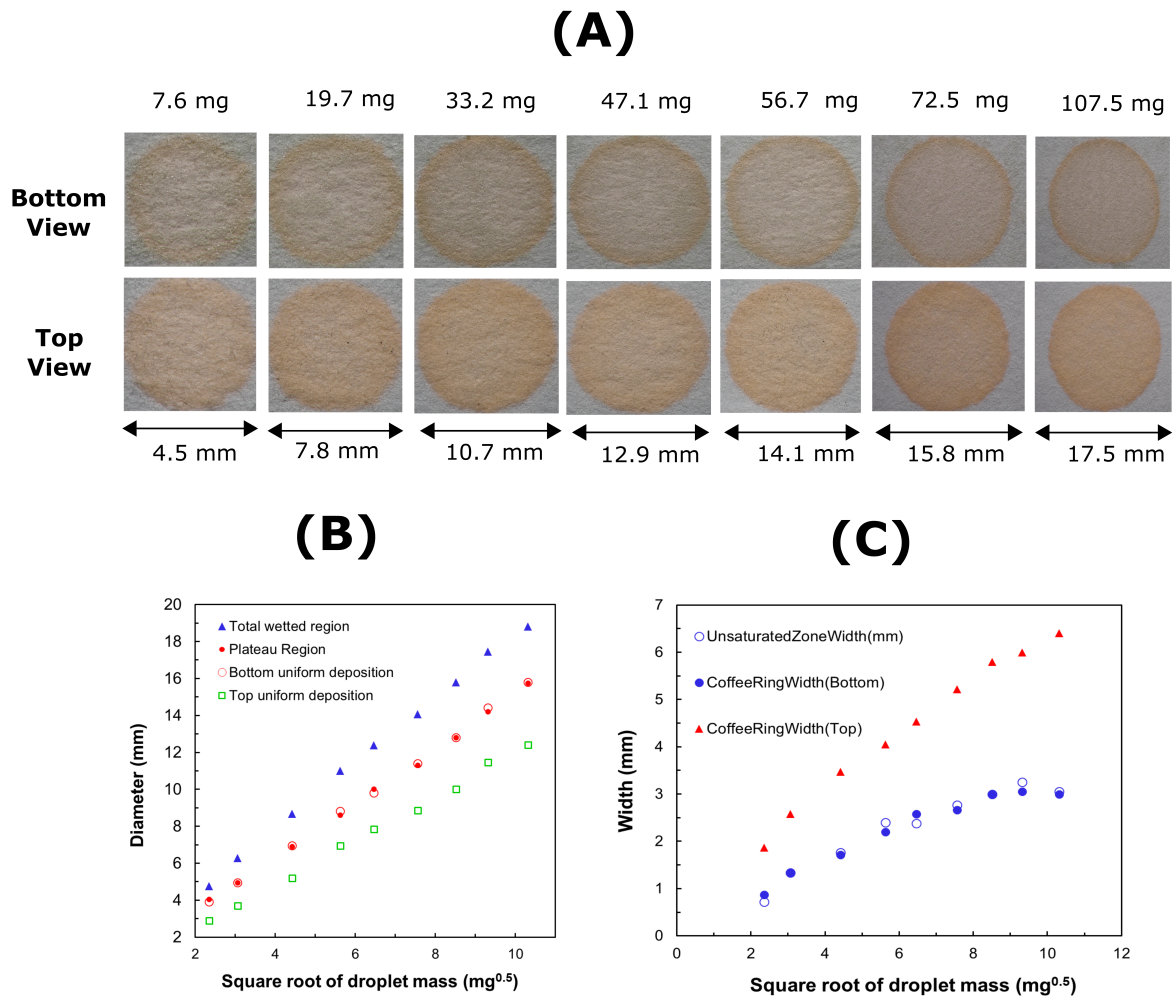

Figure 7.11.: (A) Top and bottom view images of the final stains formed on Whatman 903 with droplets of different initial masses of the complex liquid (WE18 vesicle dispersion), (B) Diameters of the total wetted area, plateau diameter, diameter of the uniform deposition region (observed from top and bottom) obtained with different initial masses of the WE18 vesicle dispersion, (C) Widths of the coffee rings (top and bottom), and the unsaturated part of the wetted area

The main observation from Fig. 7.11(A) is that the diameter of the plateau region corresponds very well the diameter of the uniform deposition region as observed from the back. The same is also identifiable from Fig. 7.11(B) where the width of the back coffee ring is found to coincide with the width of the unsaturated zone in the initial wetted area. This indicates that the final stain formed on the porous substrate is intrinsically related to the characteristics of the wetted

area formed initially. Furthermore, it is observed that the width of the bottom coffee ring initially increases with increasing droplet mass and thereafter does not increase beyond a certain value. On the other hand, the top coffee ring width does not reach saturation and keeps increasing with the droplet mass. These characteristics of the final stain could be explained with the help of schematic model proposed in the subsequent section.

7.5.4 Schematic model for evaporation and coffee ring formation from wetted areas

Based on the observations reported in the last two sections, a model is conceptualized to describe how evaporation of the wetted spot formed on the porous substrate proceeds and how the coffee ring effect is eventually formed. The conceptualized model describing the evaporation process has been shown schematically on Fig. 7.12.

The evaporation process takes effect after the relatively faster wetting process is over. The initial wetted area has two parts, the central region which is formed during the primary wetting phase and appears as a plateau in the color profile. Additionally, there exists a peripheral region which is filled via secondary radial liquid penetration. The extent of liquid filling in the peripheral region is lower than that in the plateau region. The wetted area is represented schematically on Fig. 7.12(A). In the first phase of evaporation, the diameter of the total wetted area and the plateau region remains constant. In this phase, the evaporation rate which is dependent on the diameter of the total wetted area also remains constant. The mass reduction due to evaporation thus only leads to reduction in the height of liquid filling in the wetted area. In this evaporation phase, most of the evaporation occurs from the periphery of the wetted area due to the high evaporation rate. The bulk liquid flows from the center of the wetted area towards the periphery to supply liquid to maintain the high evaporation rate.

As evaporation proceeds, the height of liquid filling in the center of the wetted area keeps decreasing. Simultaneously, the rate at which liquid is supplied from the center of the wetted area to the periphery also reduces. A stage is therefore reached at which the high evaporation rate at the periphery cannot be sustained by bulk liquid flow from the center. Thereafter, further evaporation leads to a reduction in the plateau diameter as is shown schematically in Fig 7.12(B). The receding plateau, however, leaves behind water and the total wetted diameter does not decrease. As a result, the evaporation rate remains constant over this evaporation stage. Eventually, a stage is reached when the evaporation from periphery cannot be sustained even by the leftover liquid and the evaporation rate starts decreasing. The decreasing evaporation rates indicates that the total wetted area starts diminishing and the periphery starts drying out leading to complete evaporation as shown in Fig. 7.12(C).

The above described model can be used to explain the main observations in Fig. 7.10. Firstly, the observed difference between the evaporation of the complex liquid and that of water on Whatman 903 can be explained as follows. As the total wetted area obtained with water is greater than that with the complex liquid, the level of liquid filling in the initial wetted area is lower for water than for the complex liquid. Therefore, the phase when the plateau diameter starts decreasing ensues much earlier with water than that with the complex liquid. Similarly when the used porous substrate Sartorius 388 is used, the wetted area is larger because of the lower thickness of the substrate. Even in this case, the liquid flow rate from the center of the wetted area to periphery is lower and cannot sustain the high evaporation rate at the periphery.

As a result the plateau diameter starts diminishing much earlier than that in the case of Whatman 903.

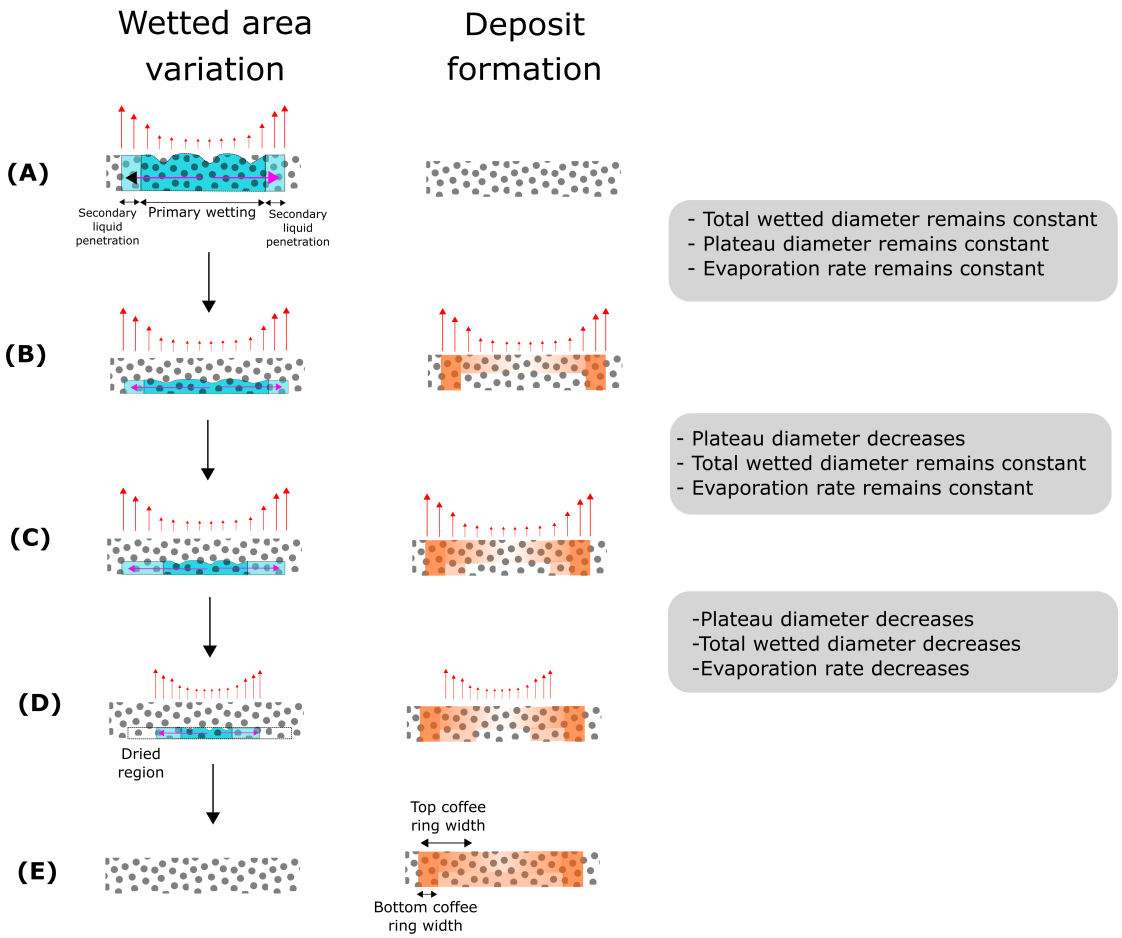

Figure 7.12.: Schematic model describing how the wetted area and the stain deposit evolves during the evaporation process

The characteristics of the final stain could be explained by considering how colloids are deposited during the course of evaporation. Based on the evaporation mechanism proposed in the above paragraphs, the evaporation process could be divided into two phases : (i) the constant wetted area phase which occurs initially (A to C in Fig. 7.12), and (ii) the reducing wetted area mode which occurs towards the end of evaporation (C to E in Fig. 7.12). The constant wetted area phase of evaporation is analogous to the pinned evaporation phase of sessile droplets, in which liquid flow from the center of the wetted area to the periphery carries the dispersed ingredients with it which are deposited at the pinned evaporation site. The coffee ring deposits as observed from the back are formed in this quasi-pinned phase of evaporation during which most of the evaporation occurs in the pinned zone i.e. the peripheral unsaturated zone of the wetted area. The coffee ring as observed from the top corresponds to the width of the highly evaporating periphery as described in Section 7.4. As the width of this highly evaporation region increases linearly with the total wetted diameter, the coffee ring width as observed from the top increases almost linearly with the square root of droplet mass as shown in Fig. 7.11(C). The evolution of

deposition of colloids on the porous substrate has been shown in Fig. 7.12.

7.5.5 Influence factors in the final stain formation

7.5.5.1 Effect of concentration

The original vesicle dispersion containing around 10% lipids is diluted with water to different concentration levels. Dispersions with concentration levels of 25%, 50%, 75% and 100% with respect to the starting dispersion are prepared. 30 μl droplets of these dispersions were placed on the Whatman 903 porous substrate. The coffee ring stains obtained at different concentration levels were compared to understand how the vesicle concentration influences coffee ring formation as shown in Fig. 7.13.

One distinct observation is that the intensity of coffee rings decreases as the concentration of the initial dispersion was reduced. At the concentration level of 25 %, the coffee rings are so weak that it is difficult to identify the ring. Comparing the coffee rings obtained at the concentration of 50%, 75% with the original dispersion (100%) shows that the intensity of obtained coffee rings increases with concentration which also follows directly from the proposed schematic model for coffee ring formation.

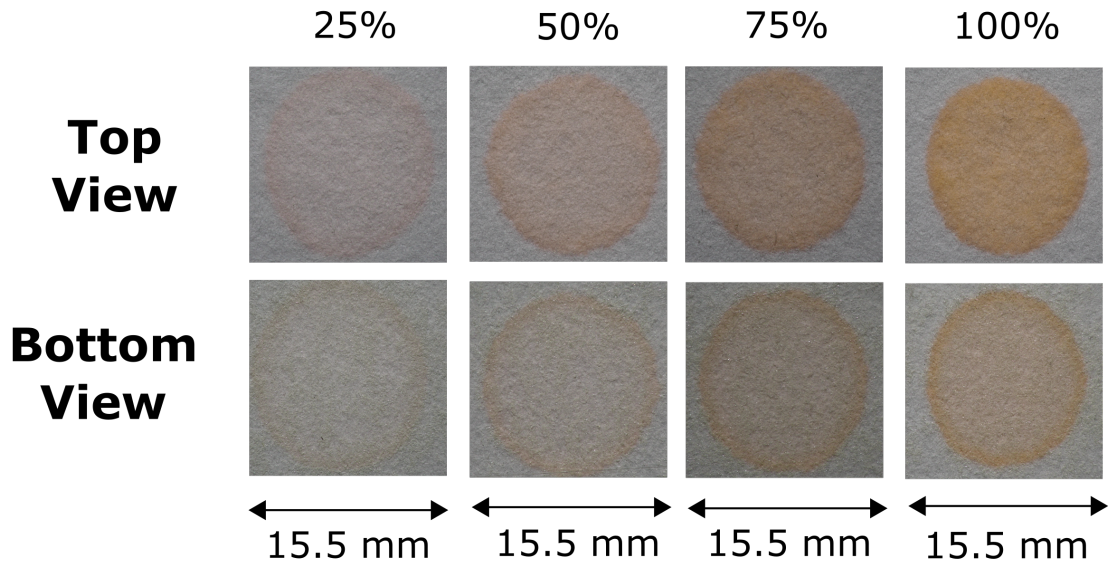

Figure 7.13.: Coffee ring stains formed on the Whatman 903 porous substrate with 30 μl droplets of WE18 vesicle dispersion at different concentration levels with respect to the original dispersion

7.5.5.2 Effect of pore sizes of porous substrate

Coffe ring stains obtained on different grades of Sartorius filter papers, namely 388, 389 and 390, with different pore sizes, were compared to get an insight into the effect of pore sizes on coffee ring formation. The pore sizes of these porous substrates are enlisted on Table 2.2.

The top and bottom views of the stains obtained with 20 μl of WE18 vesicle dispersion on these substrates are shown in Fig.7.14. While a distinct and strong coffee ring is obtained on the filter paper Sartorius 388 with the highest pore size, the coffee ring intensity decreases with decreasing pore size and no distinct coffee ring is obtained on the substrate, Sartorius 390, with the smallest pore size.

The above observation could be explained using the mechanism of coffee ring formation on porous substrates that has been outlined in Fig.7.14. The formation of coffee rings occurs due to the flow of liquid from the center of the wetted region towards its periphery. When the porous substrate has large pores, liquid flows from the center towards the periphery with less resistance leading to more intense coffee rings. On the other hand, on a porous substrate with smaller pores the radial outwards flow of the liquid would be highly supressed leading to weaker coffee rings.

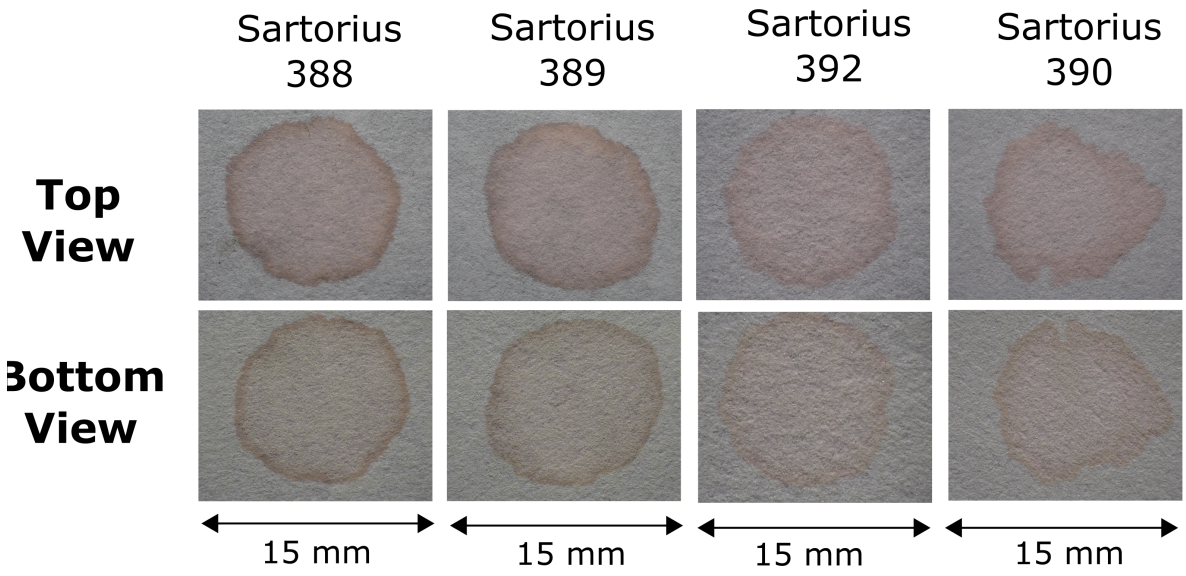

Figure 7.14.: Coffee ring stains formed on porous substrates with different pore sizes with 20 μl droplets of WE18 vesicle dispersion

7.5.5.3 Effect of temperature

The temperature of the underlying substrate is an important factor that could influence the formation of coffee rings. In the case of coffee ring formation on porous substrates, the substrate temperature could not only influence the rate of liquid evaporation but also the extent of initial spreading and imbibition of the liquid on the porous substrate. In order to investigate the effect of temperature on coffee ring formation, 30 μl droplets of the WE18 vesicle dispersion were placed on Whatman 903 porous substrates maintained at temperatures of 10°C, 30°C and 50°C using a Peltier-Element. The top and bottom views of the final stains obtained at the different temperatures are shown on Fig. 7.15.

It is observed that the diameter of the wetted area is lower at 50 ^{o}C than at 10°C. The effect of substrate temperature on the wetted diameter could be explained by considering the dynamics

of the secondary liquid penetration described in Chapter 6. When the substrate temperature is increased, the evaporation rate also increases. This leads to greater evaporation and faster increase in the colloids concentration close to the spreading liquid front which negatively influences the secondary liquid penetration. This may lead to the secondary liquid penetration coming to a stop earlier than that at lower temperature. Therefore, at different substrate temperatures the size of the primary wetted area would be the same for same droplet volume. However, the extent of secondary liquid penetration is lower at higher temperature and vice-versa. As far as the widths of the coffee rings are concerned, they are also found to be narrower at higher temperature. This is in agreement with the earlier observations which relate the coffee ring widths with the width of the secondary liquid penetration zone.

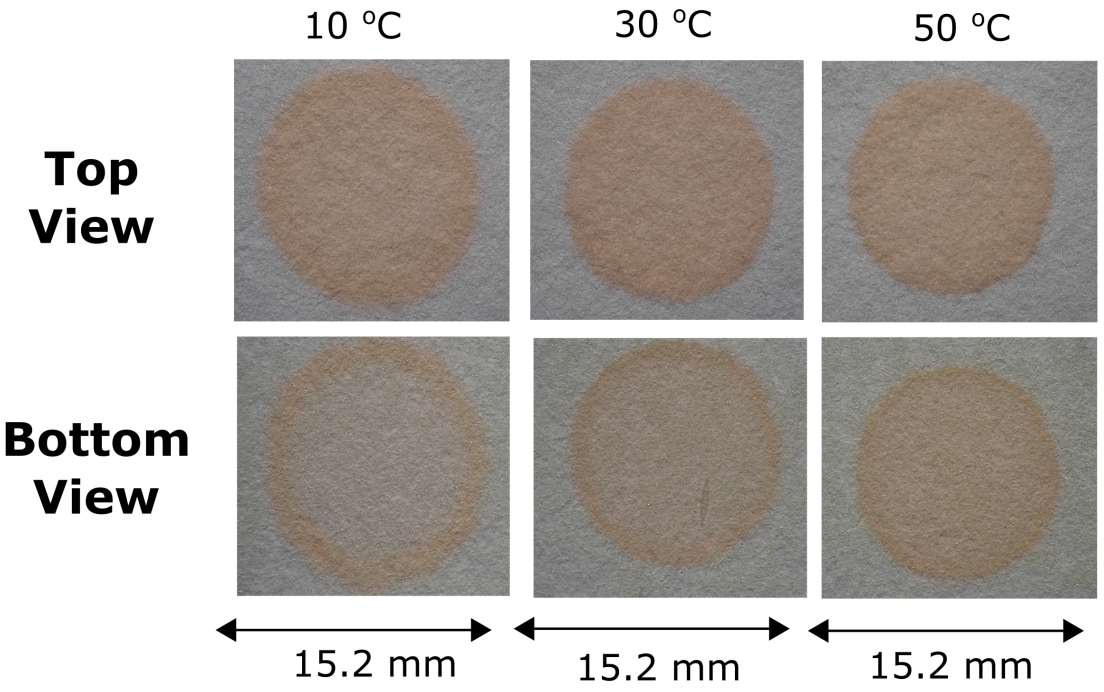

Figure 7.15.: Coffee ring stains formed on Whatman 903 with 30 μl droplets of WE18 vesicle dispersion at different temperatures

7.6 Summary

In this Chapter, the formation of coffee rings on porous substrates has been investigated. The droplets were placed on the porous substrate, and the evaporation process which ensues after droplet wetting and imbibition is completed was observed from the top. The mass rate of evaporation was simultaneously characterized using an analytical balance. A combination of the two measurement techniques is used to obtain insights into the mechanism underlying the coffee ring formation. It is identified that the evaporation process is divided into two phase : (i) the constant wetted area phase which occurs initially, and (ii) the constant wetted height phase which occurs towards the end of evaporation. It is found that the coffee ring deposits are formed in the initial constant wetted area phase of the evaporation process. Furthermore, the trends

in variation of size of the coffee rings with different parameters such as droplet size, colloidal concentration, and substrate porosity are investigated and explained.

8 Conclusions and Outlook

In this PhD thesis, the interaction of complex liquids which porous substrates involving processes such as colloidal deposition, liquid wetting, and coffee ring stain formation has been investigated using various approaches and experimental techniques. Cationic vesicle dispersions which form an important ingredient of several homecare and personal care products are used as model complex liquids for the investigations. Anionic cellulose fiber based substrates such as cotton fibers, cotton yarns and cellulose fiber filter papers were used as porous substrates. The aim of these investigations is to gain new insights into various important aspects of these interaction processes which are still not well understood. A better understanding of these processes will help us design more effective complex liquid formulations and choose optimum treatment conditions to achieve better results in real-life applications.

The deposition of cationic vesicles on anionic substrates is studied using streaming potential measurements to characterize the apparent zeta potentials of substrates. As the applicability of this technique to complex sample geometries such as fiber plugs is not well established, a new theoretical model is developed in Chapter 3 to describe streaming potential and streaming current generation in complex geometry samples such as fiber plugs which establishes that the qualititative validitiy of the Helmholtz-Smoluchowski equation.

The deposition of cationic vesicles on non-porous and porous anionic cellulose substrates is investigated in Chapter 4. It is shown that the mechanism of cationic vesicle deposition is highly dependent on vesicle size, vesicle shape, polydispersity, and substrate roughness. Vesicle deposition behavior on smooth surfaces (viscose fibers) is governed by the contrasting surface mobility characteristics of the two vesicle types with smoothly-shaped and round WE 15 vesicles being capable of moving, and non-spherical and sharp-edged DEEDMAC vesicles being immobilized upon deposition. For deposition on rough surfaces (cotton fibers), the surface mobility of both DEEDMAC and WE 15 vesicles is suppressed, and hence similar deposition behavior is observed for both the vesicle types.

In Chapter 5, the permeation and deposition of cationic vesicles on anionic porous substrates, namely porous cotton yarns in investigated. The phase behavior of lipid bilayers constituting the vesicles and the presence of electrolyte in the bulk liquid are found to be the important parameters influencing the process. While the deposition of vesicles with solid-gel phase bilayers (DEEDMAC) is found to be confined to the yarn periphery, the deposition of vesicles with liquid-crystalline phase bilayers (WE 15) occurs quite homogeneously across the yarn cross-section. Additionally, the presence of inter-particle electrostatic interactions which could be tuned by adding electrolyte (salt) to the bulk liquid is found to influence the deposition of both the vesicle types. The effect of these parameters on the process is explained in terms of their effect on the ratio of colloidal deposition and permeation rates.

In Chapter 6, the simultaneous spreading and imbibition of vesicle dispersion droplets on porous cellulose fiber filter papers. It is shown that the spreading behavior of vesicle dispersions on

porous substrates is strongly influenced by the thickness of the porous substrate as well as the phase behavior of the lipid bilayers constituting the vesicles. Droplet spreading behavior is of the complete wetting type on Whatman 903 which has a thickness of 500 μm, while it is of the partial wetting type on Sartorius 388 which has a thickness of 210 μm. On both the filter papers, the spreading kinetics of the liquid droplets containing WE18 vesicles with solid-gel phase bilayers is slower than that of liquid droplets containing WE15 vesicles with liquid-crystalline phase bilayers. It is shown that the faster spreading kinetics of WE15 vesicles is due to its lower viscosity which results in a faster rate of liquid penetration into the porous substrate via imbibition.

In Chapter 7, the formation of coffee rings on porous substrates has been investigated. The droplets were placed on the porous substrate, and the evaporation process was observed from the top. The rate of evaporation was simultaneously characterized using an analytical balance. A combination of the two measurement techniques is used to obtain insights into the mechanism underlying the coffee ring formation. It is identified that the evaporation process could be divided into two phases : (i) the constant wetted area phase which occurs initially, and (ii) the constant wetted height phase which occurs towards the end of evaporation. It is found that the coffee ring deposits are formed in the initial constant wetted area phase of the evaporation process. Furthermore, the trends in variation of size of the coffee rings with different parameters such as droplet size, colloidal concentration, and substrate porosity were investigated and explained.

8.1 Outlook

The work carried out in this thesis advances the present understanding of the interaction of complex liquid formulations with porous substrates. However, the findings of this thesis also give rise of several new questions which could be addressed in future works.

In Chapter 3, a new theoretical model has been proposed to describe the apparent zeta potential characterization of solid substrates via streaming potential measurements. The new model describes the generation of streaming potential in non-ideal sample geometries such as non-uniform capillaries and porous substrates. However, the fundamental microscale relationship proposed in this work which has been used to establish the relationships between the applied pressure difference, sample geometry and the developed streaming potential could also be extended to other electrokinetic phenomena such as streaming current generation and electro-osmosis which are of significance.

In Chapter 4 and 5, the deposition of cationic vesicles on non-porous and porous anionic substrates, respectively, has been investigated. The streaming potential measurements which form the main experimental technique used for these investigations allow us to characterize the zeta potential of the substrates and provide us valuable insights into the process mechanism. However, the conclusions drawn based on these measurements are indirectly derived. Hence, direct visualization of the in-situ permeation and deposition of such vesicles into porous substrates could help confirm the conclusions. This could potentially be carried out using 3D-confocal microscopy of the deposition process, wherein the evolution of adsorption densities could be visualized inside a refractive index-matched porous substrate.

In Chapters 6 and 7, the wetting of porous substrates by vesicle dispersion droplets and subsequent formation of the coffee ring effect after evaporation is described. The present study, however, does not provide clear insights into the microscale picture of the process. In future works, the focus could be on 3D-visualization of liquid redistribution during evaporation and particle deposition leading to coffee ring formation. Furthemore, strategies could be devised to control or modulate the formation of coffee rings on porous substrates.

Bibliography

[1] Enrico Gerace, Agnese Veronesi, Gianmario Martra, Alberto Salomone, and Marco Vincenti. Study of cocaine incorporation in hair damaged by cosmetic treatments. *Forensic Chemistry*, 3:69 – 73, 2017. ISSN 2468-1709. doi: http://dx.doi.org/10.1016/j.forc.2017.02.004. URL http://www.sciencedirect.com/science/article/pii/S2468170916300947.

[2] Peter Sjövall, Tanja M. Greve, Susanne K. Clausen, Kristian Moller, Stefan Eirefelt, Bjorn Johansson, and Kim T. Nielsen. Imaging of distribution of topically applied drug molecules in mouse skin by combination of time-of-flight secondary ion mass spectrometry and scanning electron microscopy. *Analytical Chemistry*, 86(7):3443–3452, 2014. doi: 10.1021/ac403924w.

[3] Gabriel Lenk, Jonas Hansson, Olof Beck, and Niclas Roxhed. The effect of drying on the homogeneity of dbs. *Bioanalysis*, 7(16):1977–1985, 2015. doi: 10.4155/bio.15.135. URL https://doi.org/10.4155/bio.15.135. PMID: 26327179.

[4] Roland JW Meesters and Gero P Hooff. State-of-the-art dried blood spot analysis: an overview of recent advances and future trends. *Bioanalysis*, 5(17):2187–2208, 2013. doi: 10.4155/bio.13.175. URL https://doi.org/10.4155/bio.13.175. PMID: 23962253.

[5] Azadeh Nilghaz, Liyuan Zhang, and Wei Shen. Coffee stains on paper. *Chemical Engineering Science*, 129:34–41, 2015.

[6] Ulrich Tallarek, Erdmann Rapp, Heiner Sann, Udo Reichl, and Andreas Seidel-Morgenstern. Quantitative study of electrokinetic transport in porous media by confocal laser scanning microscopy. *Langmuir*, 19(11):4527–4531, 2003. doi: 10.1021/la034183p. URL http://dx.doi.org/10.1021/la034183p.

[7] Andrew T. Horvath, A. Elisabet Horvath, Tom Lindström, and Lars Wågberg. Adsorption of highly charged polyelectrolytes onto an oppositely charged porous substrate. *Langmuir*, 24 (15):7857–7866, 2008. doi: 10.1021/la800093m. URL http://dx.doi.org/10.1021/la800093m. PMID: 18581999.

[8] Andrew T. Horvath, A. Elisabet Horvath, Tom Lindström, and Lars Wågberg. Adsorption of low charge density polyelectrolytes to an oppositely charged porous substrate. *Langmuir*, 24(13):6585–6594, 2008. doi: 10.1021/la800274w. URL http://dx.doi.org/10.1021/la800274w. PMID: 18507419.

[9] V.M. Starov, S.R. Kostvintsev, V.D. Sobolev, M.G. Velarde, and S.A. Zhdanov. Spreading of liquid drops over dry porous layers: Complete wetting case. *Journal of Colloid and Interface Science*, 252(2):397 – 408, 2002. ISSN 0021-9797. doi: https://doi.org/10.1006/jcis.2002.8450. URL http://www.sciencedirect.com/science/article/pii/S002197970298450X.

[10] Tzu Chieh Chao, Omid Arjmandi-Tash, Diganta B. Das, and Victor M. Starov. Spreading of blood drops over dry porous substrate: Complete wetting case. *Journal of Colloid and Interface Science*, 446:218 – 225, 2015. ISSN 0021-9797. doi: https://doi.org/10.1016/j.jcis.2015.01.054. URL http://www.sciencedirect.com/science/article/pii/S0021979715001009.

[11] Bronwyn Jean Battersby, Rudo Grimm, Stefan Huebner, and Gregor Cevc. Evidence for three-dimensional interlayer correlations in cationic lipid-dna complexes as observed by cryo-electron microscopy. *Biochimica et Biophysica Acta (BBA) - Biomembranes*, 1372(2):379 – 383, 1998. ISSN 0005-2736. doi: https://doi.org/10.1016/S0005-2736(98)00062-5. URL http://www.sciencedirect.com/science/article/pii/S0005273698000625.

[12] Abhijeet Kumar, Laurent Gilson, Franziska Henrich, Verena Dahl, Jochen Kleinen, Tatiana Gambaryan-Roisman, and Joachim Venzmer. Intact deposition of cationic vesicles on anionic cellulose fibers: Role of vesicle size, polydispersity, and substrate roughness studied via streaming potential measurements. *Journal of Colloid and Interface Science*, 473:152 – 161, 2016. ISSN 0021-9797. doi: https://doi.org/10.1016/j.jcis.2016.04.004. URL http://www.sciencedirect.com/science/article/pii/S0021979716302120.

[13] Abhijeet Kumar, Verena Dahl, Jochen Kleinen, Tatiana Gambaryan-Roisman, and Joachim Venzmer. Influence of lipid bilayer phase behavior and substrate roughness on the pathways of intact vesicle deposition: A streaming potential study. *Colloids Surf., A*, 521: 302 – 311, 2017. ISSN 0927-7757. doi: https://doi.org/10.1016/j.colsurfa.2016.07.066. URL http://www.sciencedirect.com/science/article/pii/S0927775716305878.

[14] I. Tucker, J. Penfold, R. K. Thomas, I. Grillo, J. G. Barker, and D. F. R. Mildner. Self assembly in mixed dialkyl chain cationic nonionic surfactant mixtures: Dihexadecyldimethyl ammonium bromide monododecyl hexaethylene glycol (monododecyl dodecaethylene glycol) mixtures. *Langmuir*, 24(15):7674–7687, 2008. doi: 10.1021/la703702p. URL https://doi.org/10.1021/la703702p. PMID: 18582000.

[15] E Feitosa, P.C.A Barreleiro, and G Olofsson. Phase transition in dioctadecyldimethylammonium bromide and chloride vesicles prepared by different methods. *Chemistry and Physics of Lipids*, 105(2):201 – 213, 2000. ISSN 0009-3084. doi: https://doi.org/10.1016/S0009-3084(00)00127-4. URL http://www.sciencedirect.com/science/article/pii/S0009308400001274.

[16] Linda S. Hirst, Adam Ossowski, Matthew Fraser, Jun Geng, Jonathan V. Selinger, and Robin L. B. Selinger. Morphology transition in lipid vesicles due to in-plane order and topological defects. *Proceedings of the National Academy of Sciences*, 110(9):3242–3247, 2013. ISSN 0027-8424. doi: 10.1073/pnas.1213994110. URL http://www.pnas.org/content/110/9/3242.

[17] Abhijeet Kumar, Jochen Kleinen, Joachim Venzmer, Anna Trybala, Victor Starov, and Tatiana Gambaryan-Roisman. Spreading and imbibition of vesicle dispersion droplets on porous substrates. *Colloids and Interfaces*, 3:53, 07 2019. doi: 10.3390/colloids3030053.

[18] Madivala G. Basavaraj, Naa Larteokor McFarlane, Matthew L. Lynch, and Norman J. Wagner. Nanovesicle formation and microstructure in aqueous ditallowethylesterdimethylammonium chloride (deedmac) solutions. *Journal of Colloid and Interface Science*, 429: 17 – 24, 2014. ISSN 0021-9797. doi: https://doi.org/10.1016/j.jcis.2014.04.064. URL http://www.sciencedirect.com/science/article/pii/S0021979714002835.

[19] Albert Einstein. Investigations on the theory of brownian motion. reprint of the 1st english edition (1926), 1956.

[20] R Befru Turan, Ayse Okur, Remziye Deveci, and Merve Acikel. Predicting the intra yarn porosity by image analysis method. *Textile Research Journal*, 82(16):1720–1728, 2012. doi: 10.1177/0040517511427971. URL https://doi.org/10.1177/0040517511427971.

[21] Helmut Wakeham and Nancy Spicer. Pore-size distribution in textiles-a study of windproof and water resistant cotton fabrics. *Textile Research Journal*, 19(11):703–710, 1949. doi: 10.1177/004051754901901105. URL https://doi.org/10.1177/004051754901901105.

[22] Abhijeet Kumar, Jochen Kleinen, Tatiana Gambaryan-Roisman, and Joachim Venzmer. Electrokinetic investigation of deposition of cationic fabric softener vesicles on anionic porous cotton fabrics. *Journal of Colloid and Interface Science*, 514:132 – 145, 2018. ISSN 0021-9797. doi: https://doi.org/10.1016/j.jcis.2017.11.062. URL http://www.sciencedirect.com/science/article/pii/S0021979717313681.

[23] Vincent Leung, Abdel Aziz M. Shehata, Carlos D.M. Filipe, and Robert Pelton. Streaming potential sensing in paper based microfluidic channels. *Colloids and Surfaces A: Physicochemical and Engineering Aspects*, 364(1):16 – 18, 2010. ISSN 0927-7757. doi: https://doi.org/10.1016/j.colsurfa.2010.04.008. URL http://www.sciencedirect.com/science/article/pii/S0927775710002372.

[24] Tijana Ristić, Silvo Hribernik, and Lidija Fras-Zemljič. Electrokinetic properties of fibres functionalised by chitosan and chitosan nanoparticles. *Cellulose*, 22(6):3811–3823, 2015. ISSN 1572-882X. doi: 10.1007/s10570-015-0760-6. URL http://dx.doi.org/10.1007/s10570-015-0760-6.

[25] Fei Wang and Martin A Hubbe. Development and evaluation of an automated streaming potential measurement device. *Colloids Surf., A*, 194(1):221 – 232, 2001. ISSN 0927-7757. doi: http://dx.doi.org/10.1016/S0927-7757(01)00802-0. URL http://www.sciencedirect.com/science/article/pii/S0927775701008020.

[26] Abhijeet Kumar, Laurent Gilson, Franziska Henrich, Verena Dahl, Jochen Kleinen, Tatiana Gambaryan-Roisman, and Joachim Venzmer. Intact deposition of cationic vesicles on anionic cellulose fibers: Role of vesicle size, polydispersity, and substrate roughness studied via streaming potential measurements. *Journal of Colloid and Interface Science*, 473:152 – 161, 2016. ISSN 0021-9797. doi: http://dx.doi.org/10.1016/j.jcis.2016.04.004. URL http://www.sciencedirect.com/science/article/pii/S0021979716302120.

[27] Lionel Ripoll, Claire Bordes, Pedro Marote, Sabrina Etheve, Abdelhamid Elaissari, and Hatem Fessi. Electrokinetic properties of bare or nanoparticle-functionalized textile fabrics.

Colloids Surf., A, 397:24 – 32, 2012. ISSN 0927-7757. doi: http://dx.doi.org/10.1016/j.colsurfa.2012.01.022. URL http://www.sciencedirect.com/science/article/pii/S0927775712000404.

[28] D. Stawski and C. Bellmann. Electrokinetic properties of polypropylene textile fabrics containing deposited layers of polyelectrolytes. *Colloids Surf., A*, 345(1):191 – 194, 2009. ISSN 0927-7757. doi: http://dx.doi.org/10.1016/j.colsurfa.2009.05.005. URL http://www.sciencedirect.com/science/article/pii/S0927775709002878.

[29] Thomas Luxbacher, Mirjana Čurlin, Irena Petrinić, Hermina Bukšek, and Tanja Pušić. Assessing the quality of raw cotton knitted fabrics by their streaming potential coefficients. *Cellulose*, 21(5):3829–3839, 2014. ISSN 1572-882X. doi: 10.1007/s10570-014-0388-y. URL http://dx.doi.org/10.1007/s10570-014-0388-y.

[30] Thomas Luxbacher. Euromembrane 2006 electrokinetic characterization of flat sheet membranes by streaming current measurement. *Desalination*, 199(1):376 – 377, 2006. ISSN 0011-9164. doi: http://dx.doi.org/10.1016/j.desal.2006.03.085. URL http://www.sciencedirect.com/science/article/pii/S0011916406006667.

[31] Markus Wegmann, Benjamin Michen, Thomas Luxbacher, Johannes Fritsch, and Thomas Graule. Modification of ceramic microfilters with colloidal zirconia to promote the adsorption of viruses from water. *Water Research*, 42(6):1726 – 1734, 2008. ISSN 0043-1354. doi: http://dx.doi.org/10.1016/j.watres.2007.10.030. URL http://www.sciencedirect.com/science/article/pii/S0043135407006689.

[32] Dennis C. Prieve and Paul J. Sides. Streaming potential near a rotating porous disk. *Langmuir*, 30(37):11197–11203, 2014. doi: 10.1021/la5022092. URL http://dx.doi.org/10.1021/la5022092.

[33] Younjin Min, Noshir Pesika, Joe Zasadzinski, and Jacob Israelachvili. Studies of bilayers and vesicle adsorption to solid substrates: Development of a miniature streaming potential apparatus (spa). *Langmuir*, 26(11):8684–8689, 2010. doi: 10.1021/la904842v. URL https://doi.org/10.1021/la904842v. PMID: 20180570.

[34] Sandrine Lavenus, Paul Pilet, Jerome Guicheux, Pierre Weiss, Guy Louarn, and Pierre Layrolle. Behaviour of mesenchymal stem cells, fibroblasts and osteoblasts on smooth surfaces. *Acta Biomater.*, 7(4):1525 – 1534, 2011. ISSN 1742-7061. doi: http://dx.doi.org/10.1016/j.actbio.2010.12.033. URL http://www.sciencedirect.com/science/article/pii/S1742706110005970.

[35] Yingjun Wang, Li Guo, Li Ren, Shiheng Yin, Jian Ge, Qianying Gao, Thomas Luxbacher, and Shijing Luo. A study on the performance of hyaluronic acid immobilized chitosan film. *Biomedical Materials*, 4(3):035009, 2009. URL http://stacks.iop.org/1748-605X/4/i=3/a=035009.

[36] Thomas Luxbacher. The zeta guide: Principles of the streaming potential technique. *Anton Paar GmbH*, 1(1):24 – 25, 2014. ISSN 978-3-200-03553-9.

[37] John A Ciriacks and Dale G Williams. A happel flow model streaming current relationship for determining the zeta potential of cylindrical fibers. *J. Colloid Interface Sci.*, 26(4):446 – 456, 1968. ISSN 0021-9797. doi: http://dx.doi.org/10.1016/0021-9797(68)90291-9. URL http://www.sciencedirect.com/science/article/pii/0021979768902919.

[38] A.V. Delgado, F. Gonzalez-Caballero, R.J. Hunter, L.K. Koopal, and J. Lyklema. Measurement and interpretation of electrokinetic phenomena. *Journal of Colloid and Interface Science*, 309(2):194 – 224, 2007. ISSN 0021-9797. doi: http://dx.doi.org/10.1016/j.jcis.2006.12.075. URL http://www.sciencedirect.com/science/article/pii/S002197970700015X. Elkin 06, International Electrokinetics Conference, June 25-29, Nancy, France.

[39] J. Lyklema. Electrokinetics after smoluchowski. *Colloids and Surfaces A: Physicochemical and Engineering Aspects*, 222(1):5 – 14, 2003. ISSN 0927-7757. doi: http://dx.doi.org/10.1016/S0927-7757(03)00217-6. URL http://www.sciencedirect.com/science/article/pii/S0927775703002176. A collection of papers presented at the International Symposium on Electrokinetic Phenomena, Cracow, Poland, August 18-22, 2003.

[40] C.C Christoforou, G.B Westermann-Clark, and J.L Anderson. The streaming potential and inadequacies of the helmholtz equation. *J. Colloid Interface Sci.*, 106(1):1 – 11, 1985. ISSN 0021-9797. doi: http://dx.doi.org/10.1016/0021-9797(85)90374-1. URL http://www.sciencedirect.com/science/article/pii/0021979785903741.

[41] C. L. Rice and R. Whitehead. Electrokinetic flow in a narrow cylindrical capillary. *J. Phys. Chem.*, 69(11):4017–4024, 1965. doi: 10.1021/j100895a062. URL http://dx.doi.org/10.1021/j100895a062.

[42] Z. Adamczyk, K. Sadlej, E. Wajnryb, M. Nattich, M.L. Ekiel Jezewska, and J. Blawzdziewicz. Streaming potential studies of colloid, polyelectrolyte and protein deposition. *Adv. Colloid Interface Sci.*, 153(1):1 – 29, 2010. ISSN 0001-8686. doi: http://dx.doi.org/10.1016/j.cis.2009.09.004. URL http://www.sciencedirect.com/science/article/pii/S000186860900089X.

[43] I.B Oldham, F.J Young, and J.F Osterle. Streaming potential in small capillaries. *J. Colloid Sci.*, 18(4):328 – 336, 1963. ISSN 0095-8522. doi: http://dx.doi.org/10.1016/0095-8522(63)90023-0. URL http://www.sciencedirect.com/science/article/pii/0095852263900230.

[44] G. A. H. Elton. Electroviscosity. i. the flow of liquids between surfaces in close proximity. *Proc. R. Soc. London, Ser. A*, 194(1037):259–274, 1948. ISSN 0080-4630. doi: 10.1098/rspa.1948.0079. URL http://rspa.royalsocietypublishing.org/content/194/1037/259.

[45] J. T. G. Overbeek. Electrokinetic phenomena. in colloid science. *Elsevier: Amsterdam*, 1: 194 – 244, 1952.

[46] Elizabeth Rodier and John Dodds. Streaming current measuring for determining the zeta potential of granular particles. *Part. Part. Syst. Charact.*, 12(4):198–203, 1995. ISSN 1521-4117. doi: 10.1002/ppsc.19950120407. URL http://dx.doi.org/10.1002/ppsc.19950120407.

[47] Philip R. Johnson. A comparison of streaming and microelectrophoresis methods for obtaining the zeta potential of granular porous media surfaces. *J. Colloid Interface Sci.*, 209 (1):264 – 267, 1999. ISSN 0021-9797. doi: http://dx.doi.org/10.1006/jcis.1998.5908. URL http://www.sciencedirect.com/science/article/pii/S0021979798959082.

[48] Hermina Buk. Zeta potential determination of polymeric materials using two differently designed measuring cells of an electrokinetic analyzer. *Acta Chim. Slov*, 57:700–706, 2010.

[49] Myung-Suk Chun, Sang-Yup Lee, and Seung-Man Yang. Estimation of zeta potential by electrokinetic analysis of ionic fluid flows through a divergent microchannel. *J. Colloid Interface Sci.*, 266(1):120 – 126, 2003. ISSN 0021-9797. doi: http://dx.doi.org/10.1016/S0021-9797(03)00576-9. URL http://www.sciencedirect.com/science/article/pii/S0021979703005769.

[50] John. A. Ciriacks. Doctor's dissertation-an investigation of the streaming current method for determining the zeta potential of fibers. *The Institute of Paper Chemistry*, 1(1):24 – 25, 1967. ISSN 978-3-200-03553-9.

[51] H. J. Jacobasch, G. Baubock, and J. Schurz. Problems and results of zeta-potential measurements on fibers. *Colloid Polym. Sci.*, 263(1):3 – 24, 1985. ISSN 1435-1536. doi: 10.1007/BF01411243. URL http://dx.doi.org/10.1007/BF01411243.

[52] A. Szymczyk, P. Fievet, and A. Foissy. Electrokinetic characterization of porous plugs from streaming potential coupled with electrical resistance measurements. *J. Colloid Interface Sci.*, 255(2):323 – 331, 2002. ISSN 0021-9797. doi: http://dx.doi.org/10.1006/jcis.2002.8591. URL http://www.sciencedirect.com/science/article/pii/S0021979702985917.

[53] SG Mason and DAI Goring. Electrokinetic properties of cellulose fibers: I. stream potential and electroosmosis. *Can. J. Res.*, 28(6):307–322, 1950.

[54] G. J. Biefer and S.G. Mason. Electrokinetic streaming, viscous flow and electrical conduction in interfibre networks. the pore orientation factor. *Trans. Faraday Soc.*, 55:1239–1245, 1959.

[55] MY Chang and AA Robertson. Zeta potential measurements of fibres. d-c. streaming current method. *Can. J. Chem. Eng.*, 45(2):66–71, 1967.

[56] E Hasselbrink Jr, M Hunter, W Even Jr, and J Irvin. Sandia report- microscale zeta potential evaluations using streaming current measurements. *Sandia National Laboratories*, pages 15 – 23, 2001.

[57] Paul W. J. Glover, Emilie Walker, and Matthew D. Jackson. Streaming-potential coefficient of reservoir rock: A theoretical model. *Geophysics*, 77(2):D17–D43, 2012. doi: 10.1190/geo2011-0364.1. URL http://dx.doi.org/10.1190/geo2011-0364.1.

[58] Andriy Yaroshchuk and Thomas Luxbacher. Interpretation of electrokinetic measurements with porous films: Role of electric conductance and streaming current within porous structure. *Langmuir*, 26(13):10882–10889, 2010. doi: 10.1021/la100777z. URL http://dx.doi.org/10.1021/la100777z.

[59] Anthony Szymczyk, Yonis Ibrahim Dirir, Matthieu Picot, Irene Nicolas, and Frederic Barriere. Advanced electrokinetic characterization of composite porous membranes. *J. Membr. Sci.*, 429:44 – 51, 2013. ISSN 0376-7388. doi: http://dx.doi.org/10.1016/j.memsci.2012.11.076. URL http://www.sciencedirect.com/science/article/pii/S0376738812009040.

[60] Sebastien Deon, Patrick Fievet, and Choukri Osman Doubad. Tangential streaming potential/current measurements for the characterization of composite membranes. *Journal of Membrane Science*, 423-424:413 – 421, 2012. ISSN 0376-7388. doi: http://dx.doi.org/10.1016/j.memsci.2012.08.038. URL http://www.sciencedirect.com/science/article/pii/S0376738812006370.

[61] A. Tamayol, A. Khosla, B.L. Gray, and M. Bahrami. Creeping flow through ordered arrays of micro-cylinders embedded in a rectangular minichannel. *Int. J. Heat Mass Transfer*, 55(15):3900 – 3908, 2012. ISSN 0017-9310. doi: http://dx.doi.org/10.1016/j.ijheatmasstransfer.2012.03.008. URL http://www.sciencedirect.com/science/article/pii/S0017931012001573.

[62] W. H. Zhong, I. G. Currie, and D. F. James. Creeping flow through a model fibrous porous medium. *Exp. Fluids*, 40(1):119–126, 2006. ISSN 1432-1114. doi: 10.1007/s00348-005-0053-1. URL http://dx.doi.org/10.1007/s00348-005-0053-1.

[63] Z. Liang, M.A. Ioannidis, and I. Chatzis. Permeability and electrical conductivity of porous media from 3d stochastic replicas of the microstructure. *Chem. Eng. Sci.*, 55(22):5247 – 5262, 2000. ISSN 0009-2509. doi: http://dx.doi.org/10.1016/S0009-2509(00)00142-1. URL http://www.sciencedirect.com/science/article/pii/S0009250900001421.

[64] S Levine, J.R Marriott, G Neale, and N Epstein. Theory of electrokinetic flow in fine cylindrical capillaries at high zeta-potentials. *J. Colloid Interface Sci.*, 52(1):136 – 149, 1975. ISSN 0021-9797. doi: http://dx.doi.org/10.1016/0021-9797(75)90310-0. URL http://www.sciencedirect.com/science/article/pii/0021979775903100.

[65] Ingmar H. Huisman, Gun Tragardh, and Christian Tragardhand Arto Pihlajamaki. Determining the zeta-potential of ceramic microfiltration membranes using the electroviscous effect. *J. Membr. Sci.*, 147(2):187 – 194, 1998. ISSN 0376-7388. doi: http://dx.doi.org/10.1016/S0376-7388(98)00135-5. URL http://www.sciencedirect.com/science/article/pii/S0376738898001355.

[66] J Lyklema and M Minor. On surface conduction and its role in electrokinetics. *Colloids Surf., A*, 140(1):33 – 41, 1998. ISSN 0927-7757. doi: http://dx.doi.org/10.1016/S0927-7757(97)00266-5. URL http://www.sciencedirect.com/science/article/pii/S0927775797002665.

[67] David Erickson, Dongqing Li, and Carsten Werner. An improved method of determining the ζ-potential and surface conductance. *J. Colloid Interface Sci.*, 232(1):186 – 197, 2000. ISSN 0021-9797. doi: http://dx.doi.org/10.1006/jcis.2000.7153. URL http://www.sciencedirect.com/science/article/pii/S0021979700971534.

[68] Carsten Werner, Ralf Zimmermann, and Thomas Kratzmuller. Streaming potential and streaming current measurements at planar solid liquid interfaces for simultaneous determination of zeta potential and surface conductivity. *Colloids Surf., A*, 192(1):205 – 213, 2001. ISSN 0927-7757. doi: http://dx.doi.org/10.1016/S0927-7757(01)00725-7. URL http://www.sciencedirect.com/science/article/pii/S0927775701007257.

[69] Jacob H Masliyah and Subir Bhattacharjee. *Electrokinetic and colloid transport phenomena*. John Wiley & Sons, 2006.

[70] A. Tamayol and M. Bahrami. Analytical determination of viscous permeability of fibrous porous media. *Int. J. Heat Mass Transfer*, 52(9):2407 – 2414, 2009. ISSN 0017-9310. doi: http://dx.doi.org/10.1016/j.ijheatmasstransfer.2008.09.032. URL http://www.sciencedirect.com/science/article/pii/S0017931008005954.

[71] JJL Higdon and GD Ford. Permeability of three-dimensional models of fibrous porous media. *J. Fluid Mech.*, 308:341–361, 1996.

[72] Karol Pietrak and Tomasz S Wisniewski. A review of models for effective thermal conductivity of composite materials. *J. Power Technol.*, 95(1):14, 2015.

[73] J. Becker; A. Wiegmann; V. Schulz. Design of fibrous filter media based on the simulation of pore size measures. *Fraunhofer-Institut fuer Techno- und Wirtschaftsmathematik ITWM*, 45:71–78, 2007.

[74] J. Venzmer. Hairs, cars, textile: In quats we care. *SOFW J*, 136(3):62–71, 2010. cited By 3.

[75] Vladimir P. Zhdanov, Kristian Dimitrievski, and Bengt Kasemo. Adsorption and spontaneous rupture of vesicles composed of two types of lipids. *Langmuir*, 22(8):3477–3480, 2006. doi: 10.1021/la053163f. URL https://doi.org/10.1021/la053163f. PMID: 16584214.

[76] Ilya Reviakine and Alain Brisson. Formation of supported phospholipid bilayers from unilamellar vesicles investigated by atomic force microscopy. *Langmuir*, 16(4):1806–1815, 2000. doi: 10.1021/la9903043. URL https://doi.org/10.1021/la9903043.

[77] Ralf P. Richter, R Berat, and Alain R. Brisson. Formation of solid-supported lipid bilayers: An integrated view. *Langmuir*, 22(8):3497–3505, 2006. doi: 10.1021/la052687c. URL https://doi.org/10.1021/la052687c. PMID: 16584220.

[78] Ralf Richter, Anneke Mukhopadhyay, and Alain Brisson. Pathways of lipid vesicle deposition on solid surfaces: A combined qcm d and afm study. *Biophysical Journal*, 85(5):3035 – 3047, 2003. ISSN 0006-3495. doi: https://doi.org/10.1016/S0006-3495(03)74722-5. URL http://www.sciencedirect.com/science/article/pii/S0006349503747225.

[79] C. A. Keller, K. Glasmästar, V. P. Zhdanov, and B. Kasemo. Formation of supported membranes from vesicles. *Phys. Rev. Lett.*, 84:5443–5446, Jun 2000. doi: 10.1103/PhysRevLett.84.5443. URL https://link.aps.org/doi/10.1103/PhysRevLett.84.5443.

[80] Seyda Bucak, Chen Wang, Paul E. Laibinis, and T. Alan Hatton. Dynamics of supported lipid bilayer deposition from vesicle suspensions. *Journal of Colloid and Interface Science*, 348(2):608 – 614, 2010. ISSN 0021-9797. doi: https://doi.org/10.1016/j.jcis.2010.04.087. URL http://www.sciencedirect.com/science/article/pii/S0021979710005059.

[81] Holger Schoenherr, Joseph M. Johnson, Peter Lenz, Curtis W. Frank, and Steven G. Boxer. Vesicle adsorption and lipid bilayer formation on glass studied by atomic force microscopy. *Langmuir*, 20(26):11600–11606, 2004. doi: 10.1021/la049302v. URL https://doi.org/10.1021/la049302v. PMID: 15595789.

[82] Erik Reimhult, Fredrik Höök, and Bengt Kasemo. Intact vesicle adsorption and supported biomembrane formation from vesicles in solution: Influence of surface chemistry, vesicle size, temperature, and osmotic pressure. *Langmuir*, 19(5):1681–1691, 2003. doi: 10.1021/la0263920. URL https://doi.org/10.1021/la0263920.

[83] A. P. Serro, A. Carapeto, G. Paiva, J. P. S. Farinha, R. Colaco, and B. Saramago. Formation of an intact liposome layer adsorbed on oxidized gold confirmed by three complementary techniques: Qcmd, afm and confocal fluorescence microscopy. *Surface and Interface Analysis*, 44(4):426–433, 2011. doi: 10.1002/sia.3820. URL https://onlinelibrary.wiley.com/doi/abs/10.1002/sia.3820.

[84] C.A. Keller and B. Kasemo. Surface specific kinetics of lipid vesicle adsorption measured with a quartz crystal microbalance. *Biophysical Journal*, 75(3):1397 – 1402, 1998. ISSN 0006-3495. doi: https://doi.org/10.1016/S0006-3495(98)74057-3. URL http://www.sciencedirect.com/science/article/pii/S0006349598740573.

[85] Nikhil D. Kalyankar, Manoj K. Sharma, Shyam V. Vaidya, David Calhoun, Charles Maldarelli, Alexander Couzis, and Lane Gilchrist. Arraying of intact liposomes into chemically functionalized microwells. *Langmuir*, 22(12):5403–5411, 2006. doi: 10.1021/la0602719. URL https://doi.org/10.1021/la0602719. PMID: 16732670.

[86] Vladimir P. Zhdanov. Mechanism of rupture of single adsorbed vesicles. *Chemical Physics Letters*, 641:20 – 22, 2015. ISSN 0009-2614. doi: https://doi.org/10.1016/j.cplett.2015.10.053. URL http://www.sciencedirect.com/science/article/pii/S000926141500809X.

[87] Hsing Lun Wu, Po Yu Chen, Chia Ling Chi, Heng Kwong Tsao, and Yu Jane Sheng. Vesicle deposition on hydrophilic solid surfaces. *Soft Matter*, 9:1908–1919, 2013. doi:

10.1039/C2SM27450G. URL http://dx.doi.org/10.1039/C2SM27450G.

[88] Joshua A. Jackman, Jae Hyeok Choi, Vladimir P. Zhdanov, and Nam Joon Cho. Influence of osmotic pressure on adhesion of lipid vesicles to solid supports. *Langmuir*, 29(36):11375–11384, 2013. doi: 10.1021/la4017992. URL https://doi.org/10.1021/la4017992. PMID: 23901837.

[89] E. Reimhult, M. Zäch, F. Höök, and B. Kasemo. A multitechnique study of liposome adsorption on au and lipid bilayer formation on sio2. *Langmuir*, 22(7):3313–3319, 2006. doi: 10.1021/la0519554. URL https://doi.org/10.1021/la0519554. PMID: 16548594.

[90] Ph Lavalle, B Senger, P Schaaf, J-C Voegel, and I-F Stoltz. Adhesion of red blood cells to solid surfaces: experimental results and modeling. *Clinical Hemorheology and Microcirculation*, 16(1):35–42, 1996.

[91] Zbigniew Adamczyk, Malgorzata Nattich Rak, Marta Sadowska, Aneta Michna, and Katarzyna Szczepaniak. Mechanisms of nanoparticle and bioparticle deposition kinetic aspects. *Colloids and Surfaces A: Physicochemical and Engineering Aspects*, 439:3 – 22, 2013. ISSN 0927-7757. doi: http://doi.org/10.1016/j.colsurfa.2012.12.060. URL http://www.sciencedirect.com/science/article/pii/S0927775713000101. Nanoparticles@interfaces.

[92] M Semmler, EK Mann, J Ricka, and M Borkovec. Diffusional deposition of charged latex particles on water- solid interfaces at low ionic strength. *Langmuir*, 14(18):5127–5132, 1998.

[93] I Michaeli, D.R Absolom, and C.J Van Oss. Diffusion of adsorbed protein within the plane of adsorption. *Journal of Colloid and Interface Science*, 77(2):586 – 587, 1980. ISSN 0021-9797. doi: https://doi.org/10.1016/0021-9797(80)90337-9. URL http://www.sciencedirect.com/science/article/pii/0021979780903379.

[94] A.P. Minton. Lateral diffusion of membrane proteins in protein-rich membranes. a simple hard particle model for concentration dependence of the two-dimensional diffusion coefficient. *Biophysical Journal*, 55(4):805 – 808, 1989. ISSN 0006-3495. doi: https://doi.org/10.1016/S0006-3495(89)82880-2. URL http://www.sciencedirect.com/science/article/pii/S0006349589828802.

[95] George Vane. Scott. Spectrophotometric determination of cationic surfactants with orange ii. *Analytical Chemistry*, 40(4):768–773, 1968. doi: 10.1021/ac60260a038. URL https://doi.org/10.1021/ac60260a038.

[96] Z. Adamczyk, M. Zembala, and A. Michna. Polyelectrolyte adsorption layers studied by streaming potential and particle deposition. *Journal of Colloid and Interface Science*, 303 (2):353 – 364, 2006. ISSN 0021-9797. doi: https://doi.org/10.1016/j.jcis.2006.07.083. URL http://www.sciencedirect.com/science/article/pii/S0021979706006874.

[97] Krzysztof Sadlej, Eligiusz Wajnryb, Jerzy Blawzdziewicz, Maria L. Ekiel-Jezewska, and Zbigniew Adamczyk. Streaming current and streaming potential for particle covered

surfaces: Virial expansion and simulations. *The Journal of Chemical Physics*, 130(14): 144706, 2009. doi: 10.1063/1.3103545. URL https://doi.org/10.1063/1.3103545.

[98] Maria Zembala and Zbigniew Adamczyk. Measurements of streaming potential for mica covered by colloid particles. *Langmuir*, 16(4):1593–1601, 2000. doi: 10.1021/la9905970. URL http://dx.doi.org/10.1021/la9905970.

[99] Maria Zembala. Electrokinetics of heterogeneous interfaces. *Advances in Colloid and Interface Science*, 112(1):59 – 92, 2004. ISSN 0001-8686. doi: https://doi.org/10.1016/j.cis.2004.08.001. URL http://www.sciencedirect.com/science/article/pii/S0001868604000648.

[100] Hsing Lun Wu, Po-Yu Chen, Chia-Ling Chi, Heng Kwong Tsao, and Yu Jane Sheng. Vesicle deposition on hydrophilic solid surfaces. *Soft Matter*, 9:1908–1919, 2013. doi: 10.1039/C2SM27450G. URL http://dx.doi.org/10.1039/C2SM27450G.

[101] Sergio P. Moura and Ana M. Carmona Ribeiro. Adsorption behavior of dodab/dppc vesicles on silica. *Journal of Colloid and Interface Science*, 313(2):519 – 526, 2007. ISSN 0021-9797. doi: https://doi.org/10.1016/j.jcis.2007.04.061. URL http://www.sciencedirect.com/science/article/pii/S0021979707005218.

[102] Kunal V Savaji, Olivia Niitsoo, and Alexander Couzis. Influence of particle/solid surface zeta potential on particle adsorption kinetics. *Journal of colloid and interface science*, 431: 165–175, 2014.

[103] Micha Semmler, Jaroslav Rička, and Michal Borkovec. Diffusional deposition of colloidal particles: electrostatic interaction and size polydispersity effects. *Colloids and Surfaces A: Physicochemical and Engineering Aspects*, 165(1-3):79–93, 2000.

[104] Z. Adamczyk, B. Siwek, P. Weronski, and M. Zembala. Adsorption of colloid particle mixtures at interfaces. In Heinz Rehage and Gerhard Peschel, editors, *Structure, Dynamics and Properties of Disperse Colloidal Systems*, pages 41–47, Darmstadt, 1998. Steinkopff. ISBN 978-3-7985-1652-6.

[105] Michael Rabe, Dorinel Verdes, and Stefan Seeger. Understanding protein adsorption phenomena at solid surfaces. *Advances in Colloid and Interface Science*, 162(1):87 – 106, 2011. ISSN 0001-8686. doi: https://doi.org/10.1016/j.cis.2010.12.007. URL http://www.sciencedirect.com/science/article/pii/S0001868611000066.

[106] Joachim Venzmer. Alltägliche phänomene. grenzflächenchemische spezialitäten. *Chemie in unserer Zeit*, 42(2):72–79, 2008. ISSN 1521-3781. doi: 10.1002/ciuz.200800447. URL http://dx.doi.org/10.1002/ciuz.200800447.

[107] J Venzmer. Hairs, cars, textiles : In quats we care. *SOFW-Journal*, 136:62–71, 2010.

[108] Roya Dastjerdi and Majid Montazer. A review on the application of inorganic nano-structured materials in the modification of textiles: Focus on anti-microbial properties. *Colloids and Surfaces B: Biointerfaces*, 79(1):5 – 18, 2010. ISSN 0927-7765. doi: http://dx.doi.org/10.1016/j.colsurfb.2010.03.029. URL http://www.sciencedirect.com/

science/article/pii/S0927776510001773.

[109] Ning Wu, Martin A Hubbe, Orlando J Rojas, and Sunkyu Park. Permeation of polyelectrolytes and other solutes into the pore spaces of water-swollen cellulose: A review. *BioResources*, 4(3):1222–1262, 2009.

[110] W. M. Deen. Hindered transport of large molecules in liquid-filled pores. *AIChE Journal*, 33(9):1409–1425, 1987. ISSN 1547-5905. doi: 10.1002/aic.690330902. URL http://dx.doi.org/10.1002/aic.690330902.

[111] Panadda Dechadilok and William M. Deen. Hindrance factors for diffusion and convection in pores. *Industrial & Engineering Chemistry Research*, 45(21):6953–6959, 2006. doi: 10.1021/ie051387n. URL http://dx.doi.org/10.1021/ie051387n.

[112] Triantafyllos Stylianopoulos, Ming-Zher Poh, Numpon Insin, Moungi G. Bawendi, Dai Fukumura, LanceÂ L. Munn, and Rakesh K. Jain. Diffusion of particles in the extracellular matrix: The effect of repulsive electrostatic interactions. *Biophysical Journal*, 99(5):1342 – 1349, 2010. ISSN 0006-3495. doi: http://dx.doi.org/10.1016/j.bpj.2010.06.016. URL http://www.sciencedirect.com/science/article/pii/S0006349510007277.

[113] Oliver Lieleg, Regina M. Baumgaertel, and Andreas R. Bausch. Selective filtering of particles by the extracellular matrix: An electrostatic bandpass. *Biophysical Journal*, 97(6): 1569 – 1577, 2009. ISSN 0006-3495. doi: http://dx.doi.org/10.1016/j.bpj.2009.07.009. URL http://www.sciencedirect.com/science/article/pii/S0006349509012284.

[114] Michael J. Skaug and Daniel K. Schwartz. Tracking nanoparticle diffusion in porous filtration media. *Industrial & Engineering Chemistry Research*, 54(16):4414–4419, 2015. doi: 10.1021/ie503895b. URL http://dx.doi.org/10.1021/ie503895b.

[115] Francesco S. Gentile, Ilaria De Santo, Gaetano D Avino, Lucio Rossi, Giovanni Romeo, Francesco Greco, Paolo A. Netti, and Pier Luca Maffettone. Hindered brownian diffusion in a square-shaped geometry. *Journal of Colloid and Interface Science*, 447:25 – 32, 2015. ISSN 0021-9797. doi: http://dx.doi.org/10.1016/j.jcis.2015.01.055. URL http://www.sciencedirect.com/science/article/pii/S0021979715001010.

[116] David J. Hughes, Zhanfeng Cui, Robert W. Field, and Uday K. Tirlapur. In situ three-dimensional characterization of membrane fouling by protein suspensions using multiphoton microscopy. *Langmuir*, 22(14):6266–6272, 2006. doi: 10.1021/la053388q. URL http://dx.doi.org/10.1021/la053388q. PMID: 16800685.

[117] Martin A. Hubbe, Ning Wu, Orlando J. Rojas, and Sunkyu Park. Permeation of a cationic polyelectrolyte into mesoporous silica. part 2. effects of time and pore size on streaming potential. *Colloids and Surfaces A: Physicochemical and Engineering Aspects*, 364(1):7 – 15, 2010. ISSN 0927-7757. doi: http://dx.doi.org/10.1016/j.colsurfa.2010.05.005. URL http://www.sciencedirect.com/science/article/pii/S092777571000302X.

[118] Martin A. Hubbe, Ning Wu, Orlando J. Rojas, and Sunkyu Park. Permeation of a cationic polyelectrolyte into mesoporous silica: Part 3. using adsorption isotherms to elucidate streaming potential results. *Colloids and Surfaces A: Physicochemical and Engineering*

Aspects, 381(1):1 – 6, 2011. ISSN 0927-7757. doi: http://dx.doi.org/10.1016/j.colsurfa.2010.12.052. URL http://www.sciencedirect.com/science/article/pii/S0927775711000562.

[119] Zbigniew Adamczyk. *Particles at interfaces: interactions, deposition, structure*, volume 9. Academic Press, 2006.

[120] Nina Kuentzer, Pavel Simacek, Suresh G. Advani, and Shawn Walsh. Permeability characterization of dual scale fibrous porous media. *Composites Part A: Applied Science and Manufacturing*, 37(11):2057 – 2068, 2006. ISSN 1359-835X. doi: http://dx.doi.org/10.1016/j.compositesa.2005.12.005. URL http://www.sciencedirect.com/science/article/pii/S1359835X05004306.

[121] Zbigniew Adamczyk, Lilianna Szyk-Warszynska, Maria Zembala, and Marian Lehocky. In situ studies of particle deposition on non-transparent substrates. *Colloids and Surfaces A: Physicochemical and Engineering Aspects*, 235(1):65 – 72, 2004. ISSN 0927-7757. doi: http://dx.doi.org/10.1016/j.colsurfa.2003.12.021. URL http://www.sciencedirect.com/science/article/pii/S0927775704000354.

[122] Monika Wasilewska and Zbigniew Adamczyk. Fibrinogen adsorption on mica studied by afm and in situ streaming potential measurements. *Langmuir*, 27(2):686–696, 2011. doi: 10.1021/la102931a. URL http://dx.doi.org/10.1021/la102931a. PMID: 21155546.

[123] Abhijeet Kumar, Verena Dahl, Jochen Kleinen, Tatiana Gambaryan-Roisman, and Joachim Venzmer. Influence of lipid bilayer phase behavior and substrate roughness on the pathways of intact vesicle deposition: A streaming potential study. *Colloids and Surfaces A: Physicochemical and Engineering Aspects*, 521:302 – 311, 2017. ISSN 0927-7757. doi: http://doi.org/10.1016/j.colsurfa.2016.07.066. URL http://www.sciencedirect.com/science/article/pii/S0927775716305878.

[124] Jochen Kleinen, Andreas Klee, and Walter Richtering. Influence of architecture on the interaction of negatively charged multisensitive poly(n-isopropylacrylamide)-co-methacrylic acid microgels with oppositely charged polyelectrolyte: Absorption vs adsorption. *Langmuir*, 26(13):11258–11265, 2010. doi: 10.1021/la100579b. URL http://dx.doi.org/10.1021/la100579b. PMID: 20377221.

[125] H Löwen, A Hörtel, A Barreira-Fontecha, H J Schöpe, E Allahyarov, and T Palberg. Charged colloidal particles in a charged wedge: do they go in or out? *Journal of Physics: Condensed Matter*, 20(40):404221, 2008. URL http://stacks.iop.org/0953-8984/20/i=40/a=404221.

[126] Micha Semmler, Jaroslav Ricka, and Michal Borkovec. Diffusional deposition of colloidal particles: electrostatic interaction and size polydispersity effects. *Colloids and Surfaces A: Physicochemical and Engineering Aspects*, 165(1):79 – 93, 2000. ISSN 0927-7757. doi: http://dx.doi.org/10.1016/S0927-7757(99)00438-0. URL http://www.sciencedirect.com/science/article/pii/S0927775799004380.

[127] Zbigniew Adamczyk. Particle adsorption and deposition: role of electrostatic interactions. *Advances in Colloid and Interface Science*, 100-102:267 – 347, 2003. ISSN 0001-8686. doi: http://dx.doi.org/10.1016/S0001-8686(02)00062-3. URL http://www.sciencedirect.com/science/article/pii/S0001868602000623.

[128] Kunal V. Savaji, Olivia Niitsoo, and Alexander Couzis. Influence of particle/solid surface zeta potential on particle adsorption kinetics. *Journal of Colloid and Interface Science*, 431: 165 – 175, 2014. ISSN 0021-9797. doi: http://dx.doi.org/10.1016/j.jcis.2014.05.030. URL http://www.sciencedirect.com/science/article/pii/S0021979714003361.

[129] Richard C. Daniel and John C. Berg. Spreading on and penetration into thin, permeable print media: Application to ink-jet printing. *Advances in Colloid and Interface Science*, 123-126:439 – 469, 2006. ISSN 0001-8686. doi: https://doi.org/10.1016/j.cis.2006.05.012. URL http://www.sciencedirect.com/science/article/pii/S0001868606000637. Special Issue in Honor of Dr. K. L. Mittal.

[130] Wenkui Li and Francis LS Tse. Dried blood spot sampling in combination with lc-ms/ms for quantitative analysis of small molecules. *Biomedical Chromatography*, 24(1):49–65, 2010.

[131] Neil Spooner, Rakesh Lad, and Matt Barfield. Dried blood spots as a sample collection technique for the determination of pharmacokinetics in clinical studies: considerations for the validation of a quantitative bioanalytical method. *Analytical chemistry*, 81(4): 1557–1563, 2009.

[132] Rolf Puchta. Cationic surfactants in laundry detergents and laundry aftertreatment aids. *Journal of the American Oil Chemists' Society*, 61(2):367–376, 1984. ISSN 1558-9331. doi: 10.1007/BF02678796. URL http://dx.doi.org/10.1007/BF02678796.

[133] Sarah A Ibrahim. Spray-on transdermal drug delivery systems. *Expert Opinion on Drug Delivery*, 12(2):195–205, 2015. doi: 10.1517/17425247.2015.961419. URL https://doi.org/10.1517/17425247.2015.961419. PMID: 25227233.

[134] Atul Nayak, Diganta B Das, Tzu C Chao, and Victor M Starov. Spreading of a lidocaine formulation on microneedle-treated skin. *Journal of pharmaceutical sciences*, 104(12): 4109–4116, 2015.

[135] K.S. Lee, C.Y. Cheah, R.J. Copleston, V.M. Starov, and K. Sefiane. Spreading and evaporation of sessile droplets: Universal behaviour in the case of complete wetting. *Colloids and Surfaces A: Physicochemical and Engineering Aspects*, 323(1):63 – 72, 2008. ISSN 0927-7757. doi: https://doi.org/10.1016/j.colsurfa.2007.09.033. URL http://www.sciencedirect.com/science/article/pii/S0927775707008813. Bubble and Drop Interfaces.

[136] Tzu Chieh Chao, Omid Arjmandi-Tash, Diganta B. Das, and Victor M. Starov. Simultaneous spreading and imbibition of blood droplets over porous substrates in the case of partial wetting. *Colloids and Surfaces A: Physicochemical and Engineering Aspects*, 505:9 – 17, 2016. ISSN 0927-7757. doi: https://doi.org/10.1016/j.colsurfa.2015.10.056. URL

http://www.sciencedirect.com/science/article/pii/S0927775715303150. 6th International Workshop on Bubble and Drop Interfaces.

[137] Sheng Wang, Dong Zeng, Jiao Niu, Hanjie Wang, Liangliang Wang, Qin Li, Changyi Li, Hao Song, Jin Chang, and Lianyun Zhang. Development of an efficient transdermal drug delivery system with tat-conjugated cationic polymeric lipid vesicles. *Journal of Materials Chemistry B*, 2(7):877–884, 2014.

[138] Alka Lohani and Anurag Verma. Vesicles: Potential nano carriers for the delivery of skin cosmetics. *Journal of Cosmetic and Laser Therapy*, 19(8):485–493, 2017. doi: 10.1080/14764172.2017.1358451. URL https://doi.org/10.1080/14764172.2017.1358451. PMID: 28753057.

[139] V.M. Starov, V.V. Kalinin, and Jing-Den Chen. Spreading of liquid drops over dry surfaces. *Advances in Colloid and Interface Science*, 50:187 – 221, 1994. ISSN 0001-8686. doi: https://doi.org/10.1016/0001-8686(94)80030-8. URL http://www.sciencedirect.com/science/article/pii/0001868694800308.

[140] GARY F. TELETZKE, H. TED DAVIS, and L.E. SCRIVEN. How liquids spread on solids. *Chemical Engineering Communications*, 55(1-6):41–82, 1987. doi: 10.1080/00986448708911919. URL https://doi.org/10.1080/00986448708911919.

[141] V.M. Starov, S.R. Kosvintsev, V.D. Sobolev, M.G. Velarde, and S.A. Zhdanov. Spreading of liquid drops over saturated porous layers. *Journal of Colloid and Interface Science*, 246(2): 372 – 379, 2002. ISSN 0021-9797. doi: https://doi.org/10.1006/jcis.2001.8077. URL http://www.sciencedirect.com/science/article/pii/S0021979701980774.

[142] Omid Arjmandi-Tash, Nina M. Kovalchuk, Anna Trybala, Igor V. Kuchin, and Victor Starov. Kinetics of wetting and spreading of droplets over various substrates. *Langmuir*, 33 (18):4367–4385, 2017. doi: 10.1021/acs.langmuir.6b04094. URL https://doi.org/10.1021/acs.langmuir.6b04094. PMID: 28190350.

[143] Jarl B. Rosenholm. Liquid spreading on solid surfaces and penetration into porous matrices: Coated and uncoated papers. *Advances in Colloid and Interface Science*, 220: 8 – 53, 2015. ISSN 0001-8686. doi: https://doi.org/10.1016/j.cis.2015.01.009. URL http://www.sciencedirect.com/science/article/pii/S0001868615000330.

[144] Tatiana Gambaryan-Roisman. Liquids on porous layers: wetting, imbibition and transport processes. *Current Opinion in Colloid & Interface Science*, 19(4):320 – 335, 2014. ISSN 1359-0294. doi: http://dx.doi.org/10.1016/j.cocis.2014.09.001. URL http://www.sciencedirect.com/science/article/pii/S1359029414000880.

[145] Tzu Chieh Chao, Anna Trybala, Victor Starov, and Diganta B. Das. Influence of haematocrit level on the kinetics of blood spreading on thin porous medium during dried blood spot sampling. *Colloids and Surfaces A: Physicochemical and Engineering Aspects*, 451:38 – 47, 2014. ISSN 0927-7757. doi: https://doi.org/10.1016/j.colsurfa.2014.03.033. URL http://www.sciencedirect.com/science/article/pii/S0927775714002556.

[146] Robert D Deegan, Olgica Bakajin, Todd F Dupont, Greb Huber, Sidney R Nagel, and Thomas A Witten. Capillary flow as the cause of ring stains from dried liquid drops. *Nature*, 389(6653):827, 1997.

[147] Faiza Hidri, Nour Sghaier, Houda Eloukabi, Marc Prat, and S Ben Nasrallah. Porous medium coffee ring effect and other factors affecting the first crystallisation time of sodium chloride at the surface of a drying porous medium. *Physics of Fluids*, 25(12): 127101, 2013.

[148] Hua Hu and Ronald G. Larson. Evaporation of a sessile droplet on a substrate. *The Journal of Physical Chemistry B*, 106(6):1334–1344, 2002. doi: 10.1021/jp0118322. URL `https://doi.org/10.1021/jp0118322`.

A Appendix

The expressions for the functions $f_s(S/R)$ and $g_s(z/R, S/R)$ in Chapter 4 are given below :

$$f_s(S/R) = 2\int_0^1 \frac{1}{\left(\frac{S}{2R} - \sqrt{1-x^2}\right)^3} dx + 8\left(\frac{R}{S}\right)^2 - 16\left(\frac{R}{S}\right)^3 \tag{A.1}$$

$$g_s(z/R, S/R) = \int_0^{z/R} \frac{\sqrt{1-x^2}}{\left(\frac{S}{2R} - \sqrt{1-x^2}\right)^3} dx \tag{A.2}$$

List of Symbols and Abbreviations

Symbols

Symbol	Description	Unit
ΔP	Pressure difference	bar
I_{str}	Streaming current	A
U_{str}	Streaming potential	V
A_c	cross-sectional area	m^2
ρ_e	Electric charge density	C/m^3
ζ	Zeta potential	V
κ	Electrical conductivity	S/m
ϵ_o	vacuum permittivity	F/m
ϵ_{rs}	dielectric constant of the electrolyte	
μ	dynamic viscosity	kgm/s
ϕ	Porosity	
R	Electric resistance	Ohm
τ_{wall}	Wall shear stress	N/m^2
δ_{EDL}	Electric double layer thickness	m
U_{scf}	Shape correction factor	
Q	Volumetric flow rate	m^3/s
ζ_{app}	Apparent zeta potential	V
θ	Surface coverage	
$p_{pr,i}$	Probability of colloidal permeation across i^{th} pore	
$p_{dp,i}$	Probability of colloidal deposition in i^{th} pore	
$R_{dp,i}$	Rate of colloidal deposition in i^{th} pore	s^{-1}
$R_{pr,i}$	Rate of colloidal permeation in i^{th} pore	s^{-1}
ϕ_{int}	internal porosity	
ϕ_{ext}	external porosity	
L	Liquid cap base diameter	m
l	Wetted area diameter	m
$\theta_c(t)$	Contact Angle	degree
θ_r	Receding contact angle	degree
θ_a	Advancing contact angle	degree
D	Diffusivity	m^2/s
I	Pixel intensity	
J	Evaporation mass flux	kgm^2/s

Abbreviations

Abbreviation	Meaning
HS	Helmholtz-Smoluchowski
EM	Electron microscopy
EDL	Electric double layer
SCF	Shape correction factor

List of Figures

1.1. (A),(B) and (C) : Common fabric softener, hair conditioner and skin care products, (D) Dosing of a fabric softener formulation into a washing machine, (E) and (F) Representation of the everyday use of hair conditioner and skin care lotions 2
1.2. Porous structures of textile (A), paper (B), hair (C) and the human skin epidermis (D) as observed via different microscopy techniques. Fig. 1(C) has been reprinted with permission from Gerace et. al. [1] Copyright © 2017, Elsevier. Figure 1(D) has been reprinted with permission from Sjövall et. al. [2] Copyright © 2014, American Chemical Society. 2
1.3. Schematic representation of the composition of complex liquids and some of the important classes of dispersed ingredients 3
1.4. (A) and (B) : Schematic representation of methods for treatment of substrates with complex liquid formulations, (C) Cross-section of a textile sheet treated with fluorescent labelled cationic softener actives (Image copyright © Evonik Nutrition & Care GmbH), (D) Deposition of metallic nanoparticles on textile via treatment with metallic nanoparticle dispersion droplets (Image copyright © Marco Cirelli, University of Twente & Verosol) 4
1.5. (A) Sampling of patient's blood on a filter paper and (B) A typical dried blood spot with inhomogeneous deposition (Image reproduced from Lenk et. al. Bioanalysis (2015) 7(16), 1977-1985) with permission 5
1.6. Layout of the common areas of investigation in the application of complex liquid formulations on porous substrates 6

2.1. Schematic representation of the structures of lipid molecules, lipid bilayers, unilamellar and multilamellar vesicles. Typical structures of unilamellar and multilamellar vesicles as observed via cryo-TEM and light microscopy, respectively, are also shown. The Cryo-TEM image of unilamellar vesicles has been reprinted with permission from Battersby et. al. [11] Copyright © 2017, Elsevier. 9
2.2. Molecular structures of the esterquats used for preparing the vesicles used in the thesis [12, 13] 10
2.3. Size distributions of large (A) and small (B) DEEDMAC, WE18 and WE15 vesicle dispersions 12
2.4. Large and small DEEDMAC, WE18 and WE15 vesicles as observed via optical microscopy and cryo-electron microscopy, respectively. 12
2.5. Dynamic viscosity vs. shear rate profiles of the large (A) and small (B) vesicle dispersions at a lipid concentration of 8%.(Image reproduced with permission from Kumar et. al. [17]) 13
2.6. SEM images of viscose (A) and cotton (B) fibers, surface topography of viscose (C) and cotton fibers (D), and surface roughness profiles along the lines marked with arrow in (C) and (D) (Image reproduced with permission from Kumar et. al. [13]) 15

2.7. SEM images of the cotton yarns used in this thesis (Image reproduced with permission from Kumar et. al. [22]) 15
2.8. Top and cross-sectional views of the cellulose fiber filter papers, Whatman 903 and Sartorius 388 (Image reproduced with permission from Kumar et. al. [17]) . 16
2.9. Top views of the different grades of Sartorius filter papers. The substrates are arranged in the order of decreasing pore sizes from left to right. 17

3.1. (A) Experimental scheme used for streaming current/potential characterization of samples, and (B) Flow diagram of processes leading to streaming current/potential generation. The steps which could be affected by sample geometry are marked with red and labeled as 1-3. The existing theories/equations that can be used to describe these steps are also mentioned alongside. 19
3.2. (A) Velocity profile (shown in green) and electric charge density profile (shown in pink) inside EDLs near charged solid surfaces. (B) Schematic representation of an arbitrarily shaped porous sample. (C) Schematic representation of the force components acting on an infinitesimally thin liquid layer of thickness dz located at height z along the pressure gradient direction. (D) Schematic representation of the currents flowing in and out of the thin liquid layer due to streaming current and bulk conduction current flow. 24
3.3. (A)-(C) Geometry of non-uniform cross-sectional capillaries for which analytical solutions are obtained, (D) Variation of the generated streaming current along the length of the capillaries, and (E) Variation of U_{str} shape correction factor (U_{scf}) with the size ratio $\gamma_1 = R_i/R_o$ at a fixed size ratio $\gamma_2 = R_o/L = 0.1$ for the capillaries. For an ideal capillary with uniform cross-sectional area, U_{scf} is equal to 1. 29
3.4. A square array of cylindrical fibers with pressure difference applied parallel to the fiber axes. 32
3.5. (A) Square array of cylindrical fibers with pressure difference applied normal to the fiber axes, (B) Geometry of unit cells constituting the fiber array, and variation of the generated streaming current (C) and streaming potential (D) along the length of the unit cell. 33
3.6. Variation of the generated streaming current (maximum and average value) (A), and the generated streaming potential (B) with porosity in square fiber arrays for parallel and transverse flow directions. 38

4.1. (A) Experimental procedure for bulk esterquat concentration determination : (1) Formation of esterquat-Orange II complex, (2) extraction of the complex in chloroform, (3) measurement of chloroform phase UV-Vis absorbance, (B) Calibration curve for DEEDMAC and WE15 concentration determination 43
4.2. (A) Schematic representation of the streaming potential measurement setup, (B) Variation of streaming potential of viscose and cotton fiber plugs (1.5 g) with differences in pressure difference levels ($P_{vacuum2}$ was fixed at 100 mbar, and $P_{vacuum1}$ was varied from 180 to 350 mbar), and (C) Variation of ΔU_{str} with the number of runs during a typical measurement on fibers with deposited vesicles . . 45
4.3. Schematic representation of the experimental methodology for characterization of equilibrium vesicle deposition on single cellulose fibers 46

4.4. (A) Theoretical apparent zeta potential profile for SVL formation (solid line) and schematic profile for SLB formation (dotted line). Experimental variation of viscose fiber apparent zeta potential with adsorption densities (mg esterquat per gram fiber) and comparison with the theoretical solution for SVL formation of large vesicles (B) and small vesicles (C). Note: Experimental data points are represented as apparent zeta potential (mV) vs. adsorption density (mg/g), whereas the theoretical solution for SVL formation is represented as apparent zeta potential (mV) vs. vesicle surface coverage. Intact DEEDMAC (D) and WE15 (E) vesicles visualized via fluorescence microscopy after deposition on the external surface of a cellulose fiber membrane. 48

4.5. Adsorption densities obtained by deposition of large (A) and small (B) DEEDMAC and WE15 vesicles on viscose fibers. Effect of presence of additional small vesicles on adsorption densities of large DEEDMAC (C) and WE15 (D) vesicles. 51

4.6. Schematic representation of the deposition mechanisms of DEEDMAC and WE15 vesicles on viscose (smooth) and cotton (rough) fibers. DEEDMAC vesicles are shown as hexagons to illustrate their non-spherical angular shapes and presence of sharp edges, whereas WE15 vesicles are smoothly shaped and round, and are therefore represented as circles. 53

4.7. Adsorption densities obtained by deposition of large (A) and small (microfluidized) (B) DEEDMAC and WE15 vesicles on cotton fibers. Variation of apparent zeta potential of cotton fibers with deposition of large (C) and small (D) vesicles . 54

5.1. Fluorescence microscopy images showing the distribution of fabric softening vesicles deposited across cotton yarn cross-sections. As is evident, the deposition of large solid-gel vesicles is localized near the yarn periphery, whereas the deposition of small liquid-crystalline vesicles in homogeneously distributed across the yarn cross-section. This figure has been reprinted with permission from Venzmer et. al. [107]. 59

5.2. Schematic representation of the experimental methodology for (A) characterization of equilibrium vesicle deposition on single cotton fibers and cotton yarns, and (B) in-situ investigation of vesicle deposition kinetics on single cotton fibers. . . . 60

5.3. (A) Schematic representation of the colloidal permeation and deposition mechanism on a sequence of pores, (B) Schematic diagram depicting colloidal permeation and deposition on a single pore, (C) Flow diagram depicting the influence of the adsorbed layer on the deposition and permeation rates 62

5.4. Schematic representation of the plug configuration during streaming potential measurements on single fibers (A), model bi-porous substrate (B) and cotton yarns (C) 65

5.5. Comparison of the deposition kinetics of DEEDMAC and WE15 vesicles on single cotton fibers via in-situ streaming potential measurements 67

5.6. Adsorption densities obtained by deposition of DEEDMAC and WE15 vesicles on porous cotton yarns in the absence of salt (A) and with salt (C). Variation of the apparent zeta potentials of porous cotton yarns with adsorption density of DEEDMAC and WE15 vesicles in the absence of salt (B) and with salt (D). 69

6.1. Schematic representation of a typical surface modification treatment as carried out in industries 76
6.2. (A) Schematic representation of the simultaneous droplet spreading and imbibition process showing the spreading parameters, the base radius, $L(t)$, the dynamic contact angle of the liquid cap, $\theta_c(t)$, and radius of the wetted region, $l(t)$. (B) Sketch of the experimental setup used for the experiments 77
6.3. Schematic representation of the characteristic trends in variation of the spreading parameters, L (liquid cap base radius) and θ_c (contact angle) in the cases of partial and complete wetting 78
6.4. Evolution of the liquid cap and the wetted area with time for the spreading of a WE18 droplet on Sartorius 388 filter paper, as observed from the side and top cameras, respectively. The dimensions of the side view and the top view images are 7.4 mm × 5.6 mm and 18.3 mm × 13.8 mm, respectively. 79
6.5. Evolution of the liquid cap base radius, the wetted area radius, and the contact angle with time for the spreading of WE18 and WE15 droplets on Sartorius 388 (A,B and C) and Whatman 903 (D, E and F) 80
6.6. Evolution of the non-dimensionalized liquid cap base radius, the wetted area radius, and the contact angle with non-dimensionalized time for the spreading of WE18 and WE15 droplets on Sartorius 388 (A,B and C) and Whatman 903 (D, E and F) 81
6.7. (A) Schematic representation of secondary radial liquid penetration, (B) Wetted areas observed right after the disappearance of the liquid cap and after equilibrium has been reached for different liquid-substrate combinations 83

7.1. (A) Schematic representation of the experimental setup, (B) The Glovebox, Labmaster SP, which houses the experimental setup, (C) The arrangement showing the plexiglass table, the analytical balance, the UV light source, (D) Typical images of the top and botton views of the final stains 87
7.2. Schematic representation of the (A) original and (B) modified plexiglass tables, (C) Observed zero drifts with original and modified plexiglass tables 88
7.3. (A) Rectangular sections for the extraction of color intensity profiles along the horizontal and vertical center lines of images, (B) View of evaporation area in the red, green and blue color channels. 89
7.4. (A) Images captured by the top camera at different times during the test evaporation experiment with the blue channel normalized intensity profile overlapping with it. The dotted red line represents the lower normalized intensity threshold for the plateau region. (B) The raw blue color intensity profiles along the horizontal center line at different times during the evaporation process, (C) Normalized blue color intensity profiles along the horizontal center line at different times during the evaporation process, (D) Variation of the plateau diameter with time as obtained using different threshold values, (E) Final plateau diameter variation obtained by averaging the plateau diameter values obtained at the threshold values 0.25 and 0.30 90
7.5. Final stain images formed as observed from the top (A) and bottom (B). Blue color intensity profiles of the top and bottom view images along the center line of the images of the final stain. 92

7.6. (A) Liquid evaporation kinetics as obtained in the sample evaporation experiment (30 mg WE18 vesicle dispersion on Whatman 903), (B) Variation of the evaporation rate as estimated for the evaporation kinetics data 93
7.7. (A) Liquid evaporation from a thin liquid droplet, (B) Liquid evaporation from the wetted region formed on the porous substrate, (C) Variation of the evaporation mass flux along the radius of the wetted region as predicted by Eq.7.4 95
7.8. Mass variation during evaporation of different initial droplet masses of WE18 vesicle dispersion on Whatman 903 filter paper 95
7.9. Total initial wetted diameters obtained on Whatman 903 (A) and Sartorius 388 (B) with different masses of both the WE18 vesicle dispersion and water. Variation of the initial evaporation rates with the total wetted diameters on Whatman 903 (WE18 vesicle dispersion (C) and water (D)) and Sartorius 388 (WE18 vesicle dispersion (E) and water (F)) 96
7.10. Variation of the plateau diameter and evaporation rate with evaporation time for on Whatman 903 (WE18 vesicle dispersion (A) and Water (B)) and Sartorius 388 (WE18 vesicle dispersion (C) and Water (D)) 98
7.11. (A) Top and bottom view images of the final stains formed on Whatman 903 with droplets of different initial masses of the complex liquid (WE18 vesicle dispersion), (B) Diameters of the total wetted area, plateau diameter, diameter of the uniform deposition region (observed from top and bottom) obtained with different initial masses of the WE18 vesicle dispersion, (C) Widths of the coffee rings (top and bottom), and the unsaturated part of the wetted area 99
7.12. Schematic model describing how the wetted area and the stain deposit evolves during the evaporation process 101
7.13. Coffee ring stains formed on the Whatman 903 porous substrate with 30 μl droplets of WE18 vesicle dispersion at different concentration levels with respect to the original dispersion 102
7.14. Coffee ring stains formed on porous substrates with different pore sizes with 20 μl droplets of WE18 vesicle dispersion 103
7.15. Coffee ring stains formed on Whatman 903 with 30 μl droplets of WE18 vesicle dispersion at different temperatures 104

List of Tables

2.1. Measured instrinsic viscosities of the vesicle dispersions 14
2.2. Properties of the different grades of Sartorius filter papers as specified by the manufacturer 16

6.1. Secondary radial penetration of water, WE18 and WE15 vesicle dispersions on Sartorius 388 and Whatman 903 82

Resume

Abhijeet Kumar

Personal

Date of birth	25.10.1990
Place of birth	Dumka, India
Nationality	India

Academic

Since 2014	Ph.D. Student at Institute for Technical Thermodynamics, Mechanical Engineering, TU Darmstadt.
2012-2014	M.Tech. in Chemical Engineering, Indian Institute of Technology, Kanpur, India Thesis: *Formulation of poorly water soluble drugs as nanoparticles for biavailability enhancement*
2005-2009	B.Tech. in Chemical Engineering, Indian Institute of Technology, Kanpur, India

Professional

2015-2018	Researcher, Institute for Technical Thermodynamics, TU Darmstadt
2014-2015	Researcher, Research Interfacial Technology, Evonik Nutrition & Care GmbH, Essen, Germany
2013	R&D Internship, Formulation & Crystallization, Bayer AG, Leverkusen, Germany
2012	R&D Summer Internship, Nippon Paper Industries, Tokyo, Japan

Publications

Journal papers

A. Kumar, T. Gambaryan-Roisman, J. Venzmer, et. al. *Intact deposition of cationic vesicles on anionic cellulose fibers : Role of vesicle size, polydispersity, and substrate roughness studied via streaming potential measurements*, **J. Colloid Interface Sci. 473(2016), 152-161**

A. Kumar, T. Gambaryan-Roisman, J. Venzmer, et. al. *Influence of lipid bilayer phase behaviour and substrate roughness on the pathways on intact vesicle deposition : A streaming potential study*, **Colloids Surf., A , 521(2017), 302-311**

A. Kumar, T. Gambaryan-Roisman, J. Venzmer, et. al. *Effect of geometry on electrokinetic characterization of solid surfaces*, **Langmuir (2017), 33, 30, 7556-7568**

A. Kumar, T. Gambaryan-Roisman, J. Venzmer, et. al. *Electrokinetic investigation of fabric softener vesicle deposition on porous cotton fabrics*, **Journal of Colloid and Interface Science, 514(2018), 132-145**

A. Kumar, T. Gambaryan-Roisman, J. Venzmer, et. al. *Charge and Size Matters-How to Formulate Organomodified Siloxanes for Textile Applications*, **Colloids and Surfaces A 560 (2019) 180-188**

A. Kumar, J. Venzmer, T. Gambaryan-Roisman, et. al. *Spreading and imbibition of vesicle dispersion droplets on porous substrates*, **Colloids Interfaces 2019, 3(3), 53**

Conferences: oral presentation

International Association of Colloid and Interface Scientists (IACIS) Conference (2018), Rotterdam | *Coffee ring effect on porous substrates*

Bubble and Drop Conference (2017), Lyon |*Coffee ring effect on porous substrates*

European Colloid and Interface Society (ECIS) Conference (2016), Rome | *Cationic vesicle transport and deposition on anionic porous substrates*

Smart and Green Interfaces Conference (2016), Athens | *Using streaming potential measurements to probe cationic vesicle permeation and deposition on substrates*

Zsigmondy Kolloquium der Kolloid-Gesellschaft (2016), Regensburg | *Effect of lipid bilayer phase behaviour and substrate roughness on intact vesicle deposition*

Conferences: poster presentation

Complex Fluid Flow in Porous Media (2015), Bordeaux | *A streaming potential study of cationic vesicle deposition on anionic porous substrates*

Droplets (2015), Enschede | *Interaction of cationic complex liquids with anionic substrates*